Title
Design and Performance Evaluation of Building Integrated Solar Technology for Greywater Recycling and Thermal Gain

Author
Kagey, Henry

Publication Date
2019

Peer reviewed|Thesis/dissertation

Design and Performance Evaluation of Building Integrated Solar Technology for Greywater Recycling and Thermal Gain

By

Henry Kagey

A dissertation submitted in partial satisfaction of the

requirements for the degree of

Doctor of Philosophy

in

Engineering – Civil and Environmental Engineering

in the

Graduate Division

of the

University of California, Berkeley

Committee in charge:

Professor Slawomir Hermanowicz, Chair
Professor Steven Glaser
Professor Alexandre Bayen
Professor Maria-Paz Gutierrez

Summer 2019

ABSTRACT:

Developing sustainable building technologies to confront the growing pressure of essential resource scarcity is an important task for civil and environmental engineers in the 21st century. This dissertation describes the design, experimentation, and performance modeling of a multi-physics, building integrated, solar-powered panel system for on-site greywater recycling and thermal gain for interior climate conditioning. The hybrid CORE (Cylindrical Optical Reactive Cylinders) panel type is novel in itself, using wave-guides to support titania photocatalyst and distribute UV light for inactivation and mineralization of contaminants, which has not been studied to date, particularly in a multi-scale format.

Several research directions are detailed, from determining the potential for interception mechanics in the cylinder bank of waveguides, to the use of mathematical optimization for performance analysis. In chapter II, Finite Element Analysis on the micro-scale is used to develop a new correlation for particle capture of cylinder banks in non-creeping laminar flow. In chapter III laboratory experimentation on a CORE prototype is detailed in order to estimate reaction rates under solar conditions and determine the efficacy of the optical waveguides for stimulating mass transfer in a turbid medium. In chapter IV the NSGA-II algorithm for multi-objective optimization is employed to assess the influence of multiple parameters on the mass and heat transfer performance of the panel.

A novel correlation for particle interception in cylinder banks at moderate flow is given, as well as a simplifying rule of thumb for engineering design purposes. However, it is also shown that particle interception does not contribute meaningfully to disinfection in the CORE panel. The reaction rate for the CORE panel type is determined in the lab: the results show pseudo-zero order kinetics and an over all slow reaction proportional to the Reynolds number on the order of 1e-4. A correlation for reaction potential of individual cylinders developed via Chilton-Colburn analogy from Žukauskas' work on heat transfer in cylinder banks is shown to compare well with the experimental results, matching exactly at Re 350. It is also shown that the photocatalytic response is predominantly due to the effect of waveguide UV transmission.

The performance evaluation of the CORE panel in the pilot scale simulation in Berkeley, CA. using the NSGA-II genetic algorithm for the multi-objective studies on efficiency and output showed tendency for maximizing cylinder diameter and thus solid fraction, tilt generally pushed towards a 45 tilt from the vertical, and that CORE could function with a relatively thin over all profile of about 5cm. The maximum daily output of recycled greywater for a $1m^2$ panel over a year was 87L, a relevant contribution to reuse of an individual's daily grey water production. The panel system functions best as building added system on the roof, but could function as building integrated with specific modifications to the catalyst to increase photosensitization. Further research is required in the direction of multi-parameter

optimization both to incorporate more parameters and design constraints (such as the effect of flow rate and solid fraction on energy return) and as a design tool to estimate context dependent design requirements.

TABLE OF CONTENTS

CHAPTER

LIST OF FIGURES

I.

II.

III.

IV.

Acknowledgements

Throughout the research for and writing of this dissertation I have received a great deal of support and assistance. I would like to first thank my advisor Dr. Slav Hermanowicz, whose guidance and expertise was invaluable in formulating my research plan and developing accurate methodology, as well as sharing interesting and meaningful conversation far outside of his field of study. Second, I would like to thank Professor Maria Paz-Gutierrez for proposing this project as well as for her insight and collaboration along the way. Third, I would like to thank my group mate Dr. Vivek Rao for his camaraderie and partnership in multiple projects and help in the laboratory. Fourth, I need to thank Dr. Allen Hunter for always making himself available to talk about solving problems across a number of dimensions and platforms. Finally I would like to thank my committee for their time and encouragement in this process.

I also need to thank the National Science Foundation Emerging Frontiers in Research Innovation (EFRI) Grant # 1038279 for years of support. Additional financial support from the TBSI (Tsinghua Berkeley Shenzhen Institute) program at UC Berkeley is also acknowledged.

Finally I would like to thank my parents, Dr. H. Price Kagey and Lyn Kagey, Esq. for being there to stop gaps whenever necessary, and of course for inspiring me to intellectual work through example. I also want to thank my son Elliot Kagey-Satinover for putting up with me as his sole parent, for being forgiving when I wasn't always available due to work obligations, and for helping me to stay focused when I didn't want to. I love you all very much.

Chapter I:
Literature Review

I. Motivation:

Developing sustainable technologies to meet current and projected essential resource demands will one of the most significant challenges of the 21st century. It is widely acknowledged that climate change is occurring in our time; the problems this presents for civilization will be first felt through world's water supply. [1] Already water scarcity and stress affect a significant percentage of the global population, in both developed and undeveloped countries, and it is expected that demand will be exacerbated in even the near future, particularly with current usage trends.

The World Health Organization [2], [3] lists several key facts regarding water scarcity and stress:

- 844 million people lack even a basic drinking-water service, including 159 million people who are dependent on surface water.
- Globally, at least 2 billion people use a drinking water source contaminated with feces.
- Contaminated water can transmit diseases such diarrhea, cholera, dysentery, typhoid, and polio. Contaminated drinking water is estimated to cause over 500,000 diarrheal deaths each year.
- In low- and middle-income countries, 38% of health care facilities lack an improved water source, 19% do not have improved sanitation, and 35% lack water and soap for hand washing.
- By 2025, half of the world's population will be living in water-stressed areas.

Though water demand projections tend to be more dire than predicted in developed areas [4], the threat to the world's available water supply current usage poses is real and present.

Water, food, and energy production and use are deeply interconnected; the security of one of these sectors is tied directly to that of the others. For example, 30% of the world's energy is used in the food production and supply chain, while 70% of the world's freshwater use is for agriculture. [5] In California moving water from the Bay Area to Southern California represents the single largest electricity load in the state. [6] The relationship of these human needs is close enough to merit a special moniker, the Water-Food-Energy Nexus, due to the fact that demands on each are increasing, and the demands on one become demands on the others. As one of these sectors is diminished in capacity, so will the others be affected in their ability to meet increased demand.

The interconnections between these sectors are not solely a matter of direct management and use. Green house gas production related to fossil fuel based energy production and consumption are expected to have dramatic effects on the world's climate, and the resulting effects on the world's useable water stores is similarly expected to be severe, as drought, flood, and other extreme weather events are expected to increase in frequency and in occur regions where they currently do not. [7], [8] Though it may seem counter intuitive, extreme weather events such as flooding damage drinking water supplies, thus causing significant water stress in areas affected. [9] We will not only feel climate change through its effect on water supplies: as more water needs to be produced to match diminishing reserves, more green house gases will be produced in a runaway process. [10]

Beyond the stress currently experienced through out the world and the dire prophecies of what is to come based on current use, rapid population growth continues in much of the world. The world is undergoing the largest wave of urban growth in history. More than half of the world's population now lives in cities, and by 2030 this number will swell to about 5 billion, 60% of the projected whole. [11] As urban centers grow and our numbers concentrate, the regional demands they create become increasingly acute. Local fresh water supplies will need to be supplemented with imported water. The water demand imposed by urban centers is expected to exceed the volume available by 40% by 2030. [12]

Rapid urbanization requires concomitant built development to match its pace. This also implies increased energy use both directly and embodied in the instruments of growth. Urban areas account for as much as 76% of energy use, and are responsible for about three quarters of global carbon emissions. [13] Buildings generate a significant amount of the energetic cost and demand in the urban environment, amounting to 20% of the world's energy consumption. [14] Space conditioning alone demands up to 50% of this use in the US. [15] Population growth and its localization in urban centers will have an accelerating and amplifying effect on the rapine of essential resources owing to the involved nature of the WFE nexus.

Existing infrastructure to deal with increasing demand is outdated in many ways. As cities grow in relation to national populations, the infrastructural requirements will be hard pressed to extend into outlying developments while providing sufficient services. [16] The energetic cost of pumping water to and from centralized treatment plants accounts for a notable percentage of most states' energy usage in the US, and the energetic cost of this is expected to grow along side the scale of cities. [17] The range of challenges that energy and water producers and distributors face is mounting in the face of growth, climate change, and scarcity. Fortunately, the centering of these problems on the burgeoning cityscape provides the possibility for these challenges to transform into opportunities by focusing on strategies for developing the built environment that diverge from existing infrastructure approaches to servicing society's needs, focusing on sustainable, low impact technologies and methods for essential resource management and delivery. [11], [18]

This literature review will provide a brief overview of the resource problems and the technologies arising to alleviate them. The goal of this chapter is to present the space wherein the CORE technology has been developed, as well as to identify gaps in the existing research that CORE fills.

II. Towards Net Zero: Intention

2.1 Towards Net-Zero – Energy

Despite countless warnings of climate change towards global warming from environmental scientists and its associated mechanism of green house gas production, there are still those who dispute it as a present danger. [19] This research will do nothing to either support or deny those claims. However, the sheer numbers of those in agreement around the possibility of climate change forces action on the part of engineers and policy makers as a means of risk mitigation. Recent sweeping proposals on the federal level may be unrealistic, but policy changes are needed if we are to take the threat seriously. [20]

Sustainable, non-carbon based, energy generation has been a topic of great interest for some time now. The reasons are manifold beyond decreasing green house gas production, energy independence and diversifying essential resources among them. In considering new technologies for a sustainable energy economy, the existing infrastructure designed for centralized production and distribution is problematic due to transmission and capacity constraints. [21] These issues are exacerbated when considering water resources, as it's delivery has an enormous additional embodied energy cost which is rapidly growing with urban density. [22] Bringing energy production and water reuse to the local scale of the built environment is a strategy that transforms these challenges into opportunities for development to integrate with and alleviate stress on existing infrastructure rather than to further burden it. [23]

The concept of Zero Energy Building (ZEB) and Net-Zero Energy Building (NZEB) has gained attention since the turn of the millennium as a target for sustainable design. The primary thrust of the movement towards Net-Zero is that residential and commercial buildings supply all energy for their functioning. The details of what is included in ZEBs are still under consideration, but four main issues embedded in the concept of Zero Energy Buildings are 1) what the metrics of the balance of energy are, 2) the types of resources included in the balancing, and 3) connections to infrastructure, and 4) the period over which energy balance is measured. [24] These issues received significant discussion following the turn of the century, but the principle behind the N/ZEB remains the same, "the idea that buildings can meet all their energy requirements from low-cost, locally available, nonpolluting, renewable sources." [25]

Of the issues listed above, several are points of contention when it comes to assessing how to implement policy. First, the metrics of Energy are not

standardized for the ZEB, whether to use kgs of CO_2 (which varies based on supply), Joules (which doesn't account for the green house gas produced), 'overall carbon footprint', or some other measureable unit. [26] Beyond this, implicit in the definition of ZEBs and Net ZEBs is an annual accounting, that is, the life cycle of buildings is not consistently considered part of the embodied energy cost of materials and construction. Finally, and important to this discussion, the energy cost of all resources, e.g. water, are not included in the accounting of cost. [27]

The issue of grid/infrastructure connectivity is what is embedded in the difference between the terms Zero Energy and Net-Zero Energy, Net Zero indicating that the over all annual energy balance of a building is supplemented at times with energy supplied by the grid, as opposed to the energy independent Zero Energy Building. [28] The Zero Energy Building as a free-standing event isolated from its urban environment has been criticized as a needless waste of resources (existing infrastructure), as these instruments are not a burden to be abandoned, but a resource that could be used in concert with emerging technologies; their existence should guide design decisions for the transition into a truly sustainable energy future. [29] Despite the clear need for infrastructure integration for urban centers to embrace the possibility of NZEBs, Torcellini still notes that there is a pressing need for supply side technologies if Net Zero is to become a reality and not simply a shell game of selling back energy to utilities off of peak consumption hours. [26]

The hierarchy of Net Zero design strategies begins with passive options: site orientation for taking advantage of insolation, insulation, passive cooling, and installing LED bulbs, for example. Second order choices are related to renewable energy or reusable water sources available on site, including technologies such as photo-voltaic (PV), solar thermal heating, and on site hydro- and wind generators. The third order of options relates to renewable energy resource trading off site. [30] There are opportunities for technologies to supply this hierarchy at every level, however the first and second levels of the hierarchy are those most apt for moving forward into energy independence in the future. It is here then that this research will focus, on passive, solar, building integrated systems, in terms of seeking solutions to the intersecting problems of responsible urban development and renewable energy supplies.

2.2 Towards Net-Zero – Water

The low hanging fruit for building integrated water conservation are flow controls such as low volume flush toilets and low flow faucets. Beyond this, the single greatest opportunity for reducing water demand in the built environment is in the reuse of greywater generated on site. Greywater is the wastewater outfall from sinks, showers, and laundry, differentiated from black water outfall from the toilet. Of the greywater water released from households (see figure 1.1), up to 60% is reclaimable for reuse after light treatment. [31] Some distinguish further between types of from these sources as 'light greywater' from showers and hand wash basins, and heavy greywater from kitchen sinks and clothes/dish washers in terms of their

pollutant load. [32] Opportunities for reuse of greywater are typically confined to toilet flushing, clothes washing, and irrigation and these represent up to 30-40% of urban domestic water use of 90-120 Liters/day per person. [33]

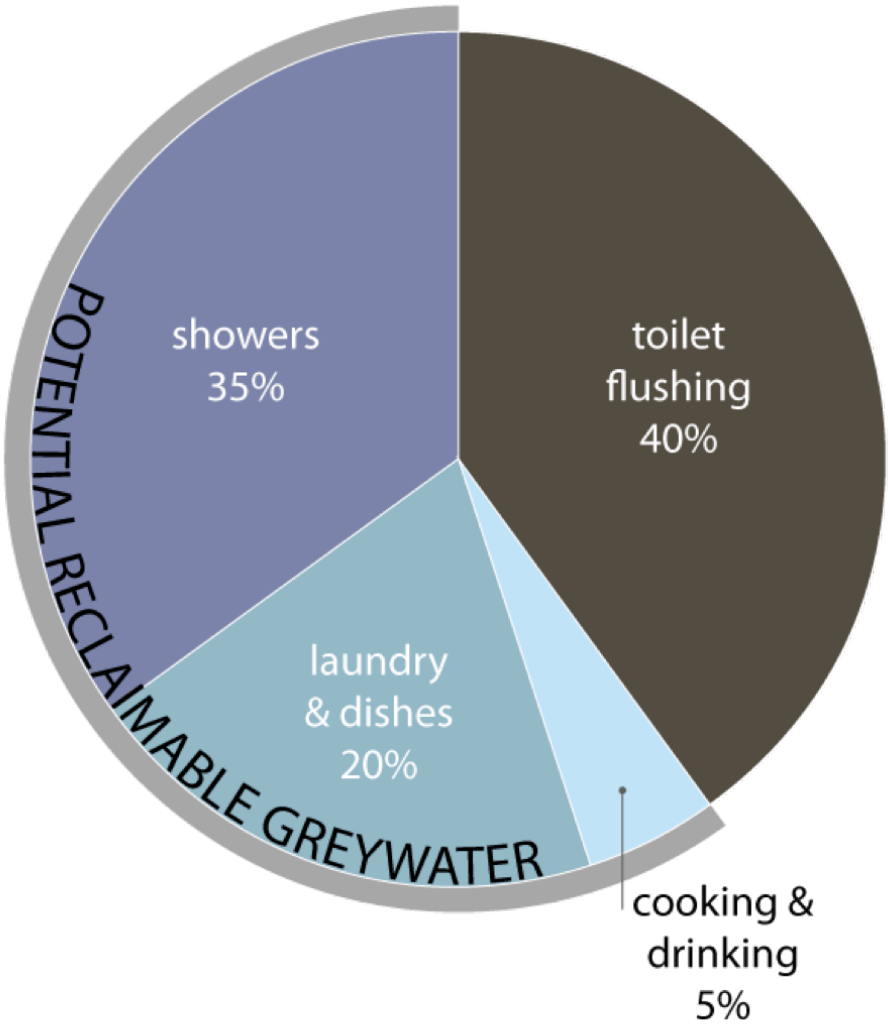

Figure 1.1: Potential reclaimable greywater outfall from residential sources

Studies on the implementation of greywater reuse have shown up to 25-40% reduction in import demand in urban centers. [34] Reuse has been shown not only to have significant effects on water conservation, but also on infrastructure requirements, easing the load on systems in the present and projected maintenance in the future. [35] Due to urban reuse opportunities being limited, more sophisticated greywater reclamation strategies have been proposed wherein optimal pollutant loads are 'designed' by mixing certain outfall sources to meet specific decontamination and recycling needs. [36] Greywater separation and reuse is a critical step in moving towards water security in water stressed regions and Net Zero strategies in sustainable building. This is another area where this research will focus on providing solutions to the problems of resource conservation in the built environment.

In the beginning of the 21st century there were proposals both in Europe and the US to achieve Net Zero by 2020, 2025, 2030, and as time moved on, 'nearly Net Zero' by those targets. [37], [38] Since the scholarly exploration of the NZEB definition described in the preceding paragraphs, the US Department of Energy has included Net Zero Water as a concurrent definition of sustainability targets. [39] The city of San Francisco is an example in this regard, and now requires that new buildings built in the downtown area have some method for on site water recycling and non-potable reuse and that the entirety of reclaimed greywater be reused in the building that generated it, up to the buildings non-potable demands. [40]

While policy is pushing urban areas to move towards Net Zero Energy and Water, the technologies that feed the supply side without taxing the existing infrastructure are not as available as they need to be for these policy side targets to become a reality. The intersection of need for both energy generation/conservation and water reuse/conservation, along with the localization of systems to on-site or the community level of implementation is a little explored niche in the green tech sector. In this research I will describe the design and characterization of a solar active building integrated technology for the gathering of thermal energy and greywater reuse. The system is a hybrid technology that aims to achieve both energy and water conservation at the same time, to 'heat and treat' water as both a energy bearing medium for climate conditioning in buildings, as well as for reuse once the useful heat has been recovered.

III. Net Zero Technologies:

3.1 Net Zero Technologies – Solar Thermal

Solar technology is driven by the fact that the sun produces massive amounts of energy that reaches the earth in direct and indirect forms such as radiation and wind. Solar thermal collectors are used in domestic, agricultural, and industrial processes for a variety of purposes. Energy recovery from solar thermal energy takes the forms of electricity and heat and installations for doing so range in scale from multistory machines to residential panels. [41], [42] This research will focus on solar thermal technologies for water heating at the building scale as this is a promising technology for approaching Net Zero Buildings. For example, it has been estimated that in the residential sector smaller scale passive models for solar thermal of 100L capacity can save 1500KWh of electricity annually. [43] These technologies are found in both the developed and developing world due to simple, low cost design and ease in application. [44]

Thermal collectors typically heat a fluid transport medium (air, water, or oil, the "working fluid") and are distinguished by 1) passive or active collection (stationary or pump-driven/tracking collectors) and 2) their operating temperatures. [45] Stationary models, the lower operating temperature technologies, are further divided into Flat Plate collectors (FPCs), and tubular absorbers (Evacuated Tube

Collectors (EVCs) and Compound Parabolic Collectors (CPCs)). Of the tubular collectors, EVCs use vacuum insulation as a means to avoid losses, whereas CPCs use optical surfaces to concentrate incident radiation (and also sometimes employ solar tracking) on an evacuated tube. FPCs, EVCs, and CPCs use black absorber plates to capture and transform solar radiation into heat transferred to the working fluid. [46] Most types also have a radiation transparent glazed aperture to contain gathered heat and prevent convective losses from the absorber plate.

FPCs are the simplest model of solar thermal collector, and are preferred for small-scale implementation due to the lack of active controls. These are typically of two types, flow through and batch. The flow-through models, where water is heated by being passed over the absorber plate in a copper or aluminum pipe, are the most common and have an operating temperature between 30-80C. Batch thermal collectors have similar working temperatures, but differ in that the fluid medium rests next to the absorber plate and heats over a period of hours. [47] There are many models of both types, as well as considerable research devoted to their individual parts, such as the best material for absorber plates. [48], [49] Nano-fluids, fluids with suspended metallic nanoparticles, have been researched as well, as means to accelerate working fluid heat absorption. [50]

The simplest of the solar water heating technologies is the batch water heater. Efficiencies for heat conversion range up to 60% for free standing models, but can be higher for systems that have only one convective surface, such as building integrated models. There is significant interest in building integrated solar thermal (BIST) technologies that will be discussed later. [51], [52] The general thermal efficiency for SWH models is given by the equation:

$$\eta_t = \frac{(m_{tot} c_{p,tot})\Delta T}{IA\Delta t} \quad (1)$$

where m_{tot} (kg) is the total mass, $c_{p,tot}$ (J/kg°C) is the lumped heat capacity of the system, ΔT (°C) is the overall change in temperature, I (W/m^2) is the total irradiance, A is the aperture area, and Δt is the time of collection. Annual efficiencies are lower due to seasonal variation and intermittence, but still are expected to be between 30-40%. [53] Solar thermal water heating is considered a necessary technology for achieving Net Zero Energy before 2050. [54]

3.2 Net Zero Technologies - Solar Water Disinfection

The use of solar water disinfection (SODIS) for drinking water has been recorded for millennia. SODIS is currently used as a low cost, effective surface water (as well as greywater) treatment, especially in undeveloped communities, where diarrhea is prevalent and responsible for the deaths of 1.8 million annually. [55] SODIS requires nothing more than sunlight, clear PET bottles, and a suitable frame to hold them. Though pre-treatment such as settling is recommended, it is not necessary for disinfection. [56]

SODIS functions through two recognized, synergistic mechanisms: photolysis and pasteurization. [57] Photolysis operates on microbial contaminants through the mechanism of high energy UV light damaging the DNA of bacteria, rendering them incapable of reproduction. Inactivation of cell reproduction is wavelength dependent: UVC at wavelength 254 nm is an order of magnitude more effective that of UVB light at 300 nm. [58] Disinfection through SODIS then is not the direct process of killing bacterium, but the indirect process of removal by rendering bacteria sterile. For this reason, inactivation plots show a 'shouldered curve' (see figure 1.2 below), that is, no reduction of bacteria until the critical time at which their diminished reproduction rate is seen in the population. [59] The dose transmitted to organisms is called 'fluence' (irradiance*time: kJ/m^2), and its effect is measured indirectly by observation of bacterial populations. [60] Studies on the inactivation of biological contaminants focus on *E. coli* as the target bacteria for the reason that *E. coli* shows the most resistance to fluence, and is thus an indicator of the presence of other microorganisms as well. [61] The consequence of high frequency light inactivation is that SODIS technologies must have high transmission for UV light in order to be maximally effective.

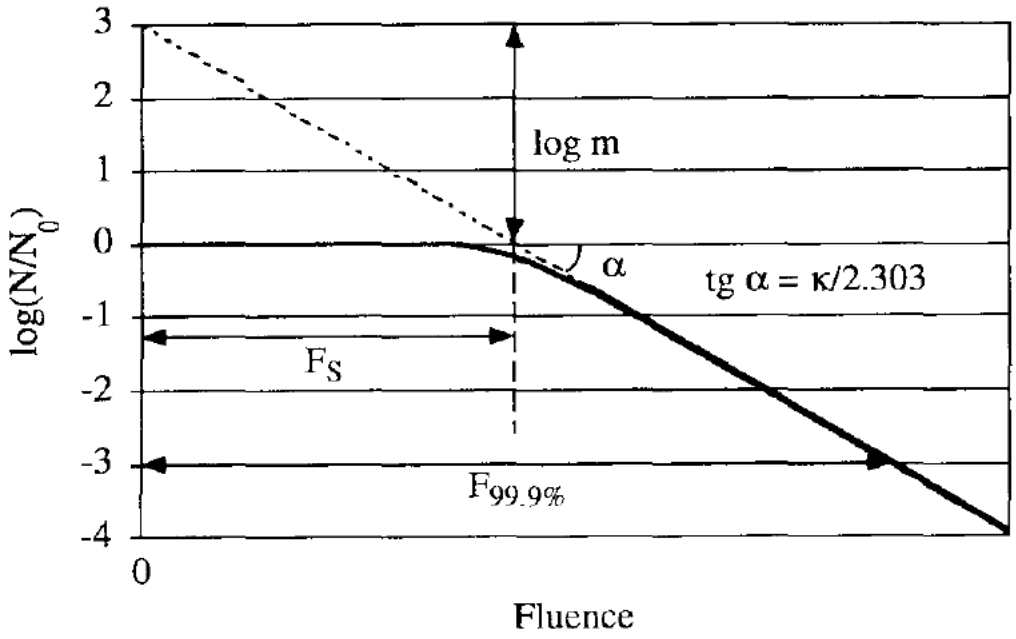

Figure 1.2: Shouldered curve for inactivation based on fluence

The second mechanism that SODIS is presumed to employ in bactericide is pasteurization. As discovered in the 19th century, bacteria in water that reaches temperatures greater than 60C for 5-30 minutes are largely destroyed. Though it is not common for low tech SODIS technologies to achieve temperatures such as these [62], as PET bottles are essentially batch solar water heaters without black body absorbers or insulation, several technologies for SODIS have been developed and tested that employ specific adaptations to increase heat gain, such as reflectors and absorbers. [63], [64] Studies show that with adaptions for heat gain, SODIS

installations are capable of reaching 75C and producing disinfected water at the cost of 0.008USD/L (in 1998). [65]

The synergistic effects of heat gain and photolysis are also reported on in the literature. [66] Batches with rising temperatures between 30-50C show increased inactivation of pathogens, up to three times the rate at 25C when at 50C. [61] While there is potential for disruption of *E. coli* with rising temperature, some research reports that *E. coli* increase reproduction rates at pre-pasteurization temperatures, peaking at 37C. [67] Other work has shown the sensitivity of various biological contaminants to the dual effect of UV and mild heat between 40 and 52C varies by pathogen, yet reduces fluence to 3log inactivation (i.e., heat and photolysis are synergistic) if above 45C for multiple strains. [68] Models for the synergistic effects of inactivation through photolysis and pasteurization have been formulated analytically and compared favorably to measured results of in field tests. [69] Though there is not full understanding of the mechanisms at play in the solar disinfection of water, SODIS has been adopted in a number of rural communities for its effectiveness in relieving disease from water borne pathogens as well as its low cost implementation at treating surface water for potability. [70], [71]

Unfortunately, with regard to greywater SODIS is not as effective due to turbidity; there is significant UV shielding and light scattering above 40 NTU. [72] Greywater water is difficult to characterize as it varies by source in the domestic environment, as well as by culture. However it has been seen that greywater throughout the world regularly has a high TSS count, and a concomitant high NTU. [73] Fenner characterizes the optical effects of UV blocking in grey water for UV fluence curves, but does not directly relate this to the TSS of grey water samples. [74] Measured values for greywater in Greece linearly correlate 70mg/L TSS with an NTU of 80. [75] For reference, at an NTU of 5 water is visibly cloudy, and at 25 it is murky. Bacteria are not the only pollutant in greywater, and the cloudiness of grey water is not due to microorganisms alone, but also the high degree of minerals present. Though some technologies are in development to super heat greywater using optical concentrators (micro-lenses), these still do not remove organic compounds found in greywater. [76] For this reason the mechanisms of pasteurization and photolysis assumed for SODIS will not be as effective for treating greywater as it is for clarified surface waters.

3.3 Net Zero Technologies – Photocataylsis

Strategies for the remediation and reuse of residential grey water employ a number of technologies, from MBRs to biological contactors. [77], [78] To achieve Net Zero however, it is important to look for lower energy cost solutions to on site greywater remediation. SODIS is promising for surface water treatment in areas where low-tech/cost solutions to water borne pathogens are necessary, however in the residential sector of developed countries greywater remediation targets include minerals that SODIS cannot effectively deal with. For this reason we must

investigate further possibilities for solar powered greywater remediation and reuse solutions.

Heterogeneous semi-conductor photocatalysis is a low energy cost technology that has been studied in connection with its ability to disinfect fluids and surfaces for over 40 years. [79], [80] Semiconductor photocatalysis operates by the absorption of high energy light in the atomic structure of photocatlysts, where the energy in the photons is converted into chemical energy. It is an Advanced Oxidation Process (AOP) whereby highly reactive hydroxyl radicals are formed in an aqueous environment. [81] These reactive hydroxyls oxidize kill bacteria by both disrupting cell membranes and damaging DNA in their nuclei, and mineralize almost any organic compound they come in contact with, yielding CO_2 and inorganic ions, particularly important for surfactant rich grey water remediation. [82] Applications of photocatalysis range from hospitals to agriculture as a lower risk means to water disinfection and bactericide than chlorination. [83] As a solar powered source of disinfection, photocatalysis used as a cleansing chemical action is promising as a means for water reuse in the built environment. [84]

Semi conductor catalysts include Fe_2O_3, CdS, ZnO, and the most widely known and used, TiO_2, though titanium dioxide is the most widely used of the catalysts. [85] Degussa P-25, a 70/30 anatase/rutile mixed phase TiO_2, is the most common commercial semiconductor photocatalyst due to its high photoactivity, low cost, availability, and that it has "band energies that are well matched to the redox properties of water." [86] Titania catalyst has a band gap of 3.2 eV, corresponding to the UV wavelengths up to 385nm; it is thus well suited for solar applications. While there have been many studies performed on mercury and (more recently) LED bulb photocatalysis [87]–[90], solar applications are preferred for Net Zero applications due to the passive, low cost energy source.

Semiconductors are activated by the absorption of a photon into their atomic structure, which is characterized by a filled valence band and an empty conduction band. The absorption of a photon with sufficient energy to promote an electron past the band gap leaves a valence band hole behind (h^+), leading to the formation of an electron/hole pair in the molecular structure. Most charge pairs will immediately recombine, however when electron scavengers are present, such as in oxygenated water, redox reactions occur and a hydroxyl radical (OH•) is formed. The photon is thus a reactant, TiO_2 technically the "photosensitizer", and it is the water and also oxygen therein that is photochemically altered by this interaction. [91] A description of the generation of reactive oxygen species in equation form and diagram is shown below:

$$TiO_2 + hv \rightarrow h^+ + e^- \quad (2)$$

$$h^+ + (H_20 \leftrightarrow H^- + OH^-) \rightarrow H^+ + OH\bullet \quad (e\ donor) \quad (3)$$

$$e^- + {O_2}^- \rightarrow (O_2H\bullet, H_2O_2, OH\bullet) \quad (e\ acceptor) \quad (4)$$

$$h^+ + e^- \rightarrow heat, light \qquad (recombination) \qquad (5)$$

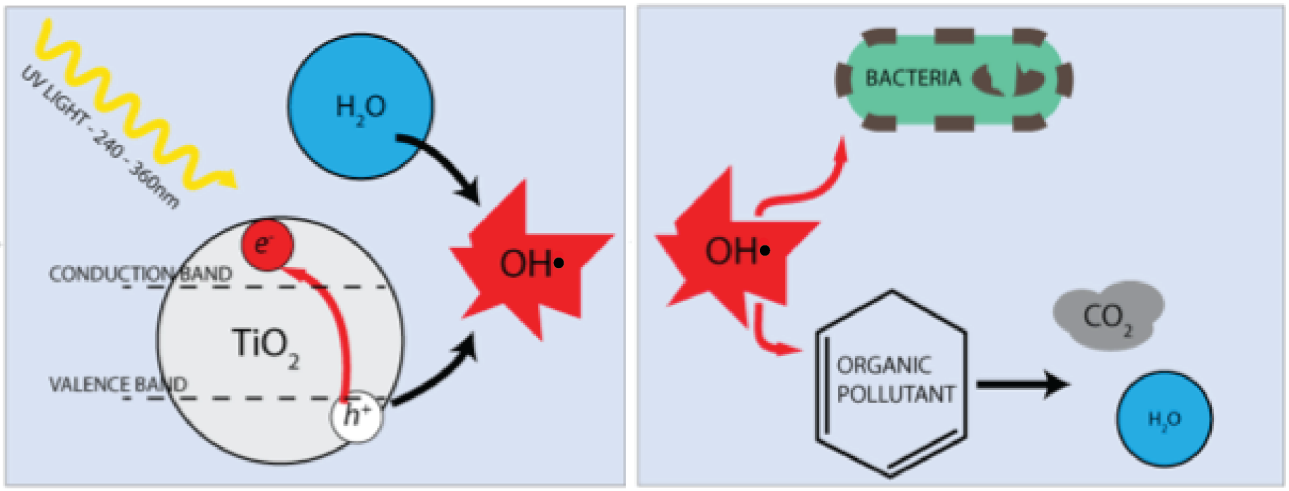

Figure 1.3: Schematic of titanium dioxide photocatalysis in water a) energy absorption and radical formation, and b) ensuing attack on biological pathogens and mineralization of organic pollutants

Titanium dioxide is popular due to its high quantum yield. The radicals produced are very short lived, and for this reason the interaction of pollutants with them are modeled as surface reactions on the catalyst surface. Due to the intermediary mechanism of removal reactions, the kinetics of those reactions has been the subject of much research. [92], [93] In general, the reaction rate is assumed to follow Langmuir-Hinshelwood kinetics, owing to the need for adsorption and desorption of pollutants for inactivation and mineralization on the surface of the catalyst. [94] The transport constant K in the reaction rate equation below demonstrates its influence:

$$R = k\theta = k\left(\frac{KC}{1+KC}\right) \qquad (6)$$

where θ represents the 'coverage' of the catalyst surface and C the instantaneous concentration of the contaminant. Note that as C becomes small, θ becomes KC, as is the case for systems where there is infrequent contact of the pollutant with the catalyst surface. The reaction is called 'pseudo-first order' for low concentration reactions, and is written:

$$k'C = kKC \qquad (7)$$

where k' is the pseudo-first order reaction rate constant. Pseudo-first order reactions are limited by the availability of surface sites and contact available for reaction.

If the concentration of the contaminant is high, the surface becomes saturated and the rate limiting step is depends on the reactivity of the radicals and the contaminant, as it is assumed there is full coverage at all times. In this case:

$$\left(\frac{KC}{1+KC}\right) \approx 1 \Rightarrow k\theta = k \tag{8}$$

This is referred to as a pseudo-zero order reaction owing to its non-log linearity. [95] Pseudo-order reactions are considered slow reactions due to the limitation of the availability of radicals, due either to low oxygen content or low photoactivity of the catalyst. [96]

The efficiency of photocatalytic reactions is defined by the quantum yield, the ratio of how many photons are converted into charge/hole pairs that generate radicals to the number of photons incident on the catalyst, determined by a reaction rate over the rate of absorption of radiation. [97]

$$\Phi_{overall} = \frac{rate\ of\ reaction}{rate\ of\ photon\ absoprtion} \tag{9}$$

This is of course hard to measure, as photon absorption as a quantity is not clear when photons are transmitted, scattered, absorbed by a photocatalyst. [91] Others have proposed the term "photonic efficiency" to describe the conversion rate of an activated photocatalyst. [98] The photonic efficiency describes the molecular conversion of a compound over the number of photons incident on a plane and contacting the catalyst surface.

$$\xi_{h\nu} = \frac{reaction\ rate}{Incident\ light\ intensity\ on\ reactor\ aperture} \tag{10}$$

Serpone proposed to correlate all photonic efficiencies to phenol removal, while that has not become common practice, photonic efficiency as a measure of reactant disappearance is.

As described above, the initial concentration of the reactant has a significant affect on reaction kinetics. Other factors that influence the activity of the photocatalytic reactions include radiation flux, temperature, pH and catalyst type. The activity of TiO_2 catalyst is linearly dependent on UV light intensity, up to an intensity of $25mW/cm^2$ ($250W/m^2$) of the relevant wavelengths, where upon increase in radiation flux amplifies the reactivity proportional to an exponential factor of ½. [99] Temperature also affects the reaction rate, decreasing it above 80C and below 0C, with increase between these ranges with increase in temperature, thus the optimum temperature range for photocatalytic activity is in the normal environmental range. [100] Other factors affecting solar photocatalytic kinetics and efficiency are explored in Chapter 3 of this document.

Photocatalytic reactors can be slurry systems, but this is generally eschewed for water treatment when reuse is the goal due to the difficulty in separating the catalyst at the end step of the process. [101] More commonly in fluid remediation, whether gas or liquid phase, the catalyst is immobilized by sintering on a surface where the fluid is allowed to pass over. The light sensitivity of photocatalytic reactions and their subsequent interaction with contaminants has fueled significant research into process intensification for applications in water remediation. [102] The amount of UV light present in the solar spectrum is only ~3-5% of the total incident energy at the earth's surface (see figure 1.4 below). For this reason research in photocatalytic reactors focuses on maximizing light transport to high surface area reactors to increase quantum yield. [103]

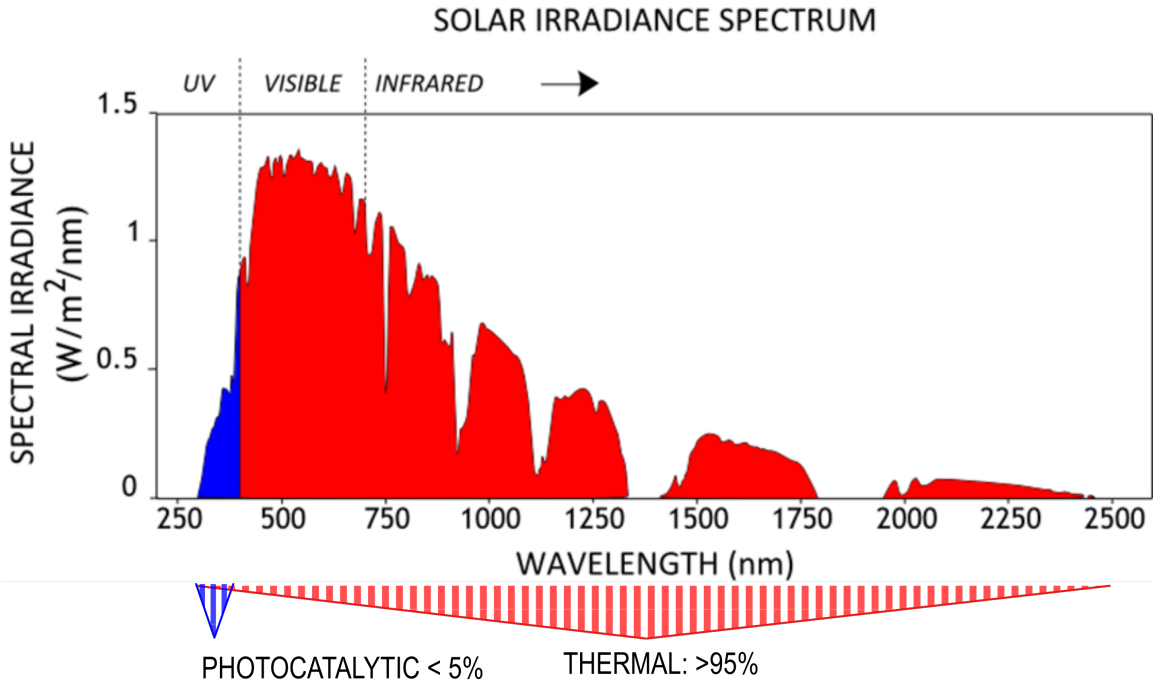

Figure 1.4: Solar spectrum distribution at the earth's surface

3.4 Net Zero Technologies - Photocatalytic reactors

Solar photocatalysis for water reclamation is perceived as a secondary or tertiary treatment for the removal of bacteria and mineral waste, after sedimentation/ filtration and/or activated sludge. [104], [105] There are a number of technologies that have been designed for this purpose. In order for these reactors to be effective, they require immobilized TiO_2, and thus also require more complicated arrangement of supports and light intensification strategies. Common in the literature is the use of CPCs for light intensification. [106] Other common studies involve tubular reactors, thin film fixed bed (TFFBRs), and double skin sheet reactors (DSSRs) (to increase irradiated surface area to volume ratios). [107]–[111] Also common is the comparison or combination of SODIS and SPC for microbial

contaminant removal. [112], [113] Interestingly, these studies frequently show that there is little difference in removal of pathogens such as *E. coli*, though SODIS has little to no efficacy in mineralizing surfactants. [114] Research on scaled up treatment plants have shown that there is little degradation in TiO_2 coating after numerous trials, suggesting that this technology is competitive for repeated, daily greywater recycling at the residential level. [115]

SODIS and Solar PC have been studied together owing to that their mechanisms are different, but both frequently are operating concurrently in solar photocatalytic reactors. However, the turbidity of grey water (as with slurry TiO_2) creates significant shading and thus decreased efficiency for both photocatalytic reactions and photolytic removal. A reactor type that has been developed for remote light transmission from a gathering lens or surface to the interior of a medium is the Photocatalytic Optical Fiber Reactor (OFR). This reactor type was first studied in the late 70s/early 80s, with seminal work done by Marinangeli and Ollis. [116]–[118] OFRs have since been studied for use remediation of liquids [119] and gases [120].

The typical OFR employs immersed fiber-optic tubes coated with photocatalyst. UV light enters from the end of the tube and reflects down the length of the fiber, refracting into the coating and scattering through it to generate radicals at the surface in contact with the medium. The goal is to maximize light transmission to the immobilized catalyst, bringing the light directly into the medium rather than having to penetrate though its surface, in order to enhance UV distribution and uniformity. OFRs typically have bundles of fibers thin fibers activated by a concentrated light source, whether bulb or solar. [121], [122] Recent studies have investigated the efficacy of compact, low-energy LED sources as well. [123] OFRs have been shown to be effective at the removal of organic contaminants such as 4-chlorophenol, benzene, acetone, malic acid, and methylene blue among others. [120], [124]–[126]

What is unique among these reactor types is that the photons enter the catalyst from within the optical waveguide, and pass through the catalyst layer to generate radicals in a contaminated medium. For this reason the optical properties of both the waveguide and the catalyst are important. Snell's Law determines the orientation of beam radiation inside the waveguide via material properties:

$$n_1 sin\theta_1 = n_2 sin\theta_2 \tag{11}$$

where *n* is the index of refraction and the subscripts 1 and 2 refer to incident and transmitted beams respectively. Once inside the waveguide, the energy of reflection (R) and transmission (T) of unpolarized light in a non-magnetic material is determined by the Fresnel equations:

$$R = \left|\frac{n_1 cos\theta_1 - n_2 cos\theta_2}{n_1 cos\theta_1 + n_2 cos\theta_2}\right|^2 \quad (12)$$

and

$$T = 1 - R \quad (13)$$

The upshot of these equations for titania coatings is that the light energy transmitted to the photocatalyst is completely internally reflected (CIR), that is it will not scatter out of the coating either back into the waveguide or out into the medium if the index of refraction of the bulk is sufficiently low, as is the case in gas and aqueous media. [127] Scattering in TiO_2 films greater than 1.5μm is essentially random owing to the multiple scattering that takes place in the nanostructure of the sintered catalyst. [128] The index of refraction for TiO_2 is estimated at 2.5 to 2.8, while those of borosilicate glass, water and air are 1.5, 1.33, and 1.0 respectively. [129], [130] In Figure 1.5, the subscripts on I (intensity) are I for incident, t for transmitted, and r for refracted.

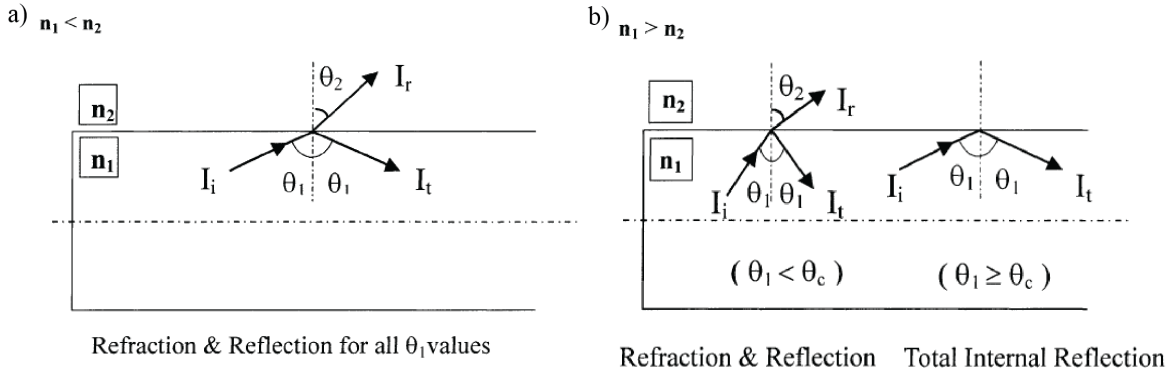

Figure 1.5: Reflection and transmission in optical waveguide for a) low to high index of refraction, and b) high to low, with CIR beyond the critical angle (θ_c) (from Choi, 2001)

The attenuation of light in a waveguide depends on the number of reflections (length and incident angle of incoming beam) and attenuation coefficient of the medium of propagation. Beer-Lambert Law gives the spatial calculation for attenuation:

$$I(z) = I_o e^{-\alpha z} \quad (14)$$

where α is the attenuation coefficient and z is the path length. Attenuation has important implications for the catalyst coating thickness: coatings too thick will extinguish UV energy within the catalyst coating and coatings too thin will have insufficient photoactivity. Several studies have been performed on optimal coating thickness for transmission to waveguide surface in OFRs. Choi found the optimal

catalyst depth to be 1.5μm, while Lin suggested that the thickness of the coating lost reactivity both above and below 0.4μm, and more generally that the thickness of the coating needed to match the wavelength of the light, that is if it were thinner than 400nm, the catalyst would not be sufficiently activated for the generation of hydroxyl radicals. [121], [131] OFR fibers have been shown to ineffective when the waveguides are over 15cm long due to the attenuation in the fiber as well as for the number of reflections in fibers longer than this. [132] More generally, the number of reflections that still contain energy for catalyst activation are fewer than 4 or 5. For bulb activated OFRs, the incident UV light beam angle is typically between 70 and 80 degrees. [127], [132] Solar powered OFRs have used concentrators to generate incident angles of light along these parameters, but are large compared to the volume of media they are capable of remediating. [129]

OFRs present an attractive option for greywater remediation due to their ability to transmit UV into turbid media, specifically grey water. [133] Unfortunately studies for OFRs and greywater do not yet exist. The development of a reactor incorporating waveguides remains a fruitful direction for greywater remediation research.

3.5 Net Zero Technologies - Building integrated and Hybrid technologies

The building sector has significant opportunities for mitigating climate change via the adoption of sustainable technology and strategies. It is estimated that buildings directly consume 40% of the world's energy and 15% of the world's water resources. [18] Direct use water urban sources (drinking water, water heating, wastewater treatment, and steam services) have been estimated to account for 12% of the USA's primary energy consumption. [134] The trend of increasing urbanization portends that resource stress will focus on the landscape of the city, even though the services that manage these resources are also located there.

The built environment itself provides the site and the scaffolding for decentralized, infrastructure-light resource management, that is, the building presents an opportunity for containing energy infrastructure. [135] Building Integrated technologies have been studied as feasible sustainable, energy efficient technologies for decades, in particular solar technologies for the obvious reason that the sun irradiates the outer surface of buildings. It is important to note that researchers distinguish between Building Integrated technologies (BI, façade integral) and Building Added (BA, rooftop mounted) systems. [136] The most well known of these systems are photo-voltaic (PV) panels, but there are many types of sustainable energy BI technologies available, such as solar thermal systems, ventilated envelope, and 'smart' light tracking louvers to moderate insolation based on interior climate needs. [137] BI technologies have been compared favorably to BA technologies due to architectural advantages, and studies have shown that the relative insolation penalty they face for not having rooftop tilt-axis optimality is offset by increasing the area of the panels, because the area available for envelope integration is much

greater over all for many buildings, in particular those with more than 2 levels. [138]

Building Integrated Solar Thermal systems have seen a dramatic rise in interest for the past 20 years. [139] The systems generally have a working fluid (water, air, or refrigerant) that is the heat transport medium for multiple functions inside the building. Passive solar heating combined with energy efficient building construction technologies can reduce the space heating demand up to 30%. On the other hand, active solar systems can decrease the fuel demand for hot water and space heating from 50% to 70% for hot water and 40% to 60% for space heating. [140]

Building integrated systems are seen as synergistic with the building climate control demands because the façade integrated system acts as insulation for the building envelope itself, while at the same time air gaps between the panels and interior act as significant insulation for the working fluid. [141]

One of key possibilities and opportunities of BI systems is their potential for exploiting synergies both architecturally as well as the physics of their processes. A primary example of this is the photovoltaic-thermal (PV-T) panel, a hybrid solar technology for electrical and thermal gain. The PV-T panel has been developed since the 70s, with many configurations using gaseous and liquid working fluids studied for optimality since then. [142] The thermal gain in the working fluid functions as a cooling mechanism for the PV aspect of the panels, increasing the electrical efficiency up to 10%, and can then be channeled into the building for low and medium heat quality climate interventions on site. [143] BIPV-T systems have been analyzed for performance in a variety of environments and site specific accommodations have been suggested for improved function and architectural appeal/compatibility. [144], [145] More details on the development and performance of PV-T collectors can be found in Chapter 4 of this work.

Other hybrid building integrated solar technologies are photovoltaic–algal systems that act as bio-fuel producers on site. [146] These systems are largely conceptual at this point, but provide insight to potential future directions. There are next to no building integrated hybrid systems at this point that focus on water reclamation. Indeed, literature on water focused sustainable building integrated technologies is relatively sparse. While some active water reuse technologies such as MBRs have been suggested for building integrated grey water recycling, they are energy intensive and require a considerable amount square footage. [147] A passive building integrated water reclamation technology is the “green roof”, where runoff is collected and potentially remediated through filtration and chemically altered through absorption by plant biomass. [148] In general, however, building integrated solar water resource technologies are in short supply, and the field requires the proposal of feasible prototypes and studies on performance.

Considering that building integrated solar technology is the most promising avenue towards achieving NZEBs, challenges for adoption and implementation of BI

technology have also received attention. Most frequently citied is the lack of knowledge on the part of architects about the possibilities of sustainable BI technology, both in education and in budget management. [149] Many architects are simply unaware of the possibilities of building integrated systems, which is generally the purview of engineers. Additionally, the upfront cost is higher than for a simple building skin alone, but the over all profitability of BI systems has been proven despite relatively short time for analysis of the most recent case studies. [141], [150] Finally, the implementation of BI systems requires specific knowledge of façade design that not all architects have training for. The majority of these challenges are addressed by expanding the range of education both academically and professionally. Despite these challenges, the prospect for the future of solar BI systems is bright. [151]

IV. Objectives of this research:

The research formulated in this document has several objectives: 1) the proposal of a sustainable on-site hybrid solar technology for energy gain and grey water reclamation, 2) the identification of mechanisms and synergies such a technology might present, and 3) the characterization and performance analysis of the proposed technology.

Several strategies were conceived, considered, and tested. Initial studies focused on a passive Fixed Bed Batch Reactor that sought to use natural convection due to thermal gain to enhance mass transfer over catalyst-coated pellets. After fluid dynamic analysis of flow resistance this idea was discarded as not feasible, and active strategies were investigated. The most promising of these is the CORE (Cylindrical Optical Reactive Elements) reactor.

The CORE panel design employs TiO_2 coated high transmission glass cylindrical waveguides that allow UV light deep into the otherwise low UV transmitting grey water for photo-catalytic disinfection. This design uses the high surface area to volume of the cylinder surfaces for greater photocatalytic disinfection potential, and is tunable for disinfection and heat gain potential by altering the geometric configuration and flow rate.

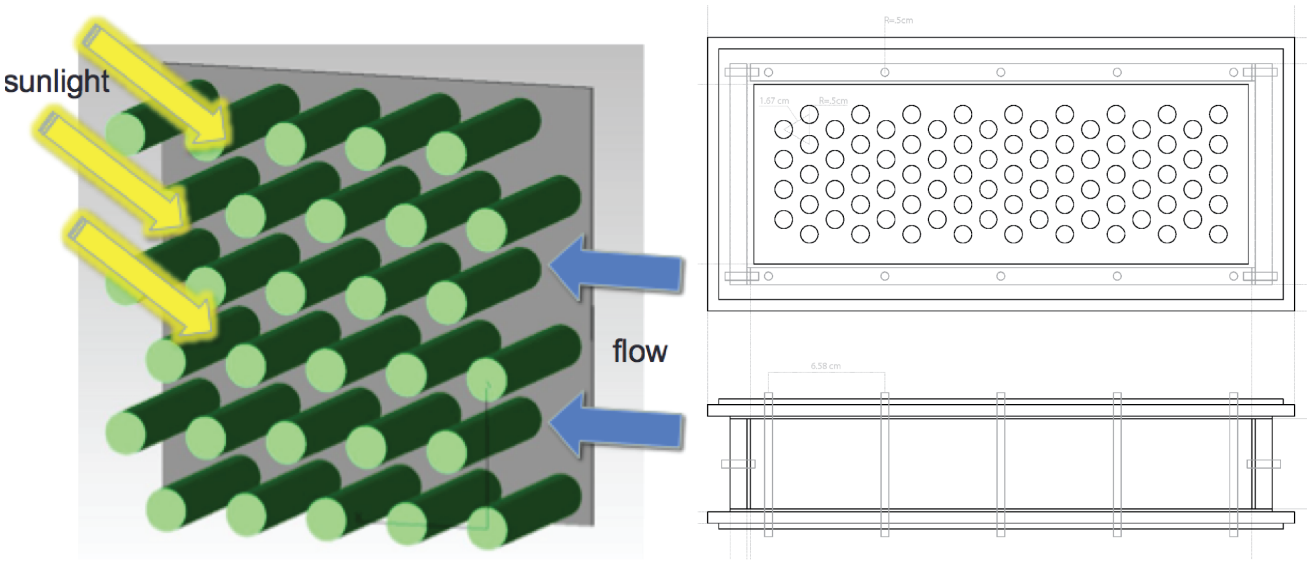

Figure 1.6: CORE panel concept and prototype

Forced flow moves fluid over the waveguides in a recirculating batch. The back of the fluid filled panel is a heat absorber. Details of the configurations are seen in chapters 3 and 4.

The optical elements required investigation both for light transmission and flow characteristics. Studies on tube and shell heat exchangers provided the most relevant source material for flow considerations, while the optical analyses were formulated as ray trace studies in Matlab and . Initial benchmark studies for the viability of modeling and simulations were undertaken in Matlab and COMSOL and compared to previous work (see figure 1.7 below for comparison of pressure drop in cylinder banks from heat exchanger studies). The ray tracing and pressure drop studies are not included in detail in this document, as they were considered preliminary.

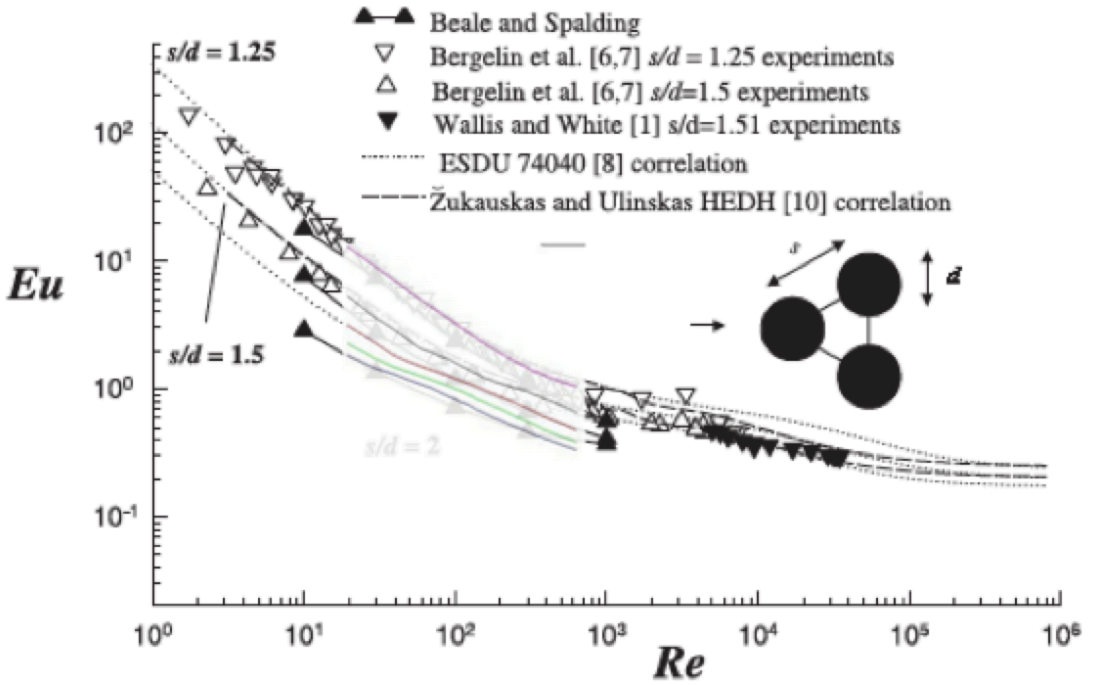

Figure 1.7: Benchmark studies on pressure drop in color, comparison to Beale [152]

V. <u>Structure of this document:</u>

In the following chapters, key concepts regarding the mechanisms and characterization of the proposed panel system will be addressed. This dissertation is presented as four chapters demonstrating several directions research on the CORE panel prototype took. Each chapter contains a relevant and more concise literature review on the topic of its focus. While each chapter draws on different research methodologies, they are interdependent: each chapter informs the work and direction of the others. Thus, while each chapter is presented as a distinct and independent contribution with its own reference section, it is necessary to view them as a whole when considering the objectives of the thesis. Figure 1.8 describes the topics that are investigated in each of the main chapters in terms of physics, technology and scale. It can be seen in this figure that the primary topic of the dissertation is greywater recycling.

Chapter 1 (this one) is a literature review to identify areas where novel contributions might be made to the field of building integrated solar technologies.

Chapter 2 is a study on particle interception for cylinders in cross flow. In the early stages of research on CORE particle interception was investigated as a possible mechanism for pathogen removal. After a preliminary review of the literature, a gap for particle interception in the moderate laminar flow ranges was discovered, and thus a simulation study developed to identify and characterize particle interception for bacteria on cylinders in the moderate laminar flow range.

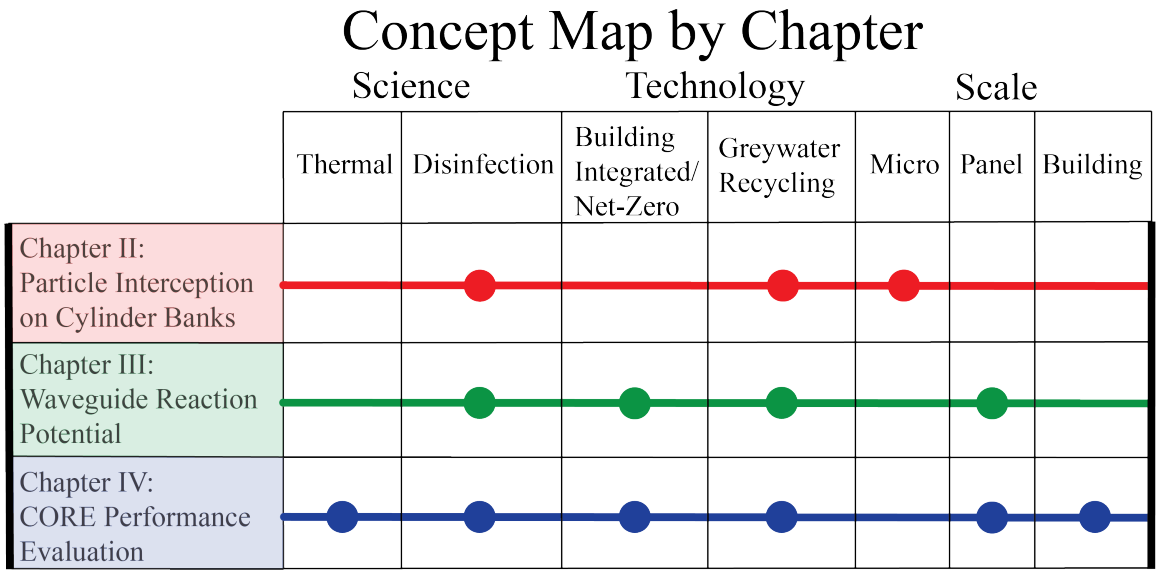

Figure 1.8: Concept Map of Topics by Chapter

In Chapter 3 the kinetics of the CORE reactor are investigated experimentally. A solar simulator in the lab is used to characterize the removal in a laboratory setting for use in modeling studies. The study focuses on the function of the waveguides in turbid media using a grate, simulating full particle shielding in the bulk of the panel prototype. No other study on greywater shielding in waveguide photocatalysis currently exists. The effect of waveguides is characterized in a turbid media, and reaction rates are found and reported.

In Chapter 4 the performance CORE panel is investigated with the use of the NSGA-II genetic algorithm. The algorithm is used not only as an optimization tool, but also as a means for determining where implementation of the panel system might be most advantageous. Important parameters are identified and suggestions for actual implementation are made.

In chapter 5 the thesis concludes with a summary and directions for future research.

References:

[1] J. Bruce, I. Burton, and B. Mills, "Water Sector : Vulnerability and Adaptation to Climate Change Water Sector : Vulnerability and Adaptation to Climate Change," 2000.

[2] WHO, "Guidelines for Drinking-water Quality, Fourth Edition Incorporating the First Addendum," 2017.

[3] R. Brite and A. McKelvey-Clayson, "Water in a Changing World: Chapter 2, The United Nations World Water Development Report," 2009.

[4] M. Heberger, K. Donnelly, and H. Cooley, *A Community Guide for Evaluating Future Urban Water Demand*, no. August. 2016.

[5] A. Flammini, M. Puri, L. Pluschke, and O. Dubois, "Walking the Nexus Talk: Assessing the Water-Energy-Food Nexus in the Context of the Sustainable Energy for All Initiative," UN FAO, 2014.

[6] C. Copeland and N. T. Carter, "Energy - Water Nexus: The Water Sector's Energy Use," 2017.

[7] OECD, *Water and Climate Change Adaptation: Policies to Navigate unchared Waters*. 2013.

[8] J. Morrison, M. Morikawa, M. Murphy, and P. Schulte, "Water Scarcity & Climate Change: Growing Risks for Businesses and Investors," 2009.

[9] A. Chanda Shimi, G. Ara Parvin, C. Biswas, and R. Shaw, "Impact and adaptation to flood," *Disaster Prev. Manag. An Int. J.*, vol. 19, no. 3, pp. 298–313, Jun. 2010.

[10] IPCC, *Climate Change 2014: Synthesis Report*. 2014.

[11] UNFPA, "State of World Population 2007: Unleashing the Potential of Urban Growth," 2007.

[12] Water Resources Group, "Charting Our Water Future," 2009.

[13] K. C. Seto, "Human Settlements, Infrastructure and Spatial Planning," in *Climate Change 2014: Mitigation of Climate Change. Contribution of Working Group III to the Fifth Assessment Report of the Intergovernmental Panel on Climate Change*, O. R. Edenhofer, Y. Pichs-Madruga, E. Sokona, S. Farahani, K. Kadner, A. Seyboth, I. Adler, B. S., P. Brunner, B. Eickemeier, J. Kriemann, S. Savolainen, C. Schlömer, T. von Stechow, T. Zwickel, and J. C. Minx, Eds. Cambridge University Press, Cambridge, United Kingdom and New York, NY, USA, 2014, pp. 993–1000.

[14] Energy Information Administration, *International Energy Outlook 2016-World energy demand and economc outlook*, vol. 0484, no. May. 2016.

[15] J. Kelso, "Delivered Energy End-Uses for an Average Household by Region (Million Btu per Household)," 2008.

[16] D. L. Boucher, "Keep Up: Infrastructure Failing to Keep Pace with Demand for Housing," *The Urban Developer*, pp. 9–14, 2018.

[17] K. Hussey and J. Pittock, "The Energy – Water Nexus : Managing the Links between Energy and Water for a Sustainable Future," *Ecol. Soc.*, vol. 17, no. 1, 2012.

[18] K. Vairavamoorthy *et al.*, "Options for Decoupling Economic Growth from Water use and Water Pollution," 2017.

[19] K. E. Björnberg, M. Karlsson, M. Gilek, and S. O. Hansson, "Climate and environmental science denial: A review of the scientific literature published in 1990–2015," *J. Clean. Prod.*, vol. 167, pp. 229–241, 2018.
[20] A. Ocasio-Cortez, *HR. Res. Con. 763*, vol. 000000. 2019, pp. 1–8.
[21] G. Crabtree *et al.*, "Integrating Renewable Electricity on the Grid," 2011.
[22] C. W. King, A. Hardberger, M. Webber, A. S. Stillwell, and I. J. Duncan, "Energy-Water Nexus in Texas," *Ecol. Soc.*, vol. 16, no. 1, 2012.
[23] P. Gleick and G. Wolff, "Global Freshwater Resources: Soft-path solutions for the 21st Century," *Science (80-.).*, vol. 302, no. November, p. pp.1524-1528, 2002.
[24] A. J. Marszal *et al.*, "Zero Energy Building – A review of definitions and calculation methodologies," *Energy Build.*, vol. 43, no. 4, pp. 971–979, 2010.
[25] D. Crawley, S. Pless, and S. Torcellini, "Getting to Net Zero Energy Buildings," *AHSRAE J.*, no. September, 2009.
[26] P. Torcellini, S. Pless, and M. Deru, "Zero energy buildings: A critical look at the definition.," in *Preprint, ACEEE Summer Study*, 2006, vol. 2, p. 15.
[27] DOE, "US Department of Energy: A Common Definition for Zero Energy Buildings," no. September, p. 22, 2015.
[28] I. Sartori, A. Napolitano, and K. Voss, "Net zero energy buildings: A consistent definition framework," *Energy Build.*, vol. 48, pp. 220–232, 2012.
[29] B. Vale and R. Vale, *The New Autonomous House: Design and Planning for Sustainability.* Thames & Hudson Ltd., 2002.
[30] S. Pless and P. Torcellini, "Net-Zero Energy Buildings : A Classification System Based on Renewable Energy Supply Options," *Tech. Rep. NREL/TP-550-44586*, no. June, pp. 1–14, 2010.
[31] C. Gerba, T. Straub, J. Rose, M. Karpiscak, K. Foster, and R. Brittain, "Water quality study of graywater treatment systems," *Water Resour. Bull.*, vol. 31, no. 1, pp. 109–116, 1995.
[32] E. Friedler, "Quality of individual domestic greywater streams and its implication for on-site treatment and reuse possibilities," *Environ. Technol.*, vol. 25, no. 9, pp. 997–1008, 2004.
[33] S. De Gisi, P. Casella, and M. Notarnicola, *Grey Water*, vol. 4. Elsevier, 2017.
[34] R. Penn, M. Hadari, and E. Friedler, "Evaluation of the effects of greywater reuse on domestic wastewater quality and quantity," *Urban Water J.*, vol. 9, no. 3, pp. 137–148, 2012.
[35] E. Friedler and M. Hadari, "Economic feasibility of on-site greywater reuse in multi-storey buildings," *Desalination*, vol. 190, no. 1–3, pp. 221–234, 2006.
[36] F. Li, K. Wichmann, and R. Otterpohl, "Review of the technological approaches for grey water treatment and reuses," *Sci. Total Environ.*, vol. 407, no. 11, pp. 3439–3449, 2009.
[37] A. ASHRAE, Engineers, "ASHRAE Strategic Plan," 2010.
[38] C. Hachem-Vermette, F. Guarino, V. La Rocca, and M. Cellura, "Towards achieving net-zero energy communities: Investigation of design strategies and seasonal solar collection and storage net-zero," *Sol. Energy*, no. July, pp. 0–1, 2018.
[39] DOE, "Handbook for Net Zero Energy, Water, and Waste: Exisiting Buildings,"

2017.
[40] San Francisco Health Code, *ARTICLE 12C: ALTERNATE WATER SOURCES FOR NON-POTABLE APPLICATIONS*. 2016.
[41] L. L. Winter, C.J., Sizmann, R. L. Vant-Hull, *Solar Power Plants: Fundamentals, Technology, Systems, Economics*. New York: Springer, 2012.
[42] D. Mills, "Advances in solar thermal electricity technology," *Sol. Energy*, vol. 76, no. 1–3, pp. 19–31, 2004.
[43] S. C. Kaushik and K. R. Ranjan, "Energetic and Exergetic Performance Evaluation of Natural Circulation Solar Water Heating System," *Appl. Sol. Energy*, no. 52, pp. 16–26, 2016.
[44] F. Spate, B. Hafner, and K. Schwarzer, "A system for solar process heat for decentralised applications in developing countries.," 1999.
[45] S. A. Kalogirou, *Solar thermal collectors and applications*, vol. 30, no. 3. 2004.
[46] S. Kalogirou, "The potential of solar industrial process heat applications," *Appl. Energy*, vol. 76, no. 4, pp. 337–361, 2003.
[47] B. Norton, "Industrial and agricultural applications of solar heat," *Compr. Renew. Energy*, vol. 3, pp. 567–594, 2012.
[48] M. G. Hutchins, P. J. Wright, and P. D. Grebenik, "Comparison of Different Forms of Black Cobalt," *Sol. energy Mater.*, vol. 16, pp. 113–131, 1987.
[49] M. L. T. Moncada, B. C. Muñoz, M. M. Yoshida, and R. D. Rodríguez, "Comparative experimental study of new absorbent surface coatings for flat plate solar collectors," *Energy Procedia*, vol. 57, pp. 2131–2138, 2014.
[50] H. Tyagi, P. Phelan, and R. Prasher, "Predicted Efficiency of a Low-Temperature Nanofluid-Based Direct Absorption Solar Collector," *J. Sol. Energy Eng.*, vol. 131, no. 4, p. 041004, 2009.
[51] ISO/FDIS, "INTERNATIONAL STANDARD ISO / FDIS Solar energy — Solar thermal collectors — Test methods," 2013.
[52] C. Maurer, C. Cappel, and T. E. Kuhn, "Simple models for building-integrated solar thermal systems," *Energy Build.*, vol. 103, pp. 118–123, 2015.
[53] D. A. Hagos, A. Gebremedhin, and B. Zethraeus, "Solar Water Heating as a Potential Source for Inland Norway Energy Mix," *J. Renew. Energy*, vol. 2014, pp. 1–11, 2014.
[54] H. M. Henning and A. Palzer, "A comprehensive model for the German electricity and heat sector in a future energy system with a dominant contribution from renewable energy technologies - Part I: Methodology," *Renew. Sustain. Energy Rev.*, vol. 30, pp. 1003–1018, 2014.
[55] T. F. Clasen, H. T. Do, S. Boisson, and O. Shipin, "Microbiological effectiveness and cost of boiling to disinfect drinking water in rural Vietnam," *Environ. Sci. Technol.*, vol. 42, no. 12, pp. 4255–4260, 2008.
[56] K. G. McGuigan, M. du Preez, R. M. Conroy, H.-J. Mosler, P. Fernandez-Ibañez, and E. Ubomba-Jaswa, "Solar water disinfection (SODIS): A review from bench-top to roof-top," *J. Hazard. Mater.*, vol. 235–236, pp. 29–46, 2012.
[57] M. B. Fisher, "The effects of wavelength, metals, and reactive oxygen species on the sunlight inactivation of microorganisms: observations and applications to the solar disinfection of drinking water," UC Berkeley, 2011.
[58] J. R. Bolton, "Terms and Definitions in Ultraviolet Disinfection," *Proc. Water*

Environ. Fed., vol. 2000, no. 2, pp. 25–40, 2011.
[59] O. K. Scheible, "Development of a rationally based design protocol for the ultraviolet disinfection process.," *J. Water Pollut. Control Fed.*, vol. 59, no. 1, pp. 25–31, 1987.
[60] W. A. M. Hijnen, E. F. Beerendonk, and G. J. Medema, "Inactivation credit of UV radiation for viruses, bacteria and protozoan (oo)cysts in water: A review," *Water Res.*, vol. 40, no. 1, pp. 3–22, 2006.
[61] Wegelin *et al.*, "Solar water disinfection : scope of the process and analysis of radiation experiments," *Aqua J. Water Supply Res. Technol.*, vol. 43, no. vol. 43, 3, pp. 154–169, 1994.
[62] C. Navntoft, E. Ubomba-Jaswa, K. G. McGuigan, and P. Fernández-Ibáñez, "Effectiveness of solar disinfection using batch reactors with non-imaging aluminium reflectors under real conditions: Natural well-water and solar light," *J. Photochem. Photobiol. B Biol.*, vol. 93, no. 3, pp. 155–161, 2008.
[63] D. A. Ciochetti and R. H. Metcalf, "Pasteurization of naturally contaminated water with solar energy," *Appl. Environ. Microbiol.*, vol. 47, no. 2, pp. 223–228, 1984.
[64] N. Safapour and R. H. Metcalf, "Enhancement of solar water pasteurization with reflectors," *Appl. Environ. Microbiol.*, vol. 65, no. 2, pp. 859–861, 1999.
[65] A. J. Fjendbo Jørgensen, K. Nøhr, H. Sørensen, and F. Boisen, "Decontamination of drinking water by direct heating in solar panels," *J. Appl. Microbiol.*, vol. 85, no. 3, pp. 441–447, 1998.
[66] G. K. Rijal and R. S. Fujioka, "Synergistic effect of solar radiation and solar heating to disinfect drinking water sources," *Water Sci. Technol.*, vol. 43, no. 12, pp. 155–162, 2001.
[67] M. AHMAD, B. S. SRIVASTAVA, and S. C. AGARWALA, "Effect of Incubation Media on the Recovery of Escherichia coli K12 Heated at 52 0C," *J. Gen. Microbiol.*, vol. 107, no. 1, pp. 37–44, 1978.
[68] M. Berney, H. U. Weilenmann, A. Simonetti, and T. Egli, "Efficacy of solar disinfection of Escherichia coli, Shigella flexneri, Salmonella Typhimurium and Vibrio cholerae," *J. Appl. Microbiol.*, vol. 101, no. 4, pp. 828–836, 2006.
[69] M. Castro-Alférez, M. I. Polo-López, J. Marugán, and P. Fernández-Ibáñez, "Mechanistic modeling of UV and mild-heat synergistic effect on solar water disinfection," *Chem. Eng. J.*, vol. 316, pp. 111–120, 2017.
[70] R. M. Conroy, M. Elmore-Meegan, T. Joyce, K. G. McGuigan, and J. Barnes, "Solar disinfection of drinking water and diarrhoea in Maasai children: A controlled field trial," *Lancet*, vol. 348, no. 9043, pp. 1695–1697, 1996.
[71] P. Kalt, C. Birzer, H. Evans, A. Liew, M. Padovan, and M. Watchman, "A solar disinfection water treatment system for remote communities," *Procedia Eng.*, vol. 78, pp. 250–258, 2014.
[72] Swiss Federal Institute of Environmental Science and Technology (EAWAG), "Water Quality: Turbidity and water depth," 1998.
[73] M. Tamanna, M. Jalil, S. Islam, and S. Anam, "Grey water generation and quality measurement at a specific site in Dhaka city," *IEB Conf.*, pp. 978–984, 2011.
[74] R. A. Fenner and K. Komvuschara, "A New Kinetic Model for Ultraviolet Disinfection of Greywater," *J. Environ. Eng.*, vol. 131, no. 6, pp. 850–864, 2005.

[75] G. Antonopoulou, A. Kirkou, and A. S. Stasinakis, “Quantitative and qualitative greywater characterization in Greek households and investigation of their treatment using physicochemical methods,” *Sci. Total Environ.*, vol. 454–455, pp. 426–432, 2013.
[76] W. Lee *et al.*, “Solar optics-based active panel for solar energy storage and disinfection of greywater,” *Biomicrofluidics*, vol. 10, no. 5, pp. 1–8, 2016.
[77] M. S. Fountoulakis, N. Markakis, I. Petousi, and T. Manios, “Single house on-site grey water treatment using a submerged membrane bioreactor for toilet flushing,” *Sci. Total Environ.*, vol. 551–552, pp. 706–711, 2016.
[78] A. M. Abdel-Kader, “Studying the efficiency of grey water treatment by using rotating biological contactors system,” *J. King Saud Univ. - Eng. Sci.*, vol. 25, no. 2, pp. 89–95, 2013.
[79] M. Tadashi, T. Ryozo, N. Toshiaki, and W. Hitoshi, “Photoelectrochemical sterilization of microbial cells by semiconductor powders,” *FEMS Microbiol. Lett.*, vol. 29, no. 1–2, pp. 211–214, 1985.
[80] K. Hashimoto, H. Irie, and A. Fujishima, “TiO 2 Photocatalysis : A Historical Overview and Future Prospects,” vol. 44, no. 12, pp. 8269–8285, 2005.
[81] M. Pera-Titus, V. García-Molina, M. A. Baños, J. Giménez, and S. Esplugas, “Degradation of chlorophenols by means of advanced oxidation processes: A general review,” *Appl. Catal. B Environ.*, vol. 47, no. 4, pp. 219–256, 2004.
[82] K. Sunada, T. Watanabe, and K. Hashimoto, “Studies on photokilling of bacteria on TiO2 thin film,” *J. Photochem. Photobiol. A*, vol. 156, no. 1–3, pp. 227–233, 2003.
[83] J. Gamage and Z. Zhang, “Applications of Photocatalytic Disinfection,” *Int. J. Photoenergy*, vol. 2010, pp. 1–11, 2010.
[84] L. W. Gassie and J. D. Englehardt, “Advanced oxidation and disinfection processes for onsite net-zero greywater reuse : A review,” *Water Res.*, vol. 125, pp. 384–399, 2017.
[85] N. Serpone *et al.*, “Standardization protocol of process efficiencies and activation parameters in heterogeneous photocatalysis: Relative photonic efficiencies ζr,” *J. Photochem. Photobiol. A Chem.*, vol. 94, no. 2–3, pp. 191–203, 1996.
[86] D. C. Hurum, A. G. Agrios, K. A. Gray, T. Rajh, and M. C. Thurnauer, “ Explaining the Enhanced Photocatalytic Activity of Degussa P25 Mixed-Phase TiO 2 Using EPR ,” *J. Phys. Chem. B*, vol. 107, no. 19, pp. 4545–4549, 2003.
[87] C. Reyes *et al.*, “Degradation and inactivation of tetracycline by TiO 2 photocatalysis,” *J. Photochem. Photobiol. A Chem.*, vol. 184, no. 1–2, pp. 141–146, 2006.
[88] M. Subramanian and A. Kannan, “Photocatalytic degradation of phenol in a rotating annular reactor,” *Chem. Eng. Sci.*, vol. 65, pp. 2727–2740, 2010.
[89] M. Izadifard, G. Achari, and C. Langford, “Application of Photocatalysts and LED Light Sources in Drinking Water Treatment,” *Catalysts*, vol. 3, no. 3, pp. 726–743, 2013.
[90] M. A. I. Molla, I. Tateishi, M. Furukawa, H. Katsumata, T. Suzuki, and S. Kaneco, “Photocatalytic Decolorization of Dye with Self-Dye-Sensitization under Fluorescent Light Irradiation,” *ChemEngineering*, vol. 1, no. 2, p. 8, 2017.

[91] A. Mills and S. Le Hunte, "An overview of semiconductor photocatalysis," *J. Photochem. Photobiol. A Chem.*, vol. 108, no. 1, pp. 1–35, 1997.
[92] M. R. Hoffmann, S. T. Martin, W. Choi, and D. W. Bahnemannt, "Environmental Applications of Semiconductor Photocatalysis," pp. 69–96, 1995.
[93] D. F. Ollis, E. Pelizzetti, and N. Serpone, *Photocatalysis*. New York: Wiley Interscience, 1989.
[94] J. M. Herrmann, "Heterogeneous photocatalysis: Fundamentals and applications to the removal of various types of aqueous pollutants," *Catal. Today*, vol. 53, no. 1, pp. 115–129, 1999.
[95] U. I. Gaya, "Heterogeneous photocatalysis using inorganic semiconductor solids," *Heterog. Photocatal. Using Inorg. Semicond. Solids*, vol. 9789400777, pp. 1–213, 2014.
[96] J. Theurich, M. Lindner, and D. W. Bahnemann, "Photocatalytic Degradation of 4-Chlorophenol in Aerated Aqueous Titanium Dioxide Suspensions: A Kinetic and Mechanistic Study," *Langmuir*, vol. 12, no. 26, pp. 6368–6376, 1996.
[97] J. G. Calvert and J. N. Pitts, *Photochemistry*. New York: Wiley, 1966.
[98] S. Nick, "Relative photonic efficiencies and quantum yields in heterogeneous photocatalysis," *J. Photochem. Photobiol. A Chem.*, vol. 104, no. 1–3, pp. 1–12, 1997.
[99] C. Turchi and D. F. Ollis, "Photocatalytic Degradation of Organic Water Contaminants: Mechanisms Involving Hydroxyl Radical Attack," *J. Catal.*, vol. 122, no. 1, pp. 178–192, 1990.
[100] J. M. Herrmann, "Heterogeneous photocatalysis: State of the art and present applications," *Top. Catal.*, vol. 34, no. 1–4, pp. 49–65, 2005.
[101] K. Kabra, R. Chaudhary, and R. L. Sawhney, "Treatment of Hazardous Organic and Inorganic Compounds through Aqueous-Phase Photocatalysis: A Review," *Treat. Hazard. Org. Inorg. Compd. through Aqueous-Phase Photocatal. A Rev.*, vol. 43, pp. 7683–7696, 2004.
[102] I. Boiarkina, S. Norris, and D. Alec, "The case for the photocatalytic spinning disc reactor as a process intensification technology : Comparison to an annular reactor for the degradation of methylene blue," *Chem. Eng. J.*, vol. 225, pp. 752–765, 2013.
[103] M. de los M. Ballari, R. Brandi, O. Alfano, and A. Cassano, "Mass transfer limitations in photocatalytic reactors employing titanium dioxide suspensions. I. Concentration profiles in the bulk," *Chem. Eng. J.*, vol. 136, no. 1, pp. 50–65, 2008.
[104] A. Bernabeu *et al.*, "Solar photocatalysis as a tertiary treatment to remove emerging pollutants from wastewater treatment plant effluents," *Catal. Today*, vol. 161, no. 1, pp. 235–240, Mar. 2011.
[105] S. Malato, P. Fernández-Ibáñez, M. I. Maldonado, J. Blanco, and W. Gernjak, "Decontamination and disinfection of water by solar photocatalysis: Recent overview and trends," *Catal. Today*, vol. 147, no. 1, pp. 1–59, 2009.
[106] P. Fernández, J. Blanco, C. Sichel, and S. Malato, "Water disinfection by solar photocatalysis using compound parabolic collectors," *Catal. Today*, vol. 101, no. 3–4 SPEC. ISS., pp. 345–352, 2005.
[107] D. Y. Goswami *et al.*, "Solar Photocatalytic Treatment of Groundwater at

Tyndall AFB: Field Test Results," in *Proceedings of the 1993 Annual Conference of American Solar Energy Society*, 1993, pp. 235–239.
[108] J. Crittenden, Y. Zhang, D. Hand, D. Perram, and E. Marchand, "Solar detoxification of fuel-contaminated groundwater using fixed-bed photocatalysts," *Water Environ. Res.*, vol. 68, no. 3, pp. 270–278, 1996.
[109] A. H. C. Chan, C. K. Chan, J. P. Barford, and J. F. Porter, "Solar photocatalytic thin film cascade reactor for treatment of benzoic acid containing wastewater," *Water Res.*, vol. 37, no. 5, pp. 1125–1135, 2003.
[110] S. J. Khan, R. H. Reed, and M. G. Rasul, "Thin-film fixed-bed reactor for solar photocatalytic inactivation of Aeromonas hydrophila: Influence of water quality," *BMC Microbiol.*, vol. 12, 2012.
[111] D. Bahnemann, "Photocatalytic water treatment: Solar energy applications," *Sol. Energy*, vol. 77, no. 5, pp. 445–459, 2004.
[112] E. F. Duffy *et al.*, "A novel TiO2-assisted solar photocatalytic batch-process disinfection reactor for the treatment of biological and chemical contaminants in domestic drinking water in developing countries," *Sol. Energy*, vol. 77, no. 5, pp. 649–655, 2004.
[113] D. M. A. Alrousan, M. I. Polo-López, P. S. M. Dunlop, P. Fernández-Ibáñez, and J. A. Byrne, "Solar photocatalytic disinfection of water with immobilised titanium dioxide in re-circulating flow CPC reactors," *Appl. Catal. B Environ.*, vol. 128, pp. 126–134, 2012.
[114] J. A. Byrne *et al.*, "A review of heterogeneous photocatalysis for water and surface disinfection," *Molecules*, vol. 20, no. 4, pp. 5574–5615, 2015.
[115] C. Sordo, R. Van Grieken, J. Marugán, and P. Fernández-Ibáñez, "Solar photocatalytic disinfection with immobilised TiO2at pilot-plant scale," *Water Sci. Technol.*, vol. 61, no. 2, pp. 507–512, 2010.
[116] R. E. Marinangeli and D. F. Ollls, "Photoassisted Heterogeneous CataIysis with Optical Fibers: Part I: Isolated Single Fiber," vol. 1649, no. 1951, pp. 415–426, 1977.
[117] R. E. Marinangeli and D. F. Ollis, "Photo-assisted heterogeneous catalysis with optical fibers II. Nonisothermal single fiber and fiber bundle," *AIChE J.*, vol. 26, no. 6, pp. 1000–1008, 1980.
[118] R. E. Marinangeli and D. F. Ollis, "Photo-assisted heterogeneous catalysis with optical fibers: Part III: Photoelectrodes," *AlChE J.*, vol. 28, no. 6, pp. 945–955, 1982.
[119] N. J. Peill and M. R. Hoffmann, "Chemical and physical characterization of a TiO2-coated fiber optic cable reactor," *Environ. Sci. Technol.*, vol. 30, no. 9, pp. 2806–2812, 1996.
[120] W. Wang and Y. Ku, "The light transmission and distribution in an optical fiber coated with TiO2 particles," *Chemosphere*, vol. 50, no. 8, pp. 999–1006, 2003.
[121] H. Lin and K. T. Valsaraj, "An optical fiber monolith reactor for photocatalytic wastewater treatment," *AIChE J.*, vol. 52, no. 6, pp. 2271–2280, 2006.
[122] N. J. Peill and M. R. Hoffmann, "Fiber-Optic Cable Reactor for Waste Stream Remediation," *J. Sol. Eneergy Eng.*, vol. 119, no. August, pp. 229–236, 1997.
[123] H. O'Neal Tugaoen, S. Garcia-Segura, K. Hristovski, and P. Westerhoff, "Compact light-emitting diode optical fiber immobilized TiO2 reactor for

photocatalytic water treatment," *Sci. Total Environ.*, vol. 613–614, pp. 1331–1338, 2018.
[124] A. Danion, J. Disdier, C. Guillard, and N. Jaffrezic-Renault, "Malic acid photocatalytic degradation using a TiO2-coated optical fiber reactor," *J. Photochem. Photobiol. A Chem.*, vol. 190, no. 1, pp. 135–140, 2007.
[125] Z. Ji, D. M. Callahan, M. N. Ismail, J. Warzywoda, and A. Sacco, "Development and characterization of a titanosilicate ETS-10-coated optical fiber reactor towards the photodegradation of methylene blue," *J. Photochem. Photobiol. A Chem.*, vol. 217, no. 1, pp. 22–28, 2011.
[126] K. Hofstadler and S. Novalic, "New Reactor Design for Photocatalytic Wastewater Treatment with Ti02 Immobilized on Fused-Silica Glass Fibers: Photomineralization of 4-Chlorophenol," *Environ. Sci. Technol.*, vol. 28, no. 4, pp. 670–674, 1994.
[127] L. W. Miller, M. I. Tejedor-Tejedor, and M. A. Anderson, "Titanium dioxide-coated silica waveguides for the photocatalytic oxidation of formic acid in water," *Environ. Sci. Technol.*, vol. 33, no. 12, pp. 2070–2075, 1999.
[128] A. Usami and H. Ozaki, "Optical Modeling of Nanocrystalline TiO 2 Films," *J. Phys. Chem. B*, pp. 2591–2596, 2005.
[129] N. J. Peill and M. R. Hoffmann, "Development and Optimization of a TiO2-Coated Fiber-Optic Cable Reactor: Photocatalytic Degradation of 4-Chlorophenol," *Environ. Sci. Technol.*, vol. 29, no. 12, pp. 2974–2981, 1995.
[130] M. Castellote and N. Bengtsson, "Applications of Titanium Dioxide Photocatalysis to Construction Materials," 2011.
[131] W. Choi, J. Y. Ko, H. Park, and J. S. Chung, "Investigation on TiO 2 -coated optical fibers for gas-phase photocatalytic oxidation of acetone," vol. 31, pp. 209–220, 2001.
[132] A. Danion, J. Disdier, C. Guillard, F. Abdelmalek, and N. Jaffrezic-Renault, "Characterization and study of a single-TiO2-coated optical fiber reactor," *Appl. Catal. B Environ.*, vol. 52, no. 3, pp. 213–223, 2004.
[133] A. Gross, A. Maimon, Y. Alfiya, and E. Friedler, *Grey Water Reuse*. CPC Press, 2015.
[134] C. Chini, M. Konar, and A. Stillwell, "Direct and indirect urban water footprints of the United States," *Water Resour. Res.*, vol. 51, pp. 9127–9140, 2015.
[135] M. P. Gutierrez and L. P. Lee, "Multiscale design and integration of sustainable building functions," *Science (80-.).*, vol. 341, no. 6143, pp. 247–248, 2013.
[136] C. Lamnatou, J. D. Mondol, D. Chemisana, and C. Maurer, "Modelling and simulation of Building-Integrated solar thermal systems: Behaviour of the coupled building/system configuration," *Renew. Sustain. Energy Rev.*, vol. 48, pp. 178–191, 2015.
[137] C. S. Park, G. Augenbroe, T. Messadi, M. Thitisawat, and N. Sadegh, "Calibration of a lumped simulation model for double-skin façade systems," *Energy Build.*, vol. 36, no. 11, pp. 1117–1130, 2004.
[138] T. Matuska and B. Sourek, "Façade solar collectors," *Sol. Energy*, vol. 80, no. 11, pp. 1443–1452, 2006.
[139] I. Bergmann and W. Weiss, "Fassandenintegration von thermiscen Sonnenkollektoren ohne Hinterlueftung," *Berichte aus Energ. - und*

Umweltforsch., vol. 13, 2002.
[140] M. S. Buker and S. B. Riffat, "Building integrated solar thermal collectors - A review," *Renew. Sustain. Energy Rev.*, vol. 51, pp. 327–346, 2015.
[141] C. Maurer, C. Cappel, and T. E. Kuhn, "Progress in building-integrated solar thermal systems," *Sol. Energy*, vol. 154, pp. 158–186, 2017.
[142] T. T. Chow, "A review on photovoltaic/thermal hybrid solar technology," *Appl. Energy*, vol. 87, no. 2, pp. 365–379, 2010.
[143] S. Krauter *et al.*, "Combined photovoltaic and solar thermal systems for facade integration and building insulation," *Sol. Energy*, vol. 67, no. 4–6, pp. 239–248, 2002.
[144] J. Ji, T. T. Chow, and W. He, "Dynamic performance of hybrid photovoltaic/thermal collector wall in Hong Kong," *Build. Environ.*, vol. 38, no. 11, pp. 1327–1334, 2003.
[145] I. Visa, M. Moldovan, M. Comsit, M. Neagoe, and A. Duta, "Facades Integrated Solar-thermal Collectors - Challenges and Solutions," *Energy Procedia*, vol. 112, no. October 2016, pp. 176–185, 2017.
[146] T. Granata, M. Krehel, S. Wittkopf, and M. Egli, "a Hybrid Facade That Combines an Algal Bioreactor With Photovoltaics," *Proc. Int. Conf. CISBAT 2015 Futur. Build. Dist. Sustain. from Nano to Urban Scale*, vol. 2, pp. 567–572, 2015.
[147] B. Wu, "Membrane-based technology in greywater reclamation: A review," *Sci. Total Environ.*, vol. 656, pp. 184–200, 2019.
[148] N. D. VanWoert, D. B. Rowe, J. A. Andersen, C. L. Rught, R. T. Fernandez, and L. Xiao, "Green roof stormwater retention: effects of roof surface, slope, and media depth," *J. Environ. Qual.*, vol. 34, pp. 1036–1044, 2005.
[149] C. Cappel, W. Streicher, F. Lichtblau, and C. Maurer, "Barriers to the market penetration of façade-integrated solar thermal systems," *Energy Procedia*, vol. 48, pp. 1336–1344, 2014.
[150] D. E. Attoye, T. O. Adekunle, K. A. T. Aoul, and H. Ahmed, "Building Integrated Photovoltaic (BIPV) Adoption : A conceptual Communication Model for Research and Market Proposals," vol. 06117, no. April, pp. 1–7, 2018.
[151] M. C. Munari Probst and C. Roecker, "Criteria for architectural integration of active solar systems IEA Task 41, Subtask A," *Energy Procedia*, vol. 30, pp. 1195–1204, 2012.
[152] S. Beale, "Fluid Flow and Heat Transfer in Tube Banks," Dissertation, Imperial College of Science, Technology, and Medicine, 1992.

Chapter II:
Particle Interception on Cylindrical Collectors in Moderate Laminar Flow

I. Introduction:

Parallel cylindrical array collector systems play an important role in a variety of engineered and natural systems, from heat exchangers to filtration, because of their well-defined geometry and excellent heat and mass transfer performance. [1], [2] Crucial to the successful application of tube banks is a careful understanding of particle collection, which governs a variety of application-specific phenomena from fouling and mechanical erosion in heat exchangers to filtration and disinfection of bacteria in water treatment systems. [3]

The collection of colloidal particles on cylindrical bodies takes place via a number of recognized mechanisms, and each system needs to be assessed to see which of these mechanisms is relevant. For example, in gas cleaning, *inertial impaction* and *interception* are dominant for particles ≥ 1 μm in diameter. [4] *Convective/diffusive* transport is considered a minor effect for particles this large due to their size and corresponding small diffusion coefficient. *Electrostatic* mechanisms of collection are also considered for bodies of varying charge. The effectiveness of a collector for a given flow and particle type is represented by a calculation of efficiency (η), the ratio of the fluid stream volume flow within which particles are collected to the superficial flow rate.

This Chapter is focused on filtration for micro-scale particles in aqueous laminar flow. Little is known about micro-scale (particles on the order of 10 - 0.1 micron diameter) particle interception in liquid laminar flow tube bank systems, an engineering configuration with applications in water disinfection and heat exchange. [5] This system places constraints on the mechanisms at play in particle filtration, both due to the mechanisms of filtration and the geometry of the system itself.

In this system:

1) Interception dominates collection. The Stokes number, a non-dimensional ratio of the particle travel time scale to the obstacle length scale, is several orders of magnitude lower than the critical Stokes number (≈ 1) required for inertial impaction to be significant. [6] Electro-static mechanisms are similarly hampered in a relatively dense fluid medium, and diffusion is also minimal for particles the size of a representative of particles of interest (e.g., *E. coli* cells, diameter ~ 1um). [7]

2) Though particle filtration theory has been well-developed for aerosol flows [8], water studies have primarily been performed in the creeping flow regime, such as for groundwater filtration [9], [10], however these source fields give no information

about interception in the moderate laminar range of flow. Studies for particle collection on single cylinders in aqueous flow have been done experimentally [11], [12] and numerically [13] for laminar flow and are useful for examining low Reynolds number flows. In section 2.1 we explain how this study is qualitatively different in a fundamental manner due to the flow restrictions that a tube bank imposes on the flow around collectors due limitations imposed on vortex shedding and retardation of the transitional flow regime behavior, in particular on the persistence of low pressure vortices behind cylinders at advanced superficial flow rates. For these reasons, while the studies of Palmer and Ghisalberti are certainly pertinent to the marine environment, for tube banks a new study must be carried out to determine particle collection for laminar non-creeping flow in packed cylinder beds.

3) Little is known about the effect of multiple adjacent collectors on interception efficiency in this regime. In general, collection efficiencies are calculated by one of two models for the flow field: potential flow used for Re>1000, describing the transitional/turbulent regime for flow over a cylinder, and a viscous (creeping) flow model for Re<1. [14] Friedlander's research in aerosol filtration has produced correlations for particle interception and diffusion for Reynolds numbers between 10^2 and 10^4, however these models are calculated from flow over single cylinder/sphere flow models. [15] The effect of adjacent collectors on the flow field is not considered explicitly in this model and thus must be combined with other fiber filter models to estimate the effect of adjacent collectors on particle removal.

An approach to describing interactions between nearby collectors on the flow field is known as the "cell model". Two models are commonly used to this effect, the free surface cell model described by Happel, and the zero vorticity cell model described by Kuwabara. [16], [17] These models assume that the collector exists in a fluid envelope and can be isolated from others by a cell boundary condition, zero shear in the free surface model, and zero vorticity in the latter. These models assume a given void fraction that defines the relative size of the cylinder/sphere to the envelope, and that the cell does not interact with adjacent cells. The zero vorticity model is not widely used due to the fact that it is difficult to assume zero vorticity in a real world system where it is highly likely that adjacent cells will be exchanging energy, and this is especially true for the current system where regular vortices will develop in the cylinder flow field. These cell models are directly applied as a factor for a given void fraction to the collection efficiency of a single sphere/cylinder. [18] Both models were developed for creeping incompressible flows (Re<1), and cannot be directly applied to moderate laminar flows (where there is both adverse pressure and vorticity). These models say nothing about the moderate laminar flow regime for particle interception theory, and the problem of determining the effect of adjacent collectors on particle interception efficiency in this flow regime currently has no rigorous definition. [19]

In this work, we seek to describe tube bank particle interception efficiency, specifically addressing the constraints of the aforementioned conditions: moderate

laminar, low Stokes number fluid flows. In investigating the colloidal filtration processes for the system we are analyzing it was determined that there was a paucity of literature on the subject of 1) particle interception in water for the range of laminar flows considered (100<Re<500 in a tube bank), and 2) the effect of adjacent collectors on the flow field and their direct effect on interception efficiency in this flow regime. Specifically, we look at particle interception in water flow in the moderate laminar range of Reynolds numbers over a staggered cylinder arrangement using numerical methods. The results of our numerical simulations will be compared to correlations and analytical models currently in use.

II. Method: Definition of the Model

2.1: Flow Field over staggered arrays of cylinders

The fluid flow field normal to an array of cylinders in the staggered arrangement has been extensively described by Žukauskas. [20] An image of the basic staggered geometry is presented in Figure 2.1 (see Eqs. 2.4-2.6 for a description of the variables):

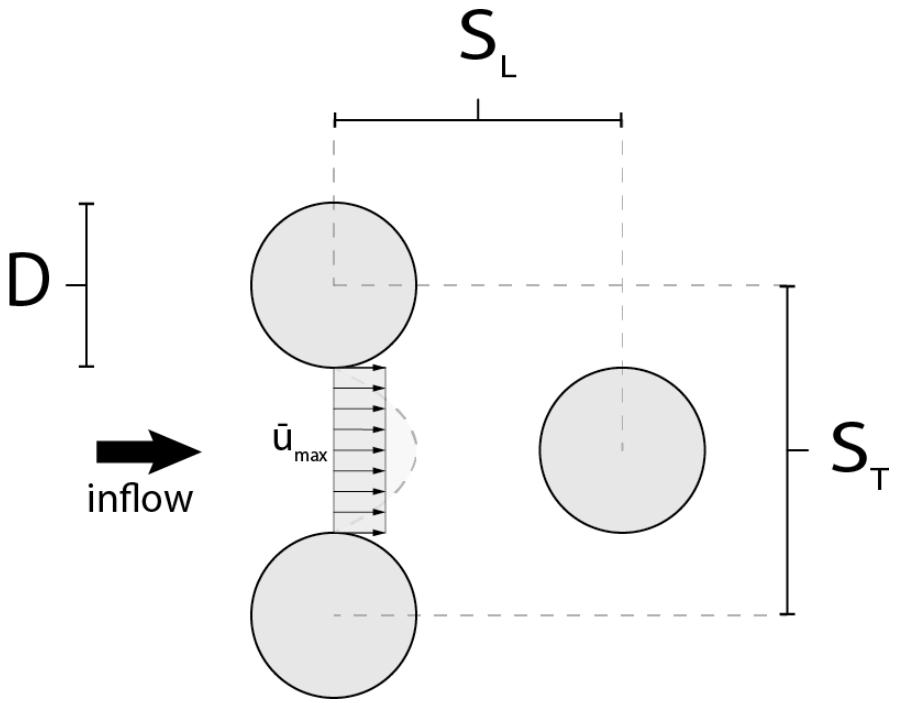

Figure 2.1: Staggered cylinder geometry and variables of interest

Žukauskas conducted his own experiments as well as tabulated the results of other studies in an effort to describe pressure drop and heat transfer correlations for tube bank heat exchangers. Using Žukauskas' experimental work, Beale defined finite difference numerical models for the flow field and heat transfer in this type of heat exchanger employing the SIMPLE algorithm of Patankar. [21], [22] The regularly

staggered tube bank flow field is identical in the two systems, and is what we use as a basis for modeling adjacent cylinders in this study.

Several aspects of the system are given detail via Žukauskas' studies, specifically the effect of the adjacent cylinders on constraining the adverse pressure gradient. For a single cylinder the lack of physical constraint leads to the development of vortex shedding at relatively low Reynolds numbers (~50-80), leading to transitional flow regime where unsteady vortex shedding (the Karman vortex street) occurs. In cross flow over staggered cylinder arrays, the adverse pressure gradient is constrained due to the presence of other nearby cylinders [20]. The resulting flow field remains regular for steady inflow up to much greater flow rates, remaining laminar (pre-transitional regime, non-turbulent eddy forming) with regular vortices forming behind the cylinders up to Re < 500-1000. Further, it was determined that in the laminar regime the velocity distribution over the cylinder banks became highly regular after the third row [20]. This information allows us to develop a numerical model that fits the expected flow pattern closely.

2.2: Numerical Modeling

The numerical model for our 2D flow simulation was developed in a Finite Element CFD software environment, COMSOL (v5.0), for laminar single-phase flow. The governing equations were the 2D steady state incompressible Navier-Stokes and continuity equations:

$$\begin{aligned} -\nu\left(\frac{\partial^2 u}{\partial x^2}+\frac{\partial^2 u}{\partial y^2}\right)+u\frac{\partial u}{\partial x}+v\frac{\partial u}{\partial y}+\frac{\partial p}{\partial x} &= 0 \\ -\nu\left(\frac{\partial^2 v}{\partial x^2}+\frac{\partial^2 v}{\partial y^2}\right)+u\frac{\partial v}{\partial x}+v\frac{\partial v}{\partial y}+\frac{\partial p}{\partial y} &= 0 \\ \frac{\partial u}{\partial x}+\frac{\partial v}{\partial y} &= 0 \end{aligned} \tag{1}$$

The cylinder geometry was defined as a series of cells, as seen in Figure 2.2. The linear triangular element size in the bulk of the fluid was extremely fine (3.5e6 triangular elements) with a layer of 100 quadrilateral boundary elements at the cylinder and symmetry edges. This resolution was necessary to capture the streamlines of interest with numerical convergence. No-slip conditions were set at the cylinder walls, and symmetry at the horizontal cell boundaries to generate the regular vortex formation expected for this flow regime. At the inlet of the cylinder cell series an average inflow velocity was set, and a zero pressure condition for the outflow. In the figure of the model (Fig. 2.2), the void space appears dark due to the density of the elements.

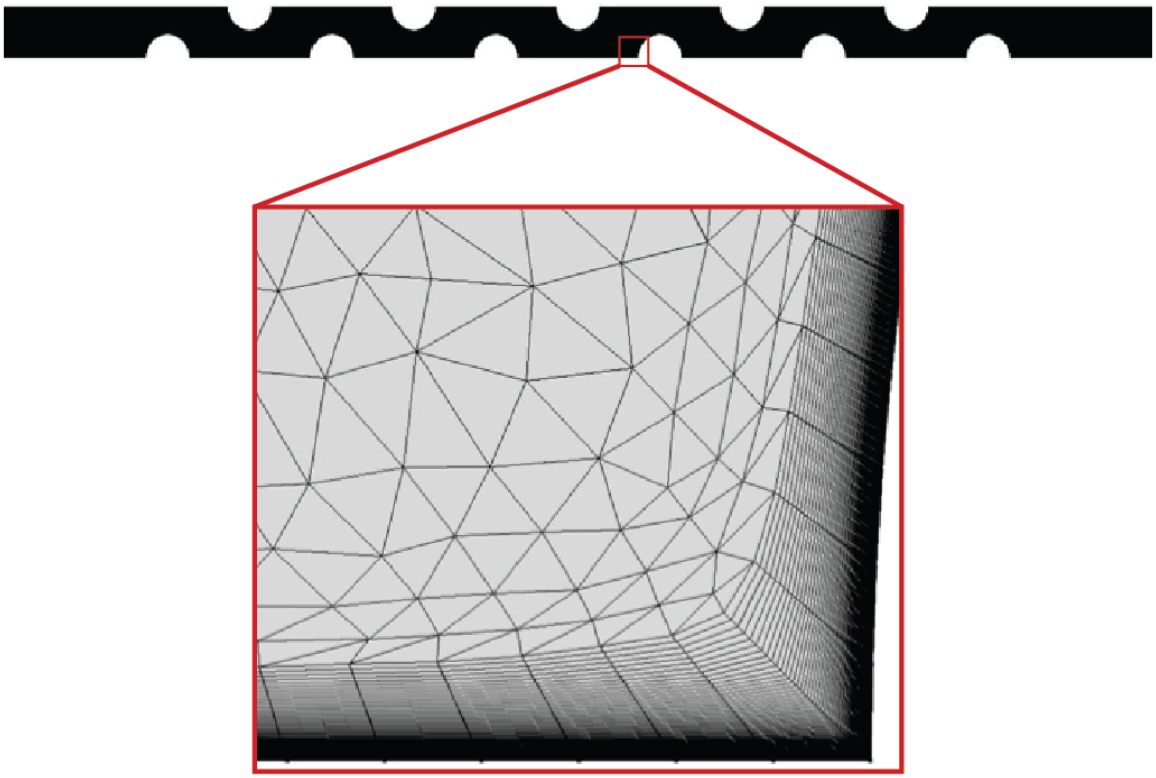

Figure 2.2: Simulation geometry and boundary layer mesh

A non-dimensionalization of the drag/pressure drop across a row of cylinders shows four groups of interest:

$$\frac{dP}{\rho \bar{U}_{max}{}^2} = Eu \quad \text{(Dimensionless pressure drop over a row)} \tag{2}$$

$$\frac{\rho \bar{U}_{max} D}{\mu} = Re \quad \text{(Reynolds Number)} \tag{3}$$

$$\frac{S_T}{D} = a \quad \text{(ratio of transverse spacing to diameter of cylinder)} \tag{4}$$

$$\frac{S_L}{D} = b \quad \text{(ratio of longitudinal spacing to diameter of cylinder)} \tag{5}$$

The parameters *a* and *b* (see Fig. 1) define the staggered geometry of the cylinder packing. In the numerical studies presented here the diameter is fixed at a unit (1cm) while the transverse and longitudinal spacing are parameterized in tandem (maintaining equilateral staggered geometry) to produce a variable solid fraction.

2.3: U_{max} variation

The Reynolds number used in the experimental data of Žukauskas was derived from the average maximum velocity of the flow in the tube bank, occurring at the

minimum cross section of the tube banks, owing to continuity. The minimum cross section occurs in the vertical spacing of the cylinders and the average maximum velocity used to generate the Reynolds number is defined as:

$$\overline{U}_{max} = U_{avg} * \left[\frac{S_T}{S_T - D}\right] \quad (6)$$

The results of our numerical studies showed that this formulation tended to under estimate the actual average velocity at the entrance to the cylinder cell at higher inlet velocities by about 5%. For our studies we used the average maximum velocity from the numerical results in the calculation of Re_{max}.

The numerical pressure drop studies from Beale offer a benchmark for the flow field generated by our simulations to assess the validity of our model. [23] Beale collated all previous major experimental work for cross flow over tube banks and compared them to his numerical simulations. Our own studies are consistent with this previous work, and provided confidence that we were moving forward into particle interception studies with a viable numerical flow model.

III: Review - Particle interception over single cylinders

The primary factor in the effectiveness of particle interception is the dimensionless ratio of the particle diameter to the collector diameter, $R = \frac{d_{part}}{D_{cyl}}$. The theory of particle interception relies on detailing the streamlines of the flow fields, and defining the critical streamline that which comes within a minimum distance to the collector of one particle radius. Friedlander developed a correlation based the critical streamline for flow over the front half of a single cylinder in the flow regime range $10^2 < Re < 10^4$, based Schlichting's detailed boundary layer calculations for flow over cylinders and spheres. [15], [24]

$$\eta_{pi,Fr} = 0.7982\, Re^{1/2} R^2 \quad (7)$$

Friedlander developed this correlation for particle interception analytically, and stated that it has not been tested for accuracy. [6,15]

The unit staggered cylinder arrangement (cylinder diameter 1unit, equilateral triangle geometry, a=2, b=$\sqrt{3}$) provides a place to begin to study the particle interception in a tube bank, where it is expected that the efficiency will be a function of Re_{max}, R, and solid fraction (sf = ½ $A_{cylinder}/A_{cell}$), the components contributing to the boundary layer thickness, correlating it with bacterial size, and the effects of other cylinders on the flow field respectively.

The method we employ is similar to the Friedlander's analytical development via Schlichting: for a given flow rate we find the critical streamline by transforming the streamline from the cylindrical orientation to Cartesian coordinates. Finding the

minimum of the transformed streamline then shows where non-inertial particles for the given *R* make the closest approach to the cylinder surface. It is assumed in this study that perfect collection is possible, that is, if the radius of the particle connects with the cylinder then interception has occurred. The area inside of this streamline is used for the calculation for particle interception efficiency (Eq. 8, below).

Holding *R* constant for all studies at 10^{-3}, we examine the effect of varying the Reynolds number and solid fraction of the staggered cylindrical packing on particle interception efficiency. It is assumed that the projected collector area in the efficiency calculation is always the diameter of the cylinder, not the inlet area to the staggered cylinder arrangement. The solid fractions range from 0.10, the lowest cylinder density where constraint of the vortices can be expected, to 0.65.

IV. Results:

4.1: Particle interception in a tube bank

The goal of gathering data on the particle interception over these cylinder arrays is to compare our results to the dimensionless components expected in the existing correlation ($Re^{1/2}\,R^2$). The efficiency is calculated numerically by:

$$\eta_{pi,num} = \frac{U_{avg,sl} A_{sl,crit}}{U_{sup} A_{proj,coll}} \tag{8}$$

where the average velocity in the numerator is the average velocity within the area swept out by the critical streamline at the entrance of the cell, and in the denominator is the superficial velocity of the bulk flow approaching the collector bed and the projected area of the collector (in this case equivalent to the diameter). This is essentially the proportion of the flow rates within the critical streamline to the system. It was expected that for all solid fractions particle interception efficiency would follow the $Re^{1/2}$ component of the Friedlander correlation (Eq. 7) and increase with solid fraction. The results detailed in figure 2.3 below show that this is largely the case, particularly at lower solid fractions, where the normalized efficiencies are close to constant for varying Re, except for higher solid fractions.

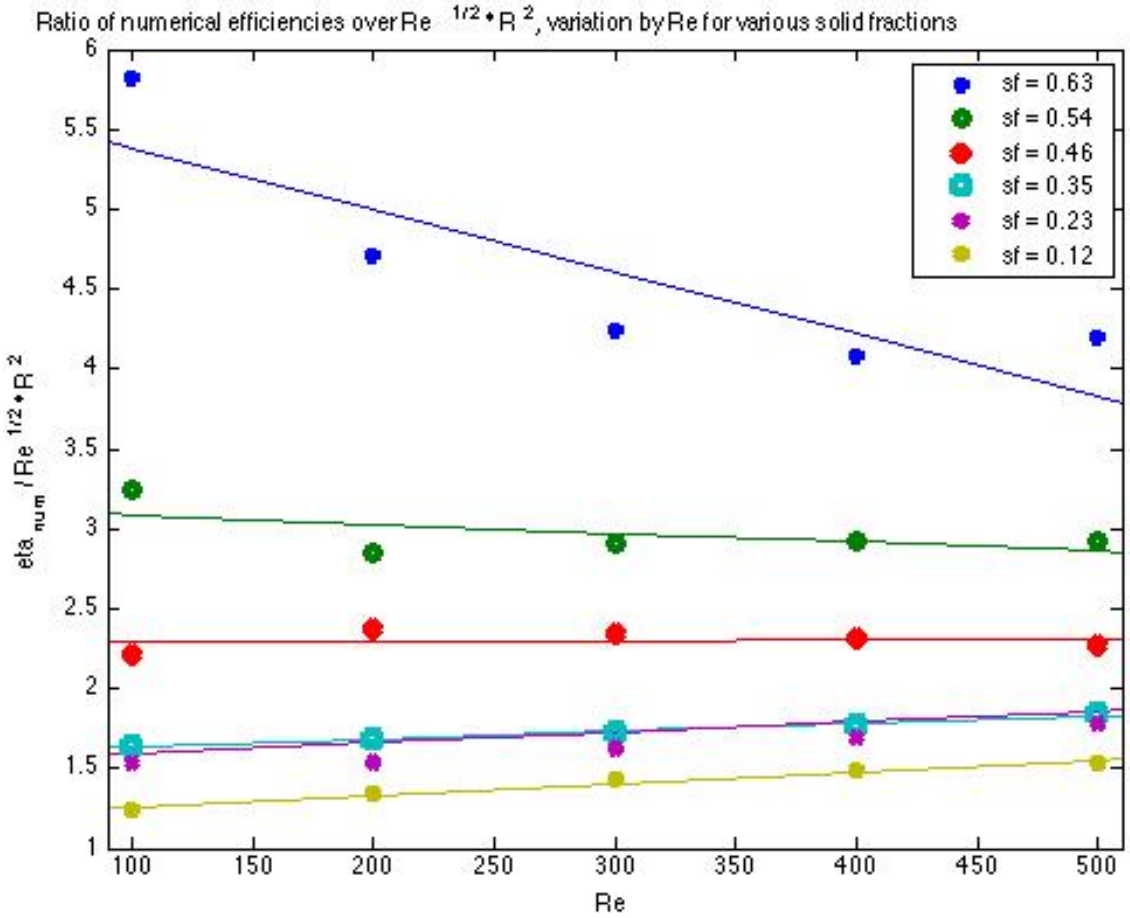

Figure 2.3: Ratio $\eta_{pi,num}$ / ($Re^{1/2}R^2$) by Re

The variation of efficiency by Reynolds number for the numerical studies show that the particle interception efficiency increases with increasing Re, but to a slightly greater linear degree than we would expect from the correlation alone. The ratio of efficiencies show that the numerical studies consistently give higher efficiencies than predicted by Friedlander, about 2 times as much at low solid fractions up to 7 times as much at higher solid fractions. This demonstrates the importance of considering the density of collectors in determining particle efficiency. When comparing the ratio of the various solid fraction efficiencies to the Friedlander correlation (Fig. 2.4), we observe that the ratio tends to remains close to constant by *Re*, except at the higher cylinder density where the ratio is convex parabolic across the Reynolds range, and is higher for lower *R*e. The average slope of the linear fits (normalized to the 1e2 *Re* range) is -3.4e-2, about a 3% grade. Most of this accounted for by the inconsistency in constancy for the greatest solid fraction. The normalization to $Re^{1/2}$ allows us to see that there is little variation by solid fraction for a changing Re, and that variations in the collection performance from the dimensionless components are found by varying the solid fraction.

The results for particle interception by solid fraction and their ratio to the dimensionless components of the Friedlander correlation are more interesting. The

results (Fig. 2.4) show a trend of increase in interception efficiency with increasing solid fraction, seen at all Reynolds numbers investigated. The normalization by $Re^{1/2}R^2$ shows that the variation in interception efficiency is almost entirely due to solid fraction, highlighting the importance of nearby collectors for interception in tube bank/fiber mat systems.

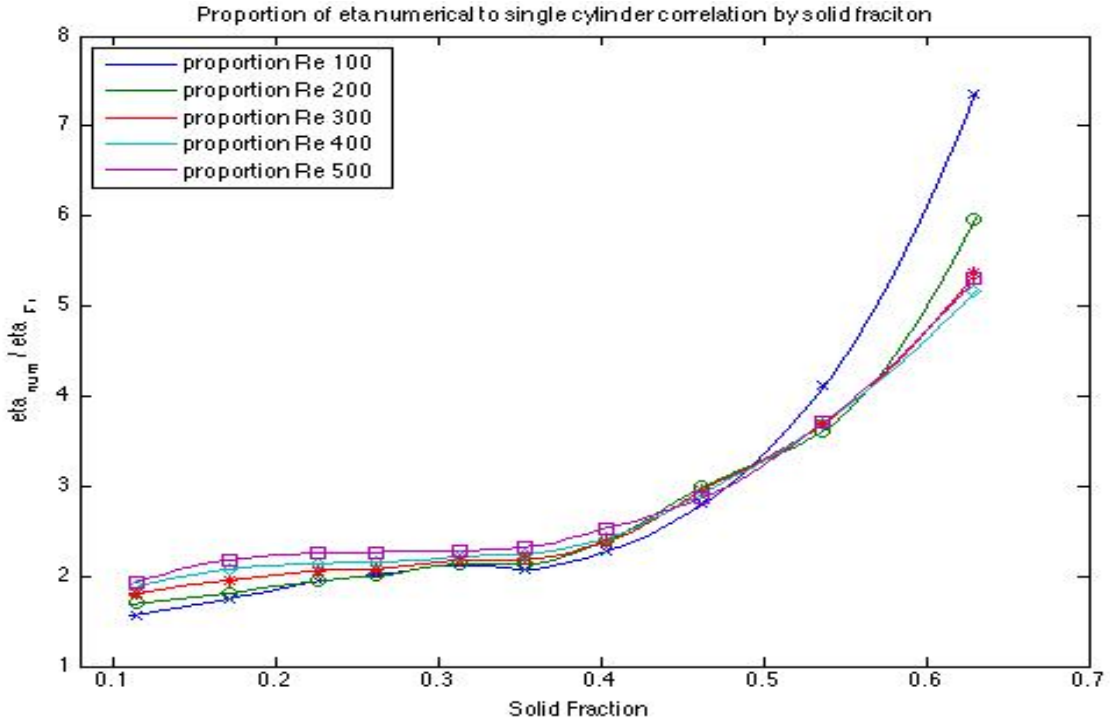

Figure 2.4: Particle interception efficiency η_{pi_num} normalized by $Re^{1/2}R^2$ by solid fraction for various *Re*

In the ratio of particle interception efficiencies of the numerical results to $Re^{1/2}R^2$ (Fig. 2.4), we see that the trend of the lines vary based on solid fraction alone, the dependence on Re seen only for lower Reynolds numbers at higher solid fractions. The variation in efficiency ratio by solid fraction is fit closely with a third order curve, although it could also be described as 'asymptotic' at the solid fraction limit. Special features of the trend in the proportional curves are a gradual increase from low solid fractions to a relatively constant value of two times the Friedlander correlation for solid fractions up to 0.35. After this point the proportion tends to increase more dramatically with solid fraction and is roughly the same for 250 < Re < 500. An interesting feature seen in both sets of data is that the ratio of particle interception efficiencies is greatest at lower Reynolds numbers for higher solid fractions.

V. Discussion:

5.1 Function Fit

The Friedlander correlation employs the potential flow assumption and is analytically sound for single cylinder flow in the Reynolds range we are interested in, but is experimentally untested. The dimensionless components in the correlation remain valid: the Reynolds number root describing the behavior of the boundary layer thickness (Fig. 2.3) and the square of the particle ratio describing the geometry of collision. The solid fraction is another dimensionless component that defines particle interception in tube bank systems (Fig.2.4). The form of the resulting correlation is:

$$\eta_{PI} = f(SF) * Re^{1/2} R^2 \tag{9}$$

where:

$$f(SF) = 47.9\, sf^3 - 35.4\, sf^2 + 9.43\, sf + 0.76 \tag{10}$$

Note that the constant found here (0.76) closely matches Friedlander's constant of 0.7982 for a vanishing solid fraction. A plot of the correlation with the data below:

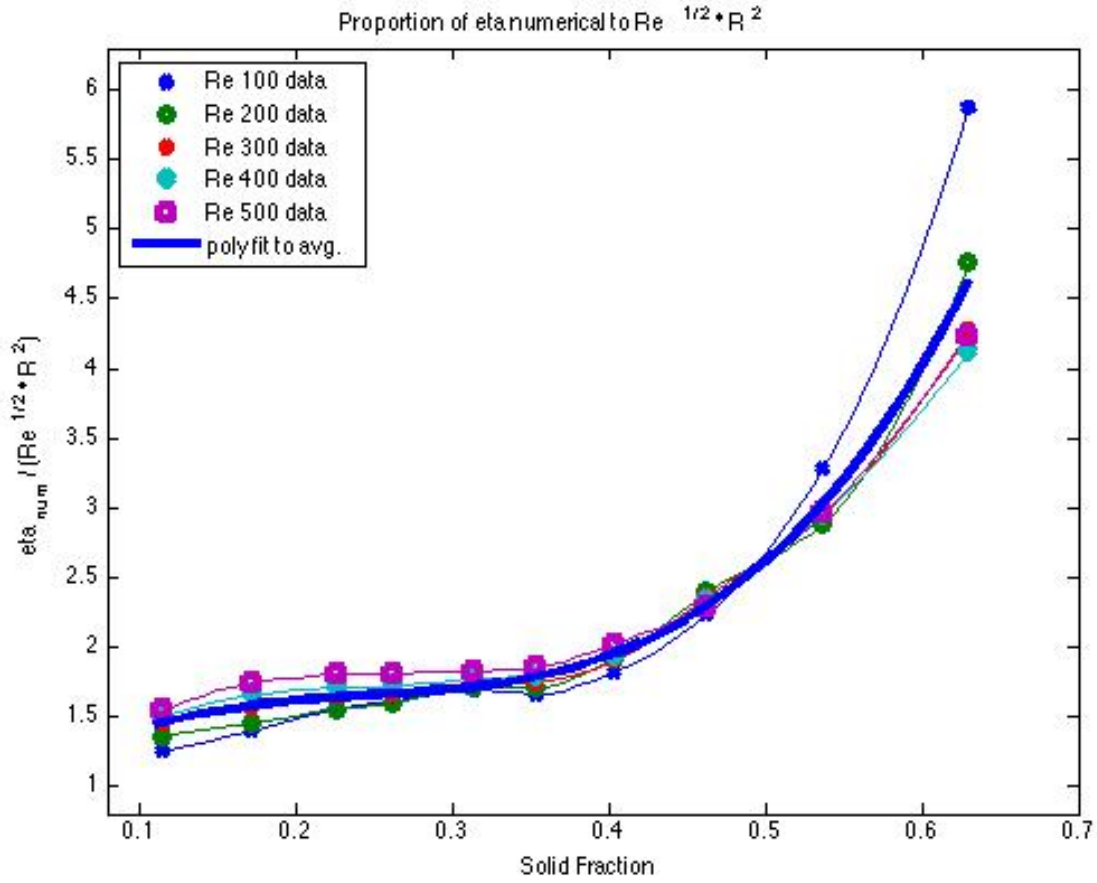

Figure 2.5: Normalized data with fit function, *f(SF)*

The adjusted R-square measure is 0.9993, and the root mean squared error (RMSE) is 0.029, giving confidence that the fit line to the average of the efficiencies in the Re range is accurate for the description of the proportional difference between the data and the correlation for the ranges ($0.1 < sf < 0.65$) and ($100 < Re < 500$) for cross flow over tube banks in the staggered configuration. The additional polynomial function in solid fraction normalized by $Re^{1/2}R^2$ covers the range of this system accurately, and opens further study on the effect of multiple collectors on particle interception in the flow regime of interest. However, extrapolation of $f(SF)$ outside of this regime has not been tested.

5.2 Analysis

The single cylinder correlation roughly follows the change in efficiency for a given solid fraction when parameterized by the Reynolds number, and is generally consistent with the expected $Re^{1/2}$ (except for lower Re, where it grows at higher solid fractions). Given that the depth of the boundary layer is considered to vary with this parameter in the same manner, this result makes physical sense and is not worth considering in greater detail. Interestingly, at the solid fraction minimum the correlation we give approaches the Friedlander analytical correlation for a single cylinder.

Looking more closely at the normalized graph we can see that interception efficiency becomes acutely sensitive to the influence of solid fraction past the value of 0.35. This is true for all superficial velocities in the laminar flow regime. Whereas before 0.35 the influence of solid fraction is relatively flat, past this critical value the interception efficiency increases exponentially thereafter for linear increase in the solid fraction.

The physics of the streamlines underlie the assumptions we use to find the minimum of the transformed streamline. In potential flow the closest approach is at the midpoint of the cylinder ($\theta = 90°$), where the velocity will increase to twice the velocity in the free stream. As the flow moves beyond the creeping flow regime to steady laminar without vortex shedding, the point of closest approach will move forward on the cylinder to 50 degrees at $Re = 500$. Our simulations correspond closely with the DNS solutions presented by Gayaso and Ghisalberti [25] for their numerical studies in the non-vortex shedding regime for particle capture over a single cylinder. This critical angle also corresponds with the maximum tangential velocity gradient and normal pressure gradient.

The point at which the derivative of the stream function with respect to the angular (or the x dimension after transform to Cartesian coordinates) is zero (the minimum on the transform to the Cartesian axis near the cylinder surface), this is also the point at which the velocity in the 'y' direction is zero (a local minimum), and thus the density of the streamlines in the radial/normal direction is a maximum where the gradient of the stream function has only a normal component. This normal component is the radial acceleration for flow over curved bodies:

$$\frac{d\varphi}{dy} = \frac{\bar{V}^2}{R_c} \tag{11}$$

Where R_c is the radius of curvature, in this case, 'unit'. [26] The dynamic pressure changes by location and cylinder packing while the superficial velocity is related to the velocity in the void spaces of the cylinder cell by flow rate equivalence:

$$\bar{V}_{system} = \frac{U_{sup}}{\epsilon} \tag{12}$$

where epsilon is the void fraction. By this relation we can relate proportionally the dynamic pressure to the streamline density via the solid fraction for tube bank flow, and thus to the location and proximity of the critical streamline:

$$q \propto \left(\frac{U_{sup}}{\epsilon}\right)^2 \propto \frac{1}{(1-SF)^2} \tag{13}$$

In the above correlation, we have already normalized the efficiency to flow relation by $Re^{1/2}$, and so the efficiency of the single cylinder would then be proportional to the constrained flow by:

$$q \propto \frac{1}{(1-SF)^{3/2}} \tag{14}$$

The density of the streamlines, the pressure gradient, is proportional to the fluid velocity in the voids, which is in turn inversely proportional to the void fraction. This proportion can then be applied to the single cylinder dimensionless components, seen below in figure 2.6:

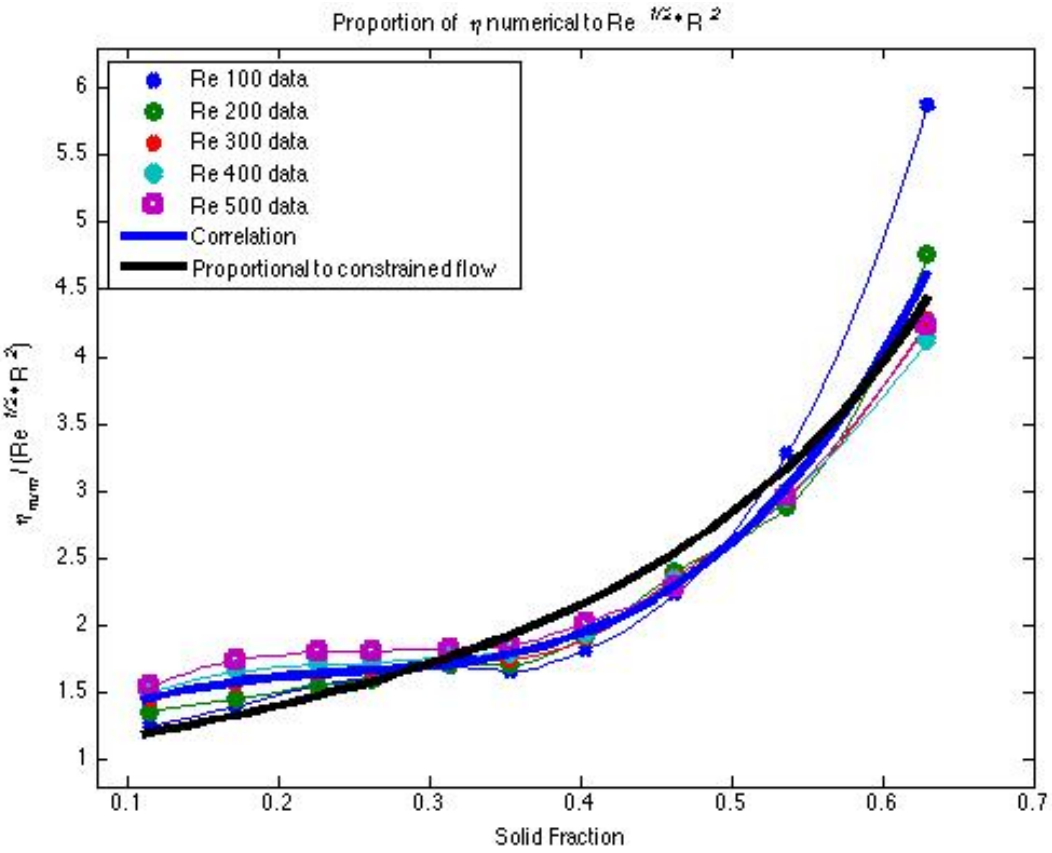

Figure 2.6: Asymptotic function fit to particle interception correlation based on solid fraction

While a fit corresponding to this type of asymptotic function roughly follows the trend of particle interception due to increase in solid fraction, the given polynomial correlation more accurately fits the numerical data. Still, this analysis still yields insight to the physical process of the particle interception efficiency change with increase in cylinder packing density. Beyond that, it offers a simple rule of thumb for estimating particle interception in this kind of cylinder matrix.

VI. Conclusion:

Designing removal systems where aqueous flow over cylinders occurs requires knowledge of the rate of particle deposition on the surface of cylinders. In the context of this work, particles are microbial cells that will be exposed to extremely short-lived radicals forming on the surface of cylinders. This analysis of particle capture due to interception in a regular collector array demonstrates significant differences between analytically derived correlations and numerical analyses using the same principles that were used to develop the original correlation due to variation in the flow field that occur with adjacent collectors. The multiple for the existing correlation accurately describes the variation with Reynolds number and solid fraction of a cylinder array. While the removal evidenced for the system

studied shows that the removal due to particle interception is not extremely significant in the CORE panel prototype, the difference between numerical analysis and analytically developed correlations is worthy of note, and suggests a direction for further study where the theory of filtration might be extended to account for the effect of adjacent cylinders in the moderate laminar flow range for fluids.

References:

[1] W. A. Khan, R. J. Culham, and M. M. Yovanovich, "Optimal Design of Tube Banks in Crossflow Using Entropy Generation Minimization Method," *J. Thermophys. Heat Transf.*, vol. 21, no. 2, pp. 372–378, 2007.

[2] H. Ibrahim, "Fouling in heat exchangers," in *MATLAB - A Fundamental Tool for Scientific Computing and Engineering Applications*, Vol. 3., V. Katsikis, Ed. 2012.

[3] S. Block, *Disinfection, Sterilization, and Preservation*, 5th ed. Philidelphia: Lippincott Williams and Wilkins, 2002.

[4] J. A. Siegel and W. W. Nazaroff, "Particle Deposition on HVAC Heat Exchangers," *Atmos. Environ.*, vol. 37, no. 39–40, pp. 5587–5596, 2003.

[5] V. K. Mandhani, R. P. Chhabra, and V. Eswaran, "Forced convection heat transfer in tube banks in cross flow," *Chem. Eng. Sci.*, vol. 57, no. 3, pp. 379–391, 2002.

[6] S. K. Friedlander, *Smoke, Dust, and Haze: Fundamentals of Aerosol Dynamics*, 2nd ed. New York: John Wiley & Sons, 2000.

[7] L. A. Spielman, "Particle Capture from Low-Speed Laminar Flows," *Annu. Rev. Fluid Mech.*, vol. 9, no. 1, pp. 297–319, 1977.

[8] N. A. Fuchs, *The Mechanisms of Aerosols*. London: Pergamon, 1964.

[9] R. Rajagopalan, "Trajectory AnaIysis of Deep-Bed Filtration with the Sphere-in-cell Porous Media Model," *AlChE J.*, vol. 22, no. 3, pp. 523–533, 1976.

[10] N. Tufenkji and M. Elimelech, "Correlation Equation for Predicting Single-Collector Efficiency in Physicochemical Filtration in Saturated Porous Media," *Environ. Sci. Technol.*, vol. 38, no. 2, pp. 529–536, 2004.

[11] M. R. Palmer, H. M. Nepf, and T. J. R. Pettersson, "Accumulation and Removal in Aquatic Systems," *Limnol. Oceanogr.*, vol. 49, no. 1, pp. 76–85, 2004.

[12] J. Shimeta and P. Jumars, "Physical mechanisms and rates of particle capture by suspension-feeders," *Ocean. Mar. Biol. Annu. rev.*, vol. 29, no. 1, pp. 191–257, 1991.

[13] A. Espinosa-Gayosso, M. Ghisalberti, G. N. Ivey, and N. L. Jones, "Particle capture by a circular cylinder in the vortex-shedding regime," *J. Fluid Mech.*, vol. 733, no. October, pp. 171–188, 2013.

[14] R. A. Pulley and J. K. Walters, "THE EFFECT OF INTERCEPTION ON PARTICLE COLLECTION," *J. Aerosol Sci.*, vol. 21, no. 6, pp. 733–743, 1990.

[15] R. Parnas and S. K. Friedlander, "Particle deposition by diffusion and interception from boundary layer flows," *Aerosol Sci. Technol.*, vol. 3, no. 1, pp. 3–8, 1984.

[16] J. Happel, "Viscous flow in multiparticle systems: Slow motion of fluids relative to beds of spherical particles," *AIChE J.*, vol. 4, no. 2, pp. 197–201, 1958.

[17] S. Kuwabara, "The Forces experienced by Randomly Distributed Parallel Circular Cylinders or Spheres in a Viscous Flow at Small Reynolds Numbers," *J. Phys. Soc. Japan*, vol. 14, no. 4, pp. 527–532, 1959.

[18] M. Clark, *Transport Modeling for Environmental Engineers and Scientists*, 2nd ed. New York: John Wiley & Sons, 2009.

[19] V. K. Satheesh, R. P. Chhabra, and V. Eswaran, “Steady incompressible fluid flow over a bundle of cylinders at moderate Reynolds numbers,” *Can. J. Chem. Eng.*, vol. 77, no. 5, pp. 978–987, 1999.
[20] A. Žukauskas, “Heat Transfer from Tubes in Crossflow,” *Adv. Heat Transf.*, vol. 18, pp. 87–159, 1987.
[21] S. B. Beale and D. B. Spalding, “NUMERICAL STUDY OF FLUID FLOW AND HEAT TRANSFER IN TUBE BANKS WITH STREAM-WISE PERIODIC BOUNDARY CONDITIONS,” *Trans. Can. Mech. Eng. Soc.*, vol. 22, no. 4A, pp. 397–416, 1998.
[22] S. V. Patankar and D. B. Spalding, “A Calculation Procedure for Heat, Mass and Momentum Transfer in Three-Dimensional Parabolic Flows,” *Int. J. Heat Mass Transf.*, vol. 15, pp. 1787–1806, 1972.
[23] S. Beale, “Fluid Flow and Heat Transfer in Tube Banks,” Imperial College of Science, Technology, and Medicine, 1992.
[24] H. Schlichting, *Boundary Layer Theory*, 4th ed. New York: McGraw Hill, 1967.
[25] A. Espinosa-Gayosso, M. Ghisalberti, G. N. Ivey, and N. L. Jones, “Particle capture and low-Reynolds-number flow around a circular cylinder,” *J. Fluid Mech.*, vol. 710, no. November, pp. 362–378, 2012.
[26] F. White, *VIscous Fluid Flow*, 2nd Ed. McGraw-Hill, 1991.

Chapter III:

Determining Surface Reaction Potential for Solar Photocatalytic Degradation of Methylene Blue Due to Light Transmitting Waveguides in Turbid Fluids: Experiments to Determine Waveguide Efficacy for Grey Water Remediation

I. Introduction:

In the past 40 years photocatalytic (PC) processes have been investigated for their potential to remove, via disinfection and mineralization, a number of contaminants in liquids and gasses, from bacteria to dyes. [1], [2] At first these studies focused on suspended titania powders, but difficulty removing these post treatment has led to research on fixed thin-film substrates. [3] However, fixed titania substrates result in mass transfer limitations due to lower surface area to volume ratios and low light energy utilization. [4] For this reason part of the research into fixed substrate photocatalysis has focused on process intensification in an effort to increase efficiency. [5], [6]

Environmental and sustainability concerns have spurred research into solar energy as the driver for a number of different applications. [7] While the UV light in the solar spectrum is a small portion of what reaches the earth (~4%), it is sufficient for solar photocatalysis TiO_2 catalysts. [8] Environmental concerns also extend to novel applications of PC technologies, such as building integrated platforms. [9]

Solar disinfection and water remediation have been tested and scaled for a number of applications, from the home to outlying communities with little infrastructure. [10] SODIS has been shown to be effective for bactericide as long as the sun shines, and the water has a relatively low level of turbidity (<30 NTU), however alternative methods (chemical and/or mechanical filtration) must be used in conjunction with SODIS in order to render the liquid clear for disinfection for turbid water. [11] For solar disinfection to be effective in removing bacteria, it requires time and several processes for any water that is initially more than slightly cloudy. SODIS is also not useful for mineralization of other organic pollutants in general.

The technology tested in this research is designed as a building integrated panel system for the recycling of greywater on site. CORE (Cylindrical Optical Reactive Elements) is a panel system using optical waveguides to irradiate photocatalytic surfaces for disinfection and reuse of greywater. The limitations of this application (solar powered, greywater medium, thin profile for façade integration) have contoured our design process, and have yielded a unique system toward this aim. The purpose of this study is to determine if CORE can operate directly on turbid greywater, or if significant pretreatment would be necessary.

Grey water is turbid, and highly absorbent in the UV as well as visible range of the solar spectrum. [12] Support-fixed photocatalysis requires high illuminated surface area to volume ratio for sufficient transport of pollutants to the reactive surfaces. In order to address both of these constraints, the CORE reactor design incorporates transparent waveguides: cylinders with immobilized photocatalyst on the surface. This design allows light to enter the fluid filled panel from any solar incident angle, reflect down the interior length of the cylinders, where UV light at each reflection will enter the TiO_2 layer and generate radicals at the TiO_2-water interface (Fig. 1). Previous studies on TiO_2 coated cylindrical waveguides for contaminant removal have been performed, where the mechanism of internal reflection is described for bulb and solar driven hydroxyl production. [13]–[17] These studies were performed primarily for gas cleaning, but UV transmission to the reactive surface applies in an aqueous medium as well. [18] However, none of these previous studies have taken into account an absorbing medium such as greywater, where incident UV light is absorbed and scattered by the high volume of particulates.

The aim of this work is to assess experimentally the potential for a novel building technology using nano-structured immobilized photocatalyst and solar power to remove pollutants from residential grey water, specifically to investigate the efficacy of waveguides in a turbid liquid medium. The substrate for removal is Methylene blue, a compound used frequently in TiO_2 photocatalysis [19], and the turbidity of grey water is simulated using a physical shield over the reactor, as seen in a picture of the prototypes (fig. 3.2, below). The set of experiments seeks to imitate the in situ conditions for the reactor as much as possible, using a solar simulator and recirculation of the substrate, in order to examine the effectiveness of cylindrical waveguides for channeling UV light to reactive surfaces in a grey water medium.

II. System details:

The CORE reactor is a thin panel with a staggered arrangement of waveguide cylinders in cross flow. The system is designed for recirculation, as multiple passes over the solar active photocatalyst is necessary for substantial treatment of grey water. Convection increases transport to the surface of the cylinders, where the hydroxyl radicals are formed. Cross-flow over the photocatalytically active cylinder bank is pump forced.

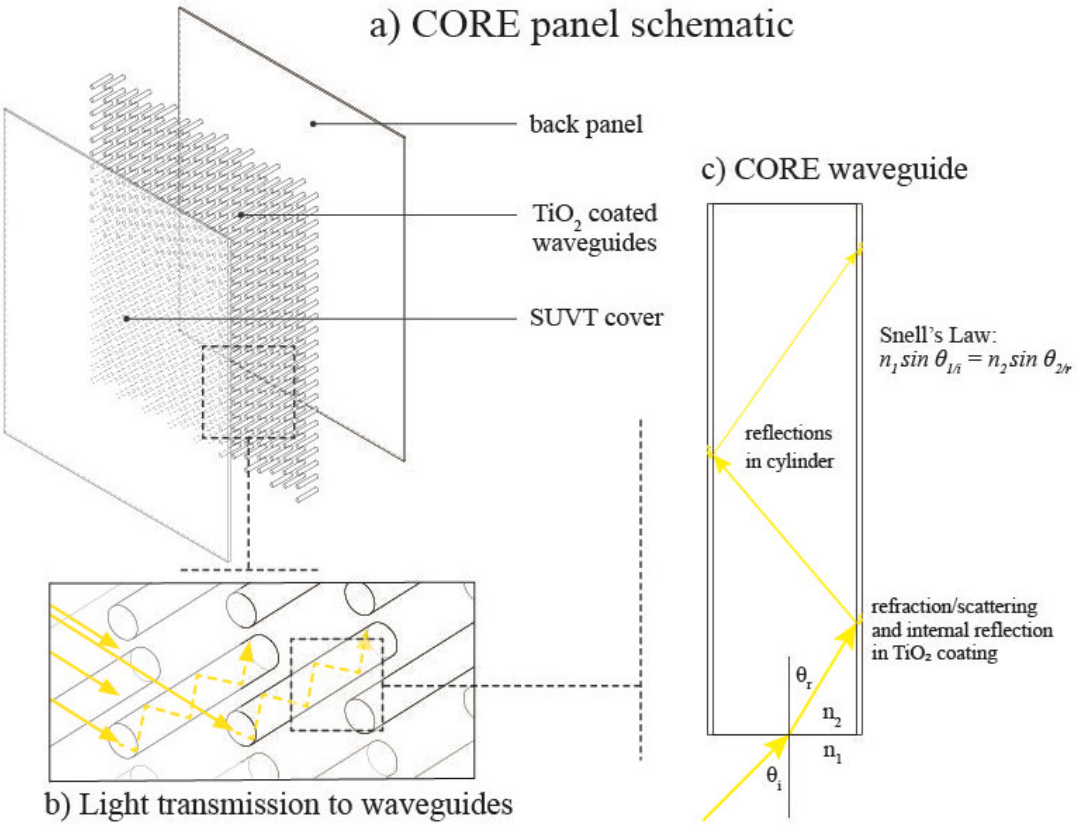

Figure 3.1: a) Schematic of CORE Reactor, b) light transmission to waveguides and c) UV transmission through waveguides

Because the primary limiting factor in using photocatalysis to clean greywater is light transmission in a turbid media, the experiments detailed in this study are designed to determine the reaction rate potential of the optical elements in a fully obscuring substrate. To investigate the efficacy of waveguides in an absorbing medium, we compared removal results from an 'open-faced' reactor to a reactor with all but the cylinder ends exposed (the covered or 'grated' reactor, figure 3.2) in order to determine how much removal is due to the activation of the catalyst from the interior of the cylinder. As grey water is only broadly defined, we use a probe compound, methylene blue (MB), which has well-established kinetics and reaction mechanisms. [20] Flow rate was varied in the moderate laminar regime between 100 – 350 Re and surface reaction kinetic potential determined for both shielded and unshielded reactors. Additional control tests were run for a reactor with no cylinders, with blank (uncoated) cylinders, a grated reactor with blank cylinders, tests run in ambient light, and foil covered reactors. A second set of tests compared removal in grated reactors only, with reduced molar concentration of MB and varied flow rate.

Figure 3.2: 'Grated' and 'open-faced' CORE Reactor lab prototypes

III. Methods and Materials:

3.1 Materials and Analytical Methods

The TiO_2 used is Degussa p-25 (Evonik), immobilized to custom borosilicate glass cylinders (Pegasus Glass, Ontario) of 1.5 mm diameter based on a thin sol-gel process. [21] The cylinders were examined with a scanning electron microscope to verify coating thickness and integrity. Slides were prepared using this method to test the transmission characteristics of the coating and were found to transmit UV light through to the catalyst.

The CORE reactor was built on site at UC Berkeley. The body was milled out of aluminum with an interior volume of 54 mL (including cylinders, 56 mL w/o). Polished and coated high transmittance glass rods**,** 3mm diameter and 15 mm length, were placed in a regular staggered arrangement of 6 x 8 rows (described above). The interior was covered with a 1/8" thick high transmittance acrylic plate (Solacryl SUVT, National City) and sealed around the edges. The covers used in the covered trials are 1.5 mm thick laser-cut pinewood. The covers were offset from the cylinders in order to account for both shading and refraction in order to ensure light passing through the holes reached the heads of the cylinders directly.

The solar simulator (Atlas Sunset XLS+) produces light with the spectrum and intensity of solar light at the surface of the earth at a maximum setting of 750W/m^2. The decoloration of Methylene Blue was measured with a spectrophotometer at 665 nm to assess its removal.

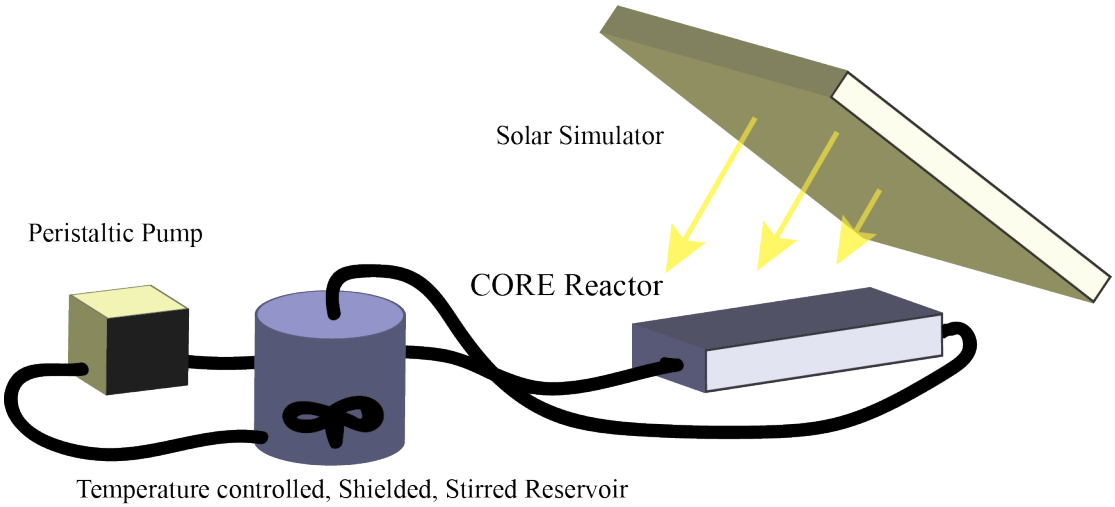

Figure 3.3: Experimental Diagram

3.2 Experimental Set up

Figure 3.3 above shows the experimental set up as a whole. The experiment was run in batch mode; the recirculating system employed a 500 mL beaker as a reservoir to contain the 200mL initial 20 μmol/L concentration batch, covered with light shielding to prevent photolysis, mixed by a magnetic stirrer. A peristaltic pump moved the fluid through 1 m length of neoprene tubing from the reservoir to the reactor and back. The reservoir was immersed in a temperature controlled water bath (19°C) to prevent rate acceleration due to thermal gain.

The experiments were run for a 30-minute dark period in order to account for initial adsorption to the cylinders, and then the solar simulator was turned on for a period of 180 minutes. The light source was maintained at a constant 45 degree angle to the reactor face at an intensity of 750 W/m^2, meaning that the incident intensity on the cylinders was approximately 300 W/m^2 after accounting for angle of incidence, absorption in the acrylic cover, and reflectivity. Samples were taken at 30-minute intervals.

IV. Modeling:

4.1: Fluid modeling

Tube bank momentum and heat transfer have been explored primarily for heat exchangers. Seminal experimental studies for the cross flow over tube bank heat exchangers have been completed by Žukauskas [22], and Beale [23], [24] collated

these studies for numerical analysis. The tube bank configuration was chosen for the same reason it is used in heat exchangers: staggered tube banks provide a high surface area and the flow pattern over them increases mixing and thus assists in over coming mass transfer resistance. The configuration we chose is a unit-staggered array of cylinders due to its higher transfer performance in laminar flows, meaning that the spacing between cylinders is equal to their diameter in an equilateral triangle arrangement. An image of the basic staggered geometry is presented in figure 3.4:

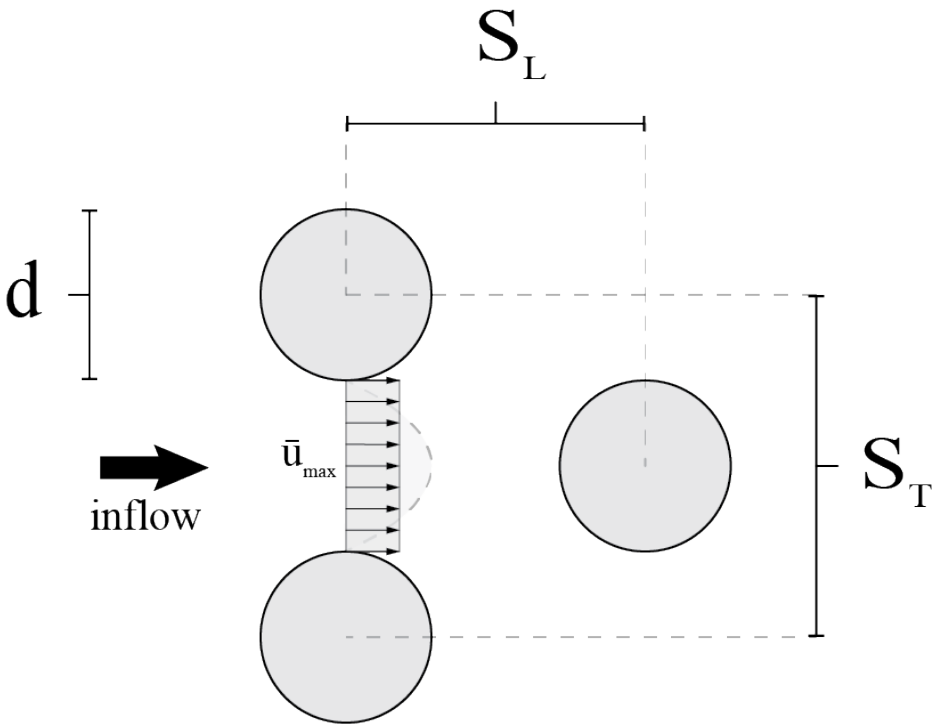

Figure 3.4: Staggered cylinder geometry and variables of interest

For fluid flow over a single cylinder the lack of physical constraints leads to the development of vortex shedding at relatively low Reynolds numbers (~50-80), leading to transitional flow regime where unsteady vortex shedding occurs. In cross flow over staggered cylinder arrays, the adverse pressure gradient experiences a constraint due to the presence of other nearby cylinders. The resulting flow field remains constant for steady inflow up to much greater flow rates, remaining laminar (pre-transitional regime, non-turbulent eddy forming) with regular vortices forming behind the cylinders up to Re < 500-1000. [22] From figure 3.4:

$$Re = \frac{\rho \bar{U}_{max} d}{\mu} \tag{1}$$

and $U_{max,avg}$ by:

$$\overline{U}_{max} = U_{avg} * \left[\frac{S_T}{S_T - d}\right] \quad (2)$$

4.2 Reaction kinetics

In this experiment the surface reaction rate of the photoactivated TiO_2 coated cylinders due to UV light from the interior of the cylinder is desired in order to assess waveguide performance in a turbid medium. Žukauskas obtained a correlation for heat transfer for cylinders in tube banks, which can be transformed using analogies for mass transfer. For the transfer of MB across the boundary layer to a single cylinder surface, one can use the expression for staggered cylinders in laminar flow (100<*Re*<1000):

$$k_{bl} = c\frac{D_{MB}}{d} Re^{0.5} Sc^{0.36} \quad (3)$$

where *c* is a constant reported between 1.04 and 0.71 for the moderate laminar range [22], [25], k_{bl} is the kinetic constant of the MB to the surface of the cylinder, D_{MB} is the diffusion coefficient of methylene blue, *Sc* is the Schmidt number, and *d* is the diameter of the cylinder.

4.3 Optical Analysis

To further define what the active surface area is for each cylinder we require the use of optics. In the previously referenced waveguide PC technologies the waveguide was a fiber optic cable, whereas we use high transmittance glass. In this case geometrical optics, explored with the use of Snell's law and the Fresnel equations, show a different result from the previous studies. In this case the light refracting and reflecting in the cylinder interior will be highly absorbed into the TiO_2 at each reflection (where it will be internally reflected, and thus contained entirely within the PC coating), limiting the distribution of the UV light in the whole.

An idealized model of attenuation of the light down the cylinder due to internal reflection in the TiO_2 is derived using attenuated flux:

$$I_{TiO_2}(z) = -\frac{dI_g}{dz}\frac{d}{4} \quad (4)$$

Integrating this over the length of the high transmittance glass gives the light in the cylinder as:

$$I_{cyl} = I_o e^{-\alpha_{eff} z} \quad (5)$$

where α_{eff} is the effective attenuation coefficient of light lost to the coating and *z* is the cylinder axis. All other UV light energy is assumed to be internally reflected in the TiO_2 coating .

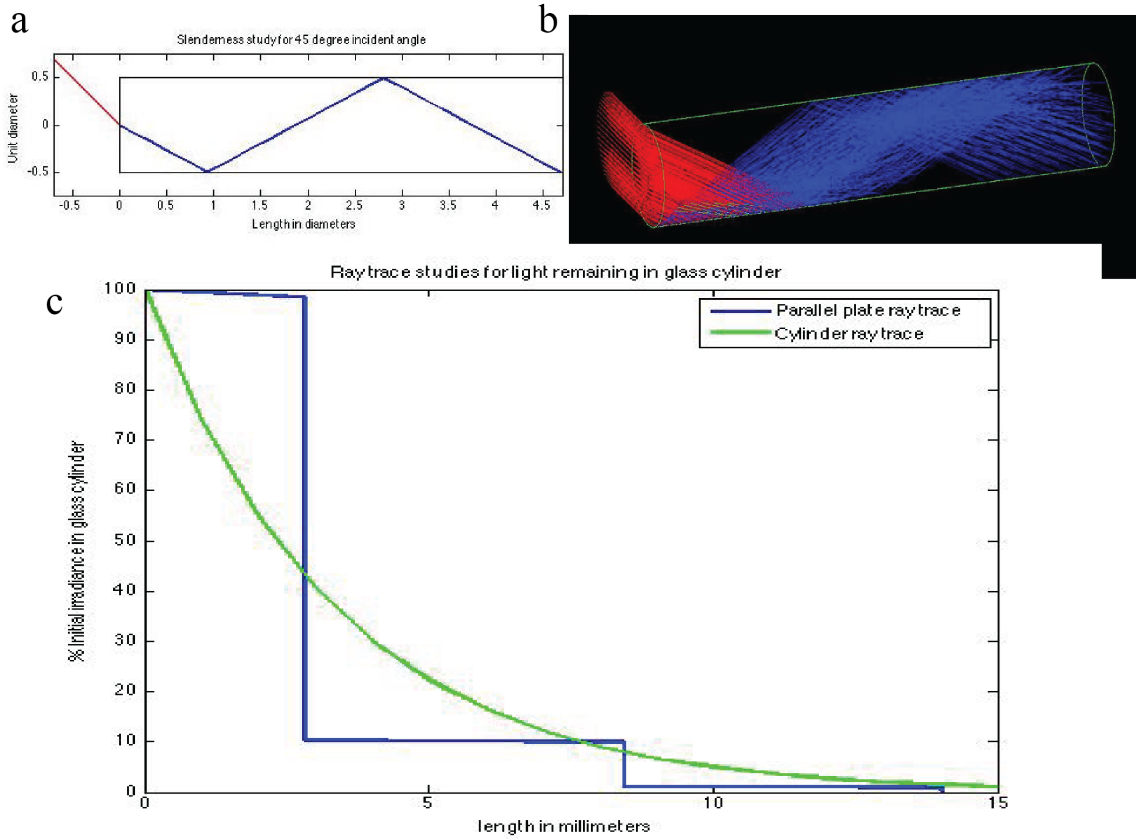

Figure 3.5: a&b) Ray trace models, c) percent UV light remaining in cylinder (reflections vs. idealized model)

However, an optical analysis of the cylinders demonstrates that 99% of UV energy is absorbed in the walls after the second reflection (figure 3.5c). The light comprising this first reflection is the volumetric form of an elliptical wedge with base of the cylinder head. The projection of that light onto the cylindrical wall is in the form of a lateral cylindrical hoof (the red traces in figure 3.5b). Unwrapping the cylinder we find that the wall of the cylindrical hoof is a sinusoidal area, with its amplitude related directly to the incident angle of the incoming light and its half period to the radius of the cylinder.

The simple geometry of the illuminated surface area for the first reflection is given by:

$$S_{ill} = 2r^2/cotan(\theta_t) \tag{6}$$

where θ_t is the angle of transmission into the glass, measured from the surface of the waveguide. The great majority of the photocatalytic reaction occurs in the

illuminated area of the cylinder, comprised of the first and second reflection, that is, the hoof area and its double.

In the reactors that we constructed, there are series of 9 half cylinders for each area in flow, meaning that the reaction equation for influx will take place over 4.5 cylinders. From equation 6 the area of the light refracted into the TiO_2 at the first reflection is 6% of the total surface area. Applying then the total active area to equation 3, we find the expected kinetics for a flow through the reactor:

$$k_r = 0.18c * n_{cyl} \frac{D_{MB}}{d} Re^{0.5} Sc^{0.36} \quad (7)$$

where k_r is the surface kinetic constant over one flow through and n_{cyl} is the number of cylinders in each flow through influx area.

Treating the reservoir in the system as an isothermal stirred tank recirculating batch reactor, the mass balance for the outflow is given by the equation:

$$\frac{C(t)}{C_o} = e^{(\phi-1)\frac{t}{\tau}} \quad (8)$$

where ϕ is the fraction remaining after one flow through, t is time, and τ is the HRT in the reservoir. Removal over one flow through is found by correlation (eq.7), and the kinetic rate determined and compared to experimental results to attempt to determine the transfer dynamics inside the reactor.

4.4 Photocatalytic reaction rates

Photocatalytic reactions, the mineralization of organic compounds with O_2 on an active photocatalyst surface, are assumed to follow Langmuir-Hinschelwood kinetics: [26]

$$R = -\frac{dC_o}{dt} = \frac{k_1 K C_o}{1+KC} \quad (9)$$

Here R is the removal rate of the contaminant, C_o is the initial concentration, K is the Langmuir adsorption constant of the contaminant onto the photocatalytic surface, and k_1 describes the reactivity of the overall photocatalytic reaction pathway from the UV photoactivated TiO_2, O_2, and hydroxyl radicals in substrate removal. The reactivity is dependent on light intensity and the amount of O_2 available for reactions. For low concentrations of contaminants (reactions not limited by O_2 availability) the reaction is considered pseudo-first order. [27]

$$R_1 = k_{app,V} C_o \quad (10)$$

where $k_{app,V}$ is the pseudo-first order apparent volumetric reaction rate constant. The pseudo-first order reaction rate constant is comprised of both reactivity and adsorption constants.

However, photocatalytic reaction kinetics are subject to a number of factors, and several kinetic regimes have been observed in the literature. [28] Factors such as pH, substrate concentration, active surface area, and light intensity all play a part in influencing removal kinetics. Pseudo-zero order kinetics are regularly seen for factors related to diffusive and reaction limitations, as well as high relative concentration substrates:

$$R_0 = k_{app,V} \tag{11}$$

These models approximate the removal in the bulk of the fluid, and because the removal in this system is considered a surface reaction due to the time scale of hydroxyl production and disappearance, the conversion of bulk to surface reaction is given by:

$$k_{app,S} = \frac{V_r}{S_r} k_{app,V} \tag{12}$$

where S_r is the illuminated reactive surface area in the reactor. The surface reaction rate can be determined once the apparent volumetric reaction rate is known.

With the reaction rate the efficiency of the reactor can be assessed by the over all UV quantum yield:

$$\theta_{UV} = \frac{k_{app,surf}}{incident\ UV\ intensity} \tag{13}$$

V. Results:

5.1 First Set of Experiments: All Reactor Types

In the initial tests comparing all reactor types, the effect of varying flow rate showed no difference in the results, and all trials for each reactor type showed a variation of ~1% at all data points. All reactors studied showed (pseudo) zero order kinetics over the three hour illuminated time period (fig. 3.6). Control tests using foil covered and ambient light tests showed <1% removal, and so the solar simulator is without question the driving force behind the removal in all trials. The volume and surface kinetic rate constants are shown in table 3.1, in μM/dm.

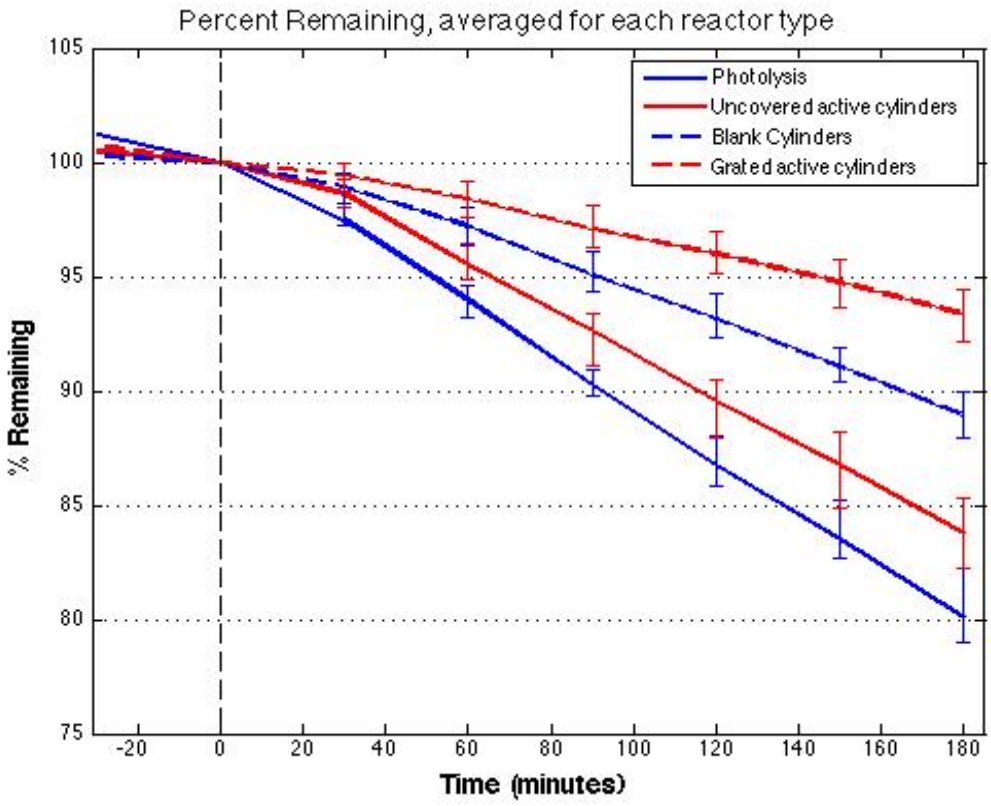

Figure 3.6: Remaining dye vs. time in reactors by type. Photolytic reactors in blue, Photocatalytic reactors in red

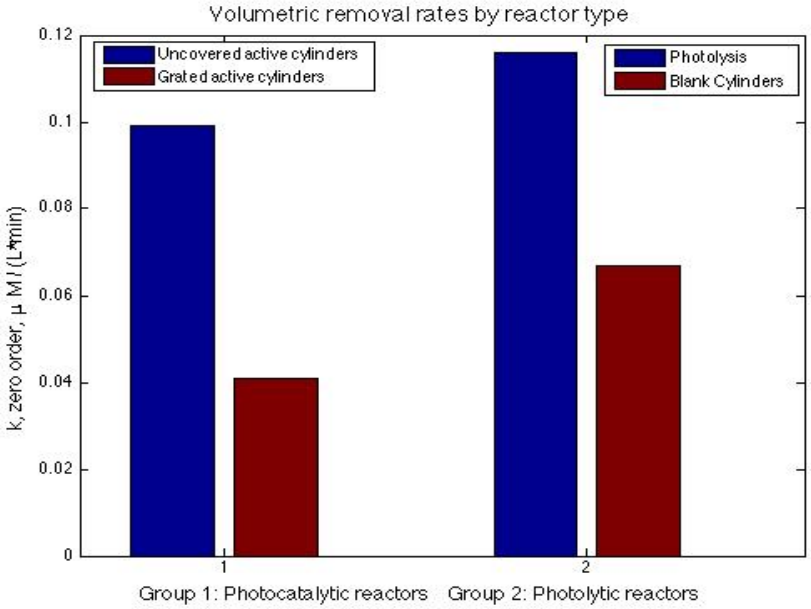

Figure 3.7: Rates of removal for different reactor types

Table 3.1: kinetic rate constants per reactor, volume and surface

	Uncovered coated cylinders	Grated coated cylinders	No cylinders, no coating	Cylinders, no coating
$k_{,V,app}$(μM/dm*s)	0.00099	0.00035	0.00116 (N/A)	0.00067 (N/A)
$k_{,S,app}$ (μM/dm*s)	0.00012	0.000045	N/A	N/A

What stands out about the first set of results is that the non-cylinder, photolytic reactor shows the best removal over the test period. While this is interesting, it is not especially surprising: solar irradiance carries all wavelengths of light including the wavelengths that MB absorb highly [29], and there are clearly reaction limitations for the coated surfaces in this reactor prototype. Comparing this to the blank cylinder data, it is clear that the cylinders are actually producing an inhibitory effect on light transmission from the surface into the bulk of the fluid, "shielding" over 40% of the photolytic effect.

Despite the strong effect of photolysis, the uncovered-coated cylinders show better removal than the blank cylinders, demonstrating that photocatalytic excitation is causing accelerated removal in the cylinder banks. Most importantly, the cylinder heads alone in the covered trial produce measurable removal. A control test using blank cylinders and the covering grate showed <1% removal.

Optics studies show that in the bulk of the medium, light entering the cylinder long axis surface will continue into the cylinder at refracted angle of approximately 62 degrees. This means that light incident on the long surface of the cylinders below the height of 6 mm (or below 60% of the cylinder length) will be directed into the base of the cylinder, accounting for a significant amount of light loss from the medium in the area of the serried cylinders.

The uncovered-coated reactor has a combination of photolytic and photocatalytic response, as well as the shading effect. Because the blank cylinder reactor shows 33% less removal than the coated cylinders, photocatalytic excitation in the uncovered-coated reactor is producing removal, as the covered cylinder trials would lead us to believe. However, the comparatively large effect of the removal due to the cylinder heads alone, the covered test accounting for 40% of the removal compared to the uncovered coated cylinder reactor. This demonstrates that the large majority (over 90%) of catalytic response in the uncovered coated reactor is due to the light entering the heads of the cylinders themselves, and is not due to light incident on cylinder surfaces from within the medium.

5.2 Second Set of Trials: Grated Reactors at Low Concentration

The first set of trials all show (pseudo) zero order response, regardless of flow rate. It is unclear what the reaction limitations are in these trials; they could be due to

photonic, diffusive, or surface saturation limitations. The first set of trials also demonstrate that the PC reaction due to light passing purely through the cylinder heads is evident, but constrained. A second set of trials was held on the grated reactors alone with a reduced initial concentration (6μM/dm) in order to examine the possible origin of the limitations seen in the first set of trials.

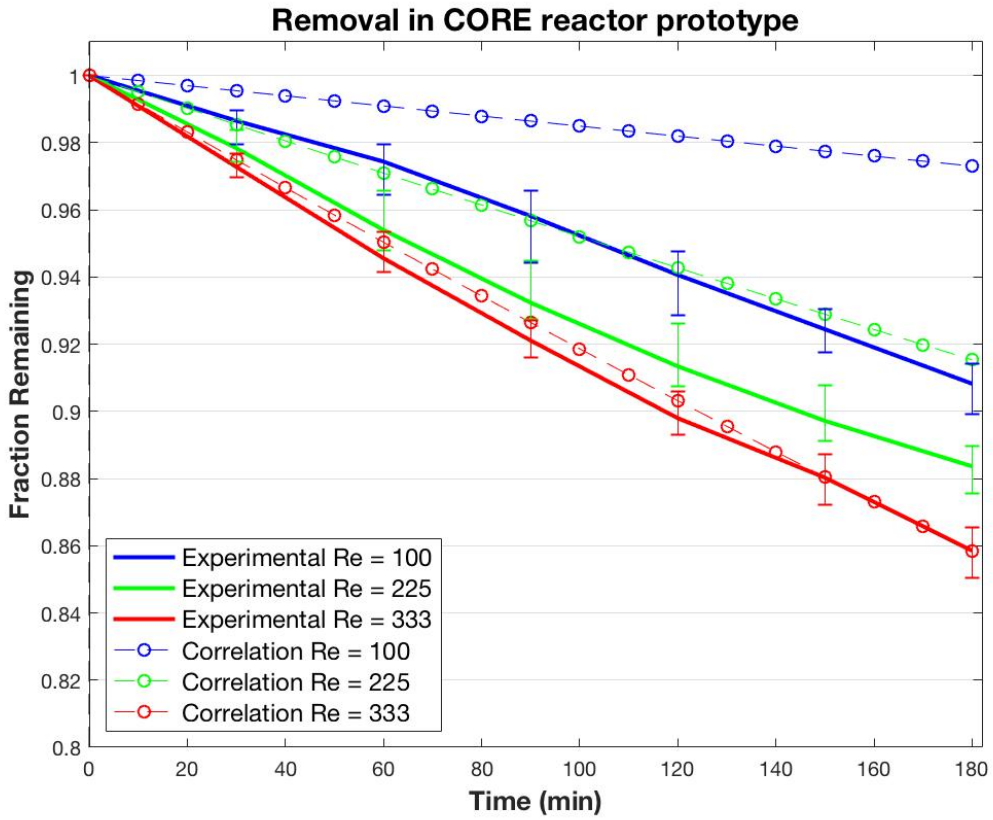

Figure 3.8: Comparison plot of expected removal (dashed) to actual (solid) in low concentration tests

In the lower concentration tests we see variation by flow rate, meaning that this is at most a partially diffusion limited regime, even though the results still show pseudo-zero order kinetics. The expected values from the Žukauskas analogy, which are sensitive to small changes, are close to within the range of error of the results, particularly for the moderate laminar flow range of interest. It is suspected that the of the correlation model is due the omission of the adsorption constant '*K*' in Eq 9. Overall the correlation model performs well when compared with the experimental results for this slow reaction. It is possible to use this model with slight corrections for further simulation studies.

In table 3.2 the surface kinetic constants from eq. 7 are compared to the pseudo-zero order rates in the bulk from the experimental results:

Table 3.2: Volumetric and surface kinetic rates from experiment and analogy

	Re100	Re225	Re333	Photonic Efficiency
k_V exp (*10^{-4})	5.1	6.6	7.8	~0.1%
k_S exp (*10^{-4})	0.65	0.84	0.99	~0.01%
k_S ana (*10^{-4})	0.34	0.48	0.57	~0.01%

The analogy for mass transfer to the cylinder surfaces from the bulk shows good comparison to the experimental results. Discrepancies are expected from the complex kinetics for the mediated reaction rate, which involves generation of radicals and surface site adsorption.

VI. Analysis:

6.1 Optics

The cylindrical waveguides in the CORE reactor are effective for delivering UV light into a turbid medium, as evidenced by the removal produced with the grated reactor. Due to the comparison of the empty, blank cylinder and coated cylinder reactors, we can deduce that the majority of the photocatalytic removal is due to the light passing into the cylinder heads transmitting to the cylinder surfaces from within. Optical analysis allows us to derive the true active surface area for the cylinders, and predict active surface area for any incident angle. The reactors in both sets of trials show reaction limitations, the origins of which must be considered.

6.2 Reaction limitations

The expected reaction kinetics for photocatalytic response is (pseudo-) first order. In this experiment we see pseudo-zero order reaction rates and need to consider where limitations originate. Typical photocatalytic limitations are light intensity, surface saturation/contaminant concentration, diffusive transport, photonic limitations, and pH. [28], [30]

Regarding light limitations, the photocatalytic reaction is linearly proportional with UV intensity up to 250 W/m^2 and then is proportional to the square root of the radiant flux. [31] The intensities at which the non-linear relation occurs are far greater than used in the CORE experiment, which used a solar simulator with full spectrum maximum intensity of 750 W/m^2 (~30 W/m^2 UV intensity) . Solar photocatalysis in general never goes beyond this linear limit, and so we expect the reaction rate to vary linearly with intensity in this range. Other factors that can be ruled out are the pH (7.0), as it is within the range for which MB and TiO_2 avoid surface charge effects. Finally, the temperature was controlled to within 5C, so

acceleration effects due to heating can be ruled out, though are expected to be significant in outdoor trials.

Though not evident in the first set of results, the flow rate was varied from Re100 to Re350, all laminar for this reactor configuration. Variation of the Reynolds number within this range means the boundary layer around the cylinders will decrease in thickness by half, reducing diffusional constraints:

$$t_{bl} \propto Re^{-1/2} \tag{14}$$

Due to the lack of variation in reaction due to variation in flow rate for the higher concentration trials (thus independent of the boundary layer), it can be assumed the main factors in the kinetic limitations in this experiment was the initial contaminant concentration (20 μM) and lack of reacting surface area. At this concentration the limited reacting surface area shown in the above reflection analysis (figure 5), reached saturation and was potentially photon limited.

The second set of trials run with reduced concentration of MB show variation with flow rate, and thus the transfer across the boundary layer is not controlling the reaction rate. Owing to the correspondence between the experimental results and the analytical expectations, the zero order kinetics here are more likely evidence of a slow reaction rather than a specifically limited one. [32]

VI. Conclusion:

A model compound methylene blue was investigated for photocatalytic degradation with the use of a novel reactor type using catalyst-coated waveguides to draw UV light into the interior of the medium. Specifically, the effects of the waveguides alone were studied in order to assess the effectiveness of the reactor for contaminant removal in turbid fluids. It was demonstrated that the primary source of photocatalytic response in the system was due to light entering the heads of the cylinders, and the effective kinetic surface rates and quantum efficiency compare well with other reactor types.

Optical analysis of the resulting surface kinetics show that the Pseudo-zero order kinetic rate is due to surface saturation for concentrations above 5μM/dm. At concentrations below this there is good agreement with expected removal rates based on modeling with heat transfer analogy correlations. While removal due to light entering the cylinder heads was shown to be the primary source of photocatalytic response in the system, geometrical optimization is necessary to ensure greater removal in future prototypes. The CORE reactor in its current configuration shows insufficient removal to be used for grey water remediation, yet the premise of using waveguides to draw light into the interior of a turbid medium shows promise for further study.

References:

[1] K. Hashimoto, H. Irie, and A. Fujishima, "TiO 2 Photocatalysis : A Historical Overview and Future Prospects," vol. 44, no. 12, pp. 8269–8285, 2005.

[2] J. H. Carey, J. Lawrence, and H. M. Tosine, "Photodechlorination of PCB's in the presence of titanium dioxide in aqueous suspensions," *Bull. Environ. Contam. Toxicol.*, vol. 16, no. 6, pp. 697–701, 1976.

[3] H. Choi, S. Al-Abed, and D. Dionysiou, "TiO2-Based Advanced Oxidation Nanotechnoliges for Water Purification and Reuse," in *Sustainability, Science, and Engineering*, Elsevier B.V., 2010, p. 416.

[4] H. Lin and K. T. Valsaraj, "An optical fiber monolith reactor for photocatalytic wastewater treatment," *AIChE J.*, vol. 52, no. 6, pp. 2271–2280, 2006.

[5] T. Van Gerven, G. Mul, J. Moulijn, and A. Stankiewicz, "A review of intensification of photocatalytic processes," *Chem. Eng. Process.*, vol. 46, pp. 781–789, 2007.

[6] I. Boiarkina, S. Norris, and D. Alec, "The case for the photocatalytic spinning disc reactor as a process intensification technology : Comparison to an annular reactor for the degradation of methylene blue," *Chem. Eng. J.*, vol. 225, pp. 752–765, 2013.

[7] C. Sordo, R. Van Grieken, J. Marugán, and P. Fernández-Ibáñez, "Solar photocatalytic disinfection with immobilised TiO2at pilot-plant scale," *Water Sci. Technol.*, vol. 61, no. 2, pp. 507–512, 2010.

[8] S. Malato, P. Fernández-Ibáñez, M. I. Maldonado, J. Blanco, and W. Gernjak, "Decontamination and disinfection of water by solar photocatalysis: Recent overview and trends," *Catal. Today*, vol. 147, no. 1, pp. 1–59, 2009.

[9] F. Denny, E. Permana, J. Scott, and J. Wang, "Integrated Photocatlytic Filtration Array for Indoor Air Quality Control," *Environ. Sci. Technol.*, vol. 44, no. 14, pp. 5558–5563, 2010.

[10] A. Silverman, "Sunlight Inactivation of Waterborne Viruses: Mechanisms, Modeling, and Application to Surface Waters and Wastewater Treatment," UC Berkeley, 2013.

[11] B. Dawney and J. M. Pearce, "Optimizing the solar water disinfection (SODIS) method by decreasing turbidity with NaCl," *J. Water, Sanit. Hyg. Dev.*, vol. 2, no. 2, pp. 87–94, 2012.

[12] V. Rao, "Heating and Treating Water with Sunlight: Solar Photocatalytic-Thermal Systems for a Sustainable Built Environment," UC Berkeley, 2018.

[13] K. Hofstadler and S. Novalic, "New Reactor Design for Photocatalytic Wastewater Treatment with Ti02 Immobilized on Fused-Silica Glass Fibers: Photomineralization of 4-Chlorophenol," *Environ. Sci. Technol.*, vol. 28, no. 4, pp. 670–674, 1994.

[14] N. J. Peill and M. R. Hoffmann, "Development and Optimization of a TiO2-Coated Fiber-Optic Cable Reactor: Photocatalytic Degradation of 4-Chlorophenol," *Environ. Sci. Technol.*, vol. 29, no. 12, pp. 2974–2981, 1995.

[15] N. J. Peill and M. R. Hoffmann, "Chemical and physical characterization of a TiO2-coated fiber optic cable reactor," *Environ. Sci. Technol.*, vol. 30, no. 9, pp. 2806–2812, 1996.

[16] N. J. Peill and M. R. Hoffmann, “Fiber-Optic Cable Reactor for Waste Stream Remediation,” *J. Sol. Eneergy Eng.*, vol. 119, no. August, pp. 229–236, 1997.
[17] W. Choi, J. Y. Ko, H. Park, and J. S. Chung, “Investigation on TiO 2 -coated optical fibers for gas-phase photocatalytic oxidation of acetone,” vol. 31, pp. 209–220, 2001.
[18] W. Wang and Y. Ku, “The light transmission and distribution in an optical fiber coated with TiO2 particles,” *Chemosphere*, vol. 50, no. 8, pp. 999–1006, 2003.
[19] L. Rizzo, J. Koch, V. Belgiorno, and M. A. Anderson, “Removal of methylene blue in a photocatalytic reactor using polymethylmethacrylate supported TiO2 nanofilm,” *Desalination*, vol. 211, no. 1–3, pp. 1–9, 2007.
[20] H. Gnaser, M. R. Savina, W. F. Calaway, C. E. Tripa, I. V. Veryovkin, and M. J. Pellin, “Photocatalytic degradation of methylene blue on nanocrystalline TiO 2: Surface mass spectrometry of reaction intermediates,” *Int. J. Mass Spectrom.*, vol. 245, no. 1–3, pp. 61–67, 2005.
[21] E. Haimi, H. Lipsonen, J. Larismaa, M. Kapulainen, J. Krzak-Ros, and S. P. Hannula, “Optical and structural properties of nanocrystalline anatase (TiO 2) thin films prepared by non-aqueous sol-gel dip-coating,” *Thin Solid Films*, vol. 519, no. 18, pp. 5882–5886, 2011.
[22] A. Žukauskas, “Heat Transfer from Tubes in Crossflow,” *Adv. Heat Transf.*, vol. 18, pp. 87–159, 1987.
[23] S. B. Beale and D. B. Spalding, “NUMERICAL STUDY OF FLUID FLOW AND HEAT TRANSFER IN TUBE BANKS WITH STREAM-WISE PERIODIC BOUNDARY CONDITIONS,” *Trans. Can. Mech. Eng. Soc.*, vol. 22, no. 4A, pp. 397–416, 1998.
[24] S. B. Beale and S. B. Spalding, “A Numerical Study of Unsteady flow in In-Line and Staggered Tube Banks,” *J. Fluids Struct.*, vol. 13, pp. 723–754, 1999.
[25] I. Martinez, “Isidoro Martínez’ lectures on Heat and Mass Transfer,” 2015. [Online]. Available: http://webserver.dmt.upm.es/~isidoro/bk3/c11/Isidoro Mart%EDnez’ lectures on Heat and Mass Transfer.pdf.
[26] C. Turchi and D. F. Ollis, “Photocatalytic Degradation of Organic Water Contaminants: Mechanisms Involving Hydroxyl Radical Attack,” *J. Catal.*, vol. 122, no. 1, pp. 178–192, 1990.
[27] D. F. Ollis, “Kinetics of Liquid Phase Photocatalyzed Reactions : An Illuminating Approach †,” *J. Phys. Chem B*, vol. 109, pp. 2439–2444, 2005.
[28] K. Mehrotra, G. S. Yablonsky, and A. K. Ray, “ Kinetic Studies of Photocatalytic Degradation in a TiO 2 Slurry System: Distinguishing Working Regimes and Determining Rate Dependences ,” *Ind. Eng. Chem. Res.*, vol. 42, no. 11, pp. 2273–2281, 2003.
[29] J. Tschirch, R. Dillert, D. Bahnemann, B. Proft, A. Biedermann, and B. Goer, “Photodegradation of methylene blue in water, a standard method to determine the activity of photocatalytic coatings?,” *Res. Chem. Intermed.*, vol. 34, no. 4, pp. 381–392, 2008.
[30] J. Theurich, M. Lindner, and D. W. Bahnemann, “Photocatalytic Degradation of 4-Chlorophenol in Aerated Aqueous Titanium Dioxide Suspensions: A Kinetic and Mechanistic Study,” *Langmuir*, vol. 12, no. 26, pp. 6368–6376, 1996.
[31] J. M. Herrmann, “Heterogeneous photocatalysis: State of the art and present

applications," *Top. Catal.*, vol. 34, no. 1–4, pp. 49–65, 2005.
[32] L. Pogliani, "Pseudo-zero-order reactions," *React. Kinet. Catal. Lett.*, vol. 93, no. 2, pp. 187–191, 2008.

Chapter IV:
Performance Evaluation of Building Integrated Hybrid Photocatalytic/Thermal Systems

I. Introduction:

Building integrated solar technologies for energy gain and climate conditioning are now regularly used in the built environment, particularly in newer constructions. Of these photo-voltaic (PV) and thermal (T) gain panels are the most well known and studied, however grey water remediation for onsite reuse is another promising application for solar technologies that is currently gaining popularity, particularly in water scarce regions. [1] Particularly effective for fluid cleaning is the use of UV activated photocatalytic (PC) nano-materials (TiO_2, for example) as a surface or slurry treatment. [2], [3] While hybrid systems for energy collection and thermal gain have been studied extensively [4] owing to the synergistic effects of the physics for their function, recent studies in heterogeneous catalysis suggest that a similar mechanism may exist for thermal gain and photocatalytic action. [5] The authors have researched and developed a panel that hopes to achieve both thermal gain for building climate conditioning and photocatalytic (PC) grey water remediation for on-site recycling (PC-T) and promote its possibilities as a building integrated technology.

Though heat gain and photocatalytic efficiency may have synergistic effects, combining those into a useful hybrid system remains a challenge. Both technologies desire surface area normal to incident radiation to maximize their effects. The CORE recirculating panel (Cylindrical Optical Reactive Elements, a novel technology described in section II) seeks to bridge both of these requirements in its design, includes radiation-absorbing surfaces orthogonal to each other and thus the attitude of the panel presented to the solar source is critical to its efficient multi-physical functioning. Design parameter selection also includes optical element sizing, panel/reservoir area/volume, flow rate, material options, and number of covers for solar facing insulation amongst others. These parameters can bring the dual goals of the technology into conflict with each other in terms of maximizing their individual efficiency and daily output.

The amount of optical waveguide available surface area, the site of the removal of contaminants, directly conflicts with the amount of energy absorbed by the back thermal absorber plate, and thus the thermal gain of the system: the two physics compete for energy absorption as the driver of their respective processes. Additional glazing covers that retain more heat will decrease the amount of UV light available for photocatalytic conversion. The tilt of the panel also causes the individual physics to geometrically compete for maximal efficiency. This study examines those trade offs as a whole, while finding parameter configurations that can be applied as solutions to specific site requirements in practical construction.

Many studies have reported on the potential of photocatalysts to disinfect and mineralize contaminants in the environment. [6] There is within this broad body of literature a set of investigations that concern process intensification for the remediation of liquids using fixed titania substrates. [7] Detailed reviews have also been carried out on the system types and their effectiveness. [8], [9] Photocatalyst coated waveguides have been used for process intensification, as available surface area is a limitation for immobilized photocatalyst. [10], [11] The only study that has focused on optimization of these systems is the work of Choi, where the optimal depth of the catalyst layer on a light transmitting fiber was determined for removal efficiency. [12]

Thermal gain panels have been much more widely studied, beginning with the work of Hottel in 1942. [13] These systems have been analytically optimized for efficiency since the solar model of Hottel and Willier. [14], [15] Hybrid systems such as PV-T were proposed and studied as the synergistic effects of photovoltaic electrical gain requiring lower temperatures for higher efficiency) and thermal gain (removing heat from the panel). [16] Reviews of these systems have been carried out and published. [17] Hybrid photocatalytic systems remain absent from current engineering research.

The optimization of the PV-T hybrid systems takes into account a wide array of possibilities for the system, such as multiple covers, flow rate, collector vs. flat plate and pipe models, the number of cells and their length, and material selection. [18], [19] Papers describing the simultaneous optimization of these multiple decisions variables analyze PV-T systems for efficiency and economic performance. [20], [21] For the CORE system, an initial metaheuristic survey needs to account for the possibility of a free standing/roof top system vs. wall panels for building integration, as well as geometric properties such as the packing density of the waveguides and the depth of the panel and reservoir. The motivation of this research is to apply multi-objective optimization algorithms to the PC-T panel in order to better understand what the key parameters are, and under what conditions the system will best perform. These key questions are what this study seeks to answer.

The PC-T panel studied using the single procedure for estimating design variables is a recirculating system with a reservoir. The removal model is derived from experiments performed on a prototype scaled to the proposed building integrated system. The thermal model applied finds performance coefficients iteratively and then is adapted for use in the elitist multi-objective evolutionary algorithm NSGA-II. NSGA_II is preferred as the method of multi-objective optimization in this study because it preserves spacing in the solution space.

Using guidance of previous work in hybrid solar systems, the feasibility of the novel CORE system is investigated in this research. Developing a model and applying optimization over the primary chosen design variables permits rapid exploration of its possibilities in application. Whereas the extensive previous studies in PV/T systems allow for highly specific tuning of a well-characterized system, this research

is focused on examining the feasibility of the CORE panel at the pilot scale to investigate parameter relations to performance and suggest site based modifications to façade design. The motivation of this work is that these design parameters can be simultaneously explored in a single run of the Multi Objective Optimization procedure, and that the results define the range of potential uses for the hybrid photocatalytic/thermal gain panel type.

II. System details:

The CORE reactor is a panel system with a staggered arrangement of waveguide cylinders in cross flow (see chapter III for more details). The goal of the technology is to provide disinfected water for reuse on site in the built environment, as well as to produce heat for use in building climate controls. The system is designed for recirculation, as multiple passes over the solar active photocatalyst are necessary for substantial treatment of grey water. Convection increases transport to the surface of the cylinders, where the hydroxyl radicals are formed due to photocatalyst activation. Cross flow over the cylinder bank is pump forced.

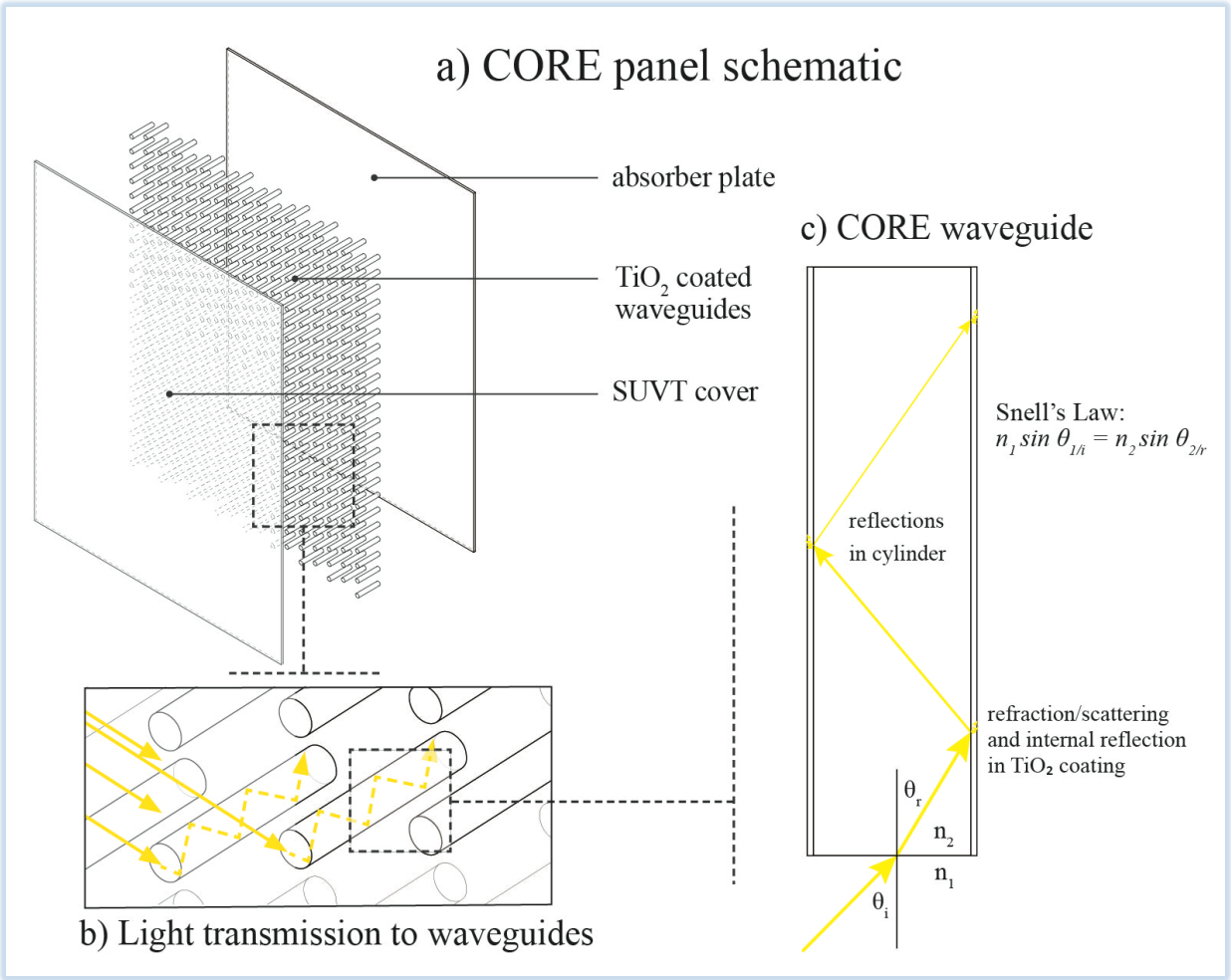

Figure 4.1: a) Schematic of CORE Reactor, b) light transmission to waveguides and c) UV transmission through waveguides

At the back of the panel is an absorber plate for thermal gain. Behind the plate is a reservoir of the same dimensions as the flow through area of the front of the panel. Between the reservoir and the surrounding environment as well as around the edges is a layer of insulation. In this study the panel dimensions are assumed to be 1 meter square with the depth being a decision variable.

The cylindrical waveguides are staggered in arrangement, with a spacing of 2cm on center. The system is pump forced with a volumetric flow rate of 50L/min. The flow is maintained in the laminar regime in this study, between $100 < Re < 800$, as the tube bank constrains vortex shedding up to a much higher Reynolds number (transitional flow begins at about $Re \sim 800\text{-}1000$). [22] Increasing the flow rate will increase removal rate, but because the panel is a recirculating system flow rate will not significantly affect the thermal gain, and so is left aside as a decision variable in this study.

III. Analytical Methods:

3.1 Mass transfer model

Prototypes of the CORE panel have been studied (as in chapter III and in [23]) and its removal potential for methylene blue (MB) determined from the experimental results shown in experiment figure 2. Studies have shown that *E. coli* inactivation due to heterogeneous photocatalysis is consistently more pronounced than for MB [8], and so we use the removal results for MB found in the lab for the reaction rate of organic contaminants in the current study. Those reaction rates have been scaled to the current mathematical model.

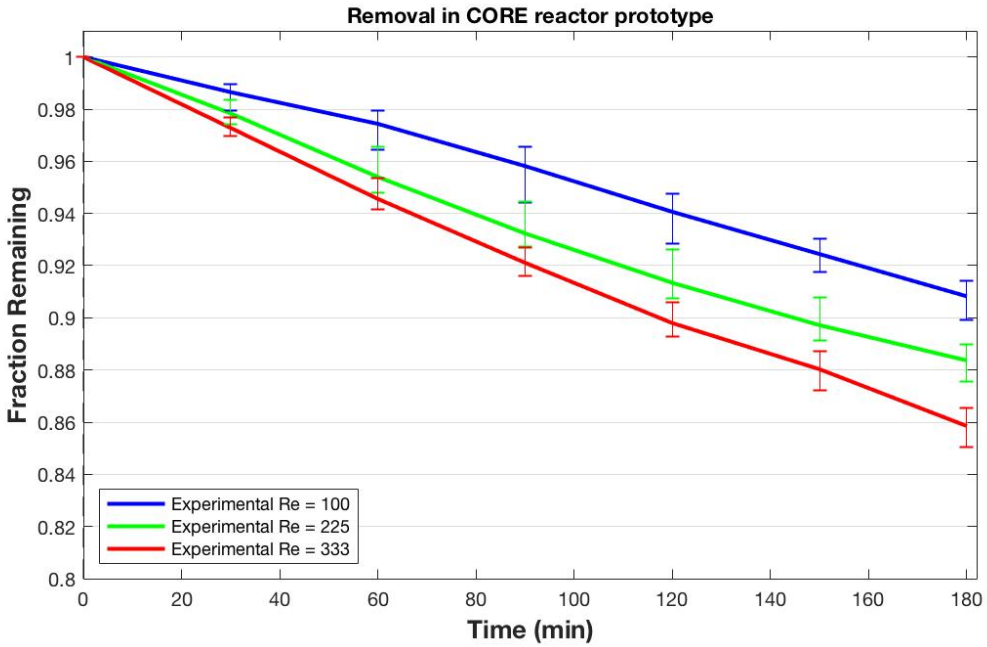

Figure 4.2: Removal of MB in experiments on CORE prototype (note that this figure is the experimental portion of Fig. 3.8)

In brief, the experiment mentioned above (in the previous chapter) showed that the majority of all photocatalytic removal in the CORE panel occurred due to light incident on the cylinder heads (as opposed to UV light passing through water to the cylinders). The system is modeled as a continuously stirred batch reactor (CSBR), and the removal within was assumed to be first order kinetics (though in the plot above we see pseudo-zero order kinetics due to slow reaction). The volumetric reaction rate in the above experiments for removal due to the cylinders alone can be described as a function of Reynolds number (in the laminar range):

$$k_v = (0.012Re + 3.96) * 10^{-4}\ \mu\text{M/dm} \tag{1}$$

The kinetics of the CORE system in the optimization study are expected to behave the same. As the HRT in the panel and reservoir is significantly faster than the time increments of the study the system will be analyzed as a CSBR, with the concentration of contaminants described by:

$$C(t) = C_o e^{-k_{sc}t} \tag{2}$$

$$k_{sc} = k_v * f(S_{rat}, V_{rat}, Cyl_{rat}, I_{rat}, T) \tag{3}$$

where t is the time increment of 10 minutes. The kinetic constant k_{sc} is scaled to the reactor from the experimental results as a function of surface area, volume, cylinder count, light intensity, and temperature (according to the Arrhenius rate). Photolysis (also studied and significant in the initial experiments) is also scaled to the simulation and applied. The particle interception studied in Chapter 2 shows that

little is expected for the solid fraction and cylinder size of this panel, and is at best a third or fourth order effect in removal; it is thus neglected in this model.

The efficiency of photocatalytic systems is taken from the quantum utilization of photons for conversion of a contaminant, and is described in section 4.2.

3.2 Thermal model

The thermal model used is one-dimensional and describes energy flow in the panel through conduction, convection, and radiation. The linearized equations are elaborated from an electrical resistance analogy model as introduced in [15], for details see Figure 4.3. Radiation coefficients are calculated iteratively before being applied. In order to simplify the model, the following assumptions are made:

- The temperature in the panel layers is the same as the surrounding fluid temperature
- Thermal exchange between the cylinders and fluid medium are not considered.
- Irradiance not reflected out of the panel is absorbed in the fluid or absorber plate and converted to heat.
- Ambient temperature is considered equal on all sides of the panel.
- Shading and fouling of the collector surfaces is negligible.
- The thermal mass of the cylinders is lumped together with the thermal mass of the fluid for determining temperature change

Ambient temperature is taken from average data for the days considered in ten-minute intervals.

The model is further developed by considering the effect of Building Added (BA) panels vs. Building Integrated (BI) systems for thermal gain. [24] The BA system is thought of as a panel system on any rooftop, where the angle of tilt is free. BI systems could theoretically have any angle of tilt as well if imagining less traditional façade morphology, however in this study BI systems are modeled as having a tilt of 10 degrees or less from the vertical on the horizontal axis. BI systems have a lower overall heat loss coefficient due to their integration with wall insulation along the rear and sides and no convection across the back of the panel. Building facades also have more surface area available, and thus there is more panel available space for urban implementation.

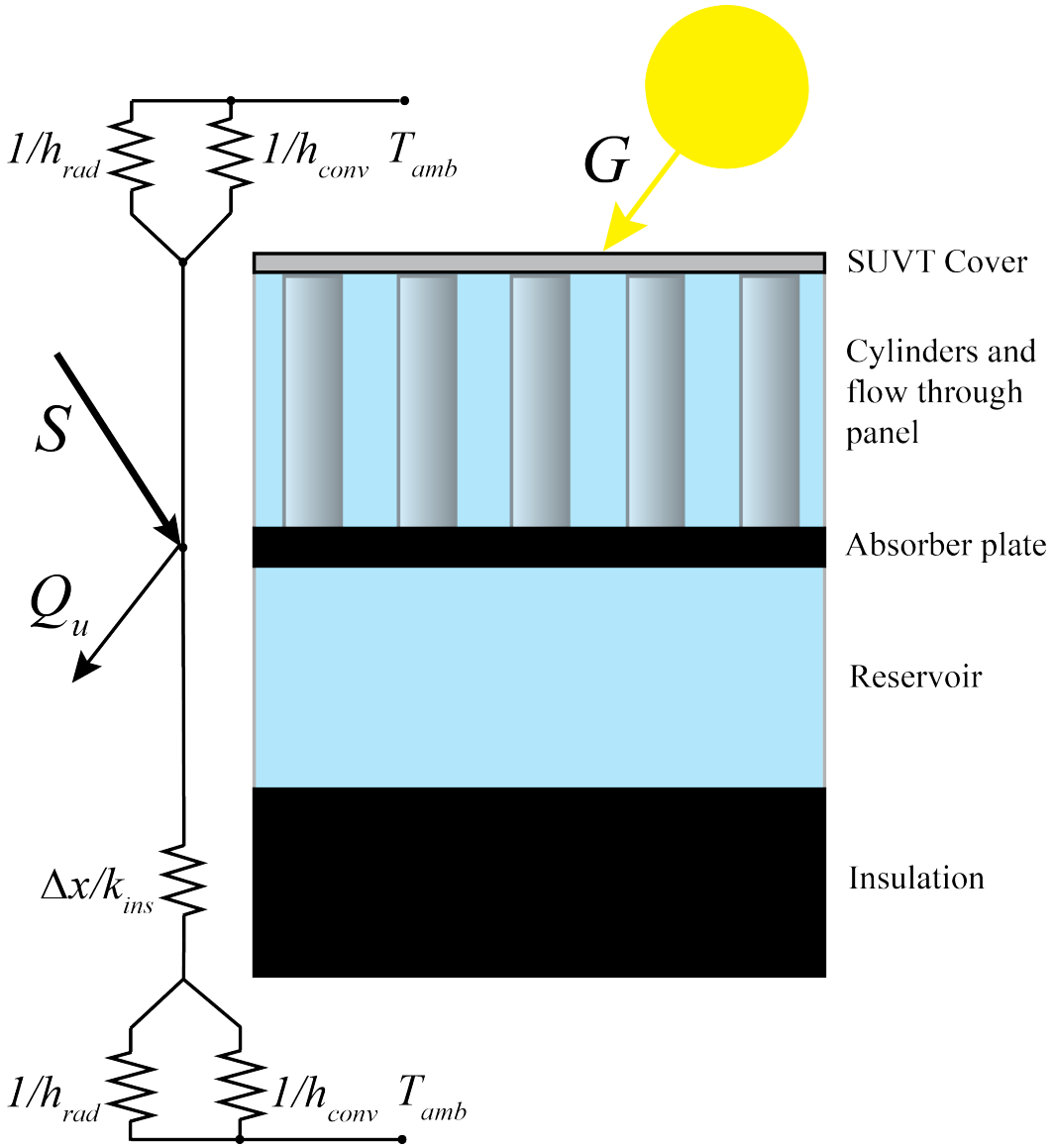

Figure 4.3: Resistance model and depth schematic of CORE panel

The basic equation describing the thermal balance in the panel is given by:

$$Q_u = A_p\left[(S * \tau\alpha) - U_L\left(T_p - T_{amb}\right)\right] \quad (4)$$

where Q_u is the useful heat, A_p is the area of the panel face, $S * \tau\alpha$ is the insolation and transmission/absorption coefficient defining the heat source, U_L is the overall heat loss coefficient described below, T is the temperature of the panel and ambient conditions respectively. As previously described, insolation is derived from the solar data, and the transmission absorption curve is calculated by degree of incidence.

The radiation coefficient of the cover of the panel to the air is found by applying:

$$h_r = \varepsilon_c \sigma ({T_c}^2 + {T_{amb}}^2)(T_c + T_{amb}) \quad (5)$$

where ε_c is the emissivity of the SUVT cover (0.94 for clear acrylic) , σ is the Stefan-Boltzmann constant, and T_c is the cover temperature. As the cover/panel temperature is unknown, calculations are applied iteratively in order to estimate the cover temperature and radiation losses at each interval.

Forced convection due to wind is the primary mechanism for loss through the panel surfaces, and is considered in parallel with radiation out the front/back and in series with conduction through the back and sides, as is shown in the resistance diagram of Figure 4.3. Material properties of the system are detailed in Table 4.1.

The thermal efficiency of the panel is the total energy converted to heat gained above ambient temperature over the panel area and insolation instantaneously or over a specified time.

$$\eta_T = \frac{\int Q_u \, dt}{A_c \int G \, dt} \quad (6)$$

where:

$$Q_u = m_w c_w (\Delta T_w) \quad (7)$$

Above m_w is the total mass, c_w the lumped specific heat, and T_w is the temperature of the water.

Upon achieving temperature of 60°C for 5 minutes (pasteurization) or 3-log *E. coli* inactivation, the heated water is evacuated for heat recovery and reuse and the panel refilled with untreated greywater.

Table 4.1: List of parameters used in simulation

Parameter	Value	Parameter	Value
SUVT transmissivity	0.9	$c_{p,cyl}$	10^3 J/kg °C
Absorption of plate	0.96	$c_{p,plate}$	500 J/kg °C
ρ_{cyl}	$2.5*10^3$ kg/m^3	ε_{cover}	0.9
k_{ins}	0.045		

IV. Multi-objective optimization of PC-T models:

The PC-T model developed in the previous sections shows tradeoffs between performance depending on the values of certain parameters. Analyzing these design variables individually is a possibility, however a time involved one. Further, because CORE is a hybrid panel system, there is no 'optimal' configuration of decisions variables, as maximizing thermal performance will adversely affect disinfection below pasteurization temperatures. For this reason the use of a multi-objective evolutionary algorithm is applied to the problem in order to understand more fully the interaction of parameters on efficiency and overall output. In addition to the simultaneous matching of optimal decision variable values for multiple configurations, the results also promise to yield insight into how these parameters affect panel performance for possibilities in application to varied environments.

4.1 NSGA-II: Genetic Algorithm for multi-objective optimization

The design of a hybrid solar panel system can be described as a multi-objective optimization problem (MOOP) with two or more conflicting objective functions $f_m(\mathrm{x})$ are maximized/minimized using bounded decision variables expressed as a vector *x*, subject to certain constraints.

Mathematically, the formulation of the MOOP [25]:

Minimize(Maximize):

$$f_m(\mathrm{x}), \qquad \mathrm{m} = 1,2,\ldots.\mathrm{M};$$

subject to:

$$g_j(\mathrm{x}) \geq 0, \qquad \mathrm{j} = 1,2,\ldots\mathrm{J}$$
$$h_k(\mathrm{x}) = 0, \qquad \mathrm{k} = 1,2,\ldots\mathrm{K}$$
$$x_i^{(L)} \leq x_i \leq x_i^{(U)} \qquad i = 1,2,\ldots n$$

where the solution is the vector $(x_1, x_2 \ldots x_n)^T$ of n decision variables. The solution set to a multi-objective problem is a pareto-front in the objective function space, where each point is a potential min or max to the objective functions that provides no better tradeoff in solving each objective.

Evolutionary algorithms begin with random generation of possible solution points with in the variable bounds of the problem, an assessment of their fitness, and the selection and recombination of the solution points that produce a better solution of the objective functions to generate new starting points. Genetic "factors" such as how the next set of start points are derived from previous solutions vary. Points in each population are assigned a rank by the dominance of the objective values and are then used to generate a next set of points in the design space. There are a number of popular GA routines for MOOPs used, distinguished by how they generate and select next sets of solution points. [26]

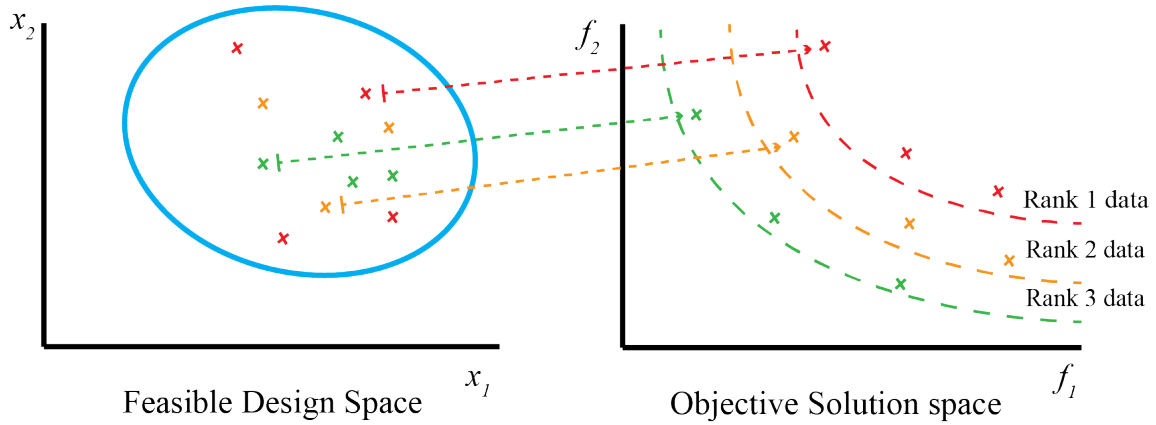

Figure 4.4: Variables in the design space become a pareto-front of solutions in the objective space. The rank of the solution reflects successive generations of trials in the design space

The NSGA-II algorithm uses an elitist, non-dominated, space preserving sorting algorithm: it selects potential solutions and their offspring in each generation by finding the points $(x_{1i}, x_{2i}...x_{ni})^T$ that are on the front of optimal objective values in the i^{th} generation not only by the fact they are not dominated by other solutions, but their crowding distance in order to maintain the shape of a front in the final set of solution vectors. [27]

The design parameters studied require that there be a conflict in the objective function evaluations, and are chosen accordingly. [28] In this case panel inclination is not known, and thus is used a conflicting decision variable, the tilt of the panel having better removal potential if it is not normal to solar irradiance, and achieving much higher thermal performance if it does. Other decision variables are the packing factor of the cylinders and the depth of the panel and reservoir. The panel depth is bounded by the constraint that BI/A panels need a relatively slender profile architecturally, and at its minimum depth to roughly allow a slenderness ratio of 5:1 (length:diameter) for the waveguide. As discussed in chapter III, this slenderness allows for a second reflection at most incident solar angles. See Table 4.2 below for details on these three continuous parameters that constitute the design space variables.

Table 4.2: Parameter bounds

Symbol	Decision Variable	Range
π	Inclination of panel	$0 < x(1) < 90$ (degrees)
d_{cyl}	Diameter of waveguides	$0.5cm < x(2) < 1.5cm$
th_{pan}	Panel depth	$2cm < x(3) < 10cm$

4.2 Optimization Problems

Several 2-dimensional optimization problems have been formulated for the CORE PC/T panel. The environmental data applied to the panels are generated from solar angle files from coordinates of Berkeley, California on the vernal/autumnal equinox and solstices, 2014 [29] and from ASHRAE guidelines for thermal panel verification. [30] Ambient temperatures have been applied from climate data from those days, and averaged over a period of eight years. The panels are oriented due south in this study.

MOP1:
The first optimization problem is to maximize the quantum yield and thermal efficiency of the reactor. The quantum yield efficiency is derived from the surface reaction rate:

$$\theta_{UV} = \frac{k_{app,s}}{incident\ UV\ intensity} \tag{8}$$

where:

$$k_{app,s} = k_v \frac{V}{S} \tag{9}$$

and is generally on the order of 10^{-3} μM/dm. It is challenging to meaningfully analyze the joint quantum and thermal efficiency as is frequently done with the hybrid PV/T technologies [31] owing to that the thermal efficiency of panel systems can be on the order of 1. In this study MOP1 the daily averaged time dependent efficiency of both physics is maximized:

Minimize: $\{-f_{1,1}(x), -f_{2,1}(x)\}$

$$f_{1,1}(x) = -\frac{1}{t_{tot}} \int \theta_{UV,i}\, dt = -\bar{\eta}_{PC} \tag{10}$$

$$f_{2,1}(x) = -\frac{1}{t_{tot}} \int \eta_{T,i} dt = -\bar{\eta}_T \tag{11}$$

The objective functions are given a negative in order to maximize, as the NSGA-II is inherently a minimization procedure.

In this study and in the next MOP, the daily solar irradiance data previously mentioned is used. It is possible to find the averaged efficiency in this manner using any number of combined daily data taken throughout the year. As this is an exploration in feasibility, the equinox data alone is used.

MOP2:
The second optimization problem juxtaposes the practical objectives of volume total disinfected water produced and total energy gained. For the purposes of this study, greywater is considered recyclable after log3 concentration reduction. [32] Heat recovery is engaged once the disinfected water in the panel has been evacuated. The purpose of exploring the produced quantities is to examine the potential for site integration, and to determine how many panels per person in a region would be required for adequate residential/commercial functioning. The objectives are formulated as such:

Minimize: $\{-f_{1,2}(x), -f_{2,2}(x)\}$

$$f_{1,2}(x) = (Volume\ clean\ H_2O\ for\ reuse)\ VHR \tag{12}$$

$$f_{2,2}(x) = (Produced\ Thermal\ Energy)\ PTE \tag{13}$$

Additional code is used for GA tuning and visualization.

V. Results and Discussion:

5.1 Efficiency

The panel model considers both disinfection and thermal performance in both problem statements. The input data is temperature and solar angle for four days of the year, the solstices and equinoxes respectively. Examples of daily removal and temperature profiles for a specific reactor configuration on an equinox day is shown in Figure 4.5 below:

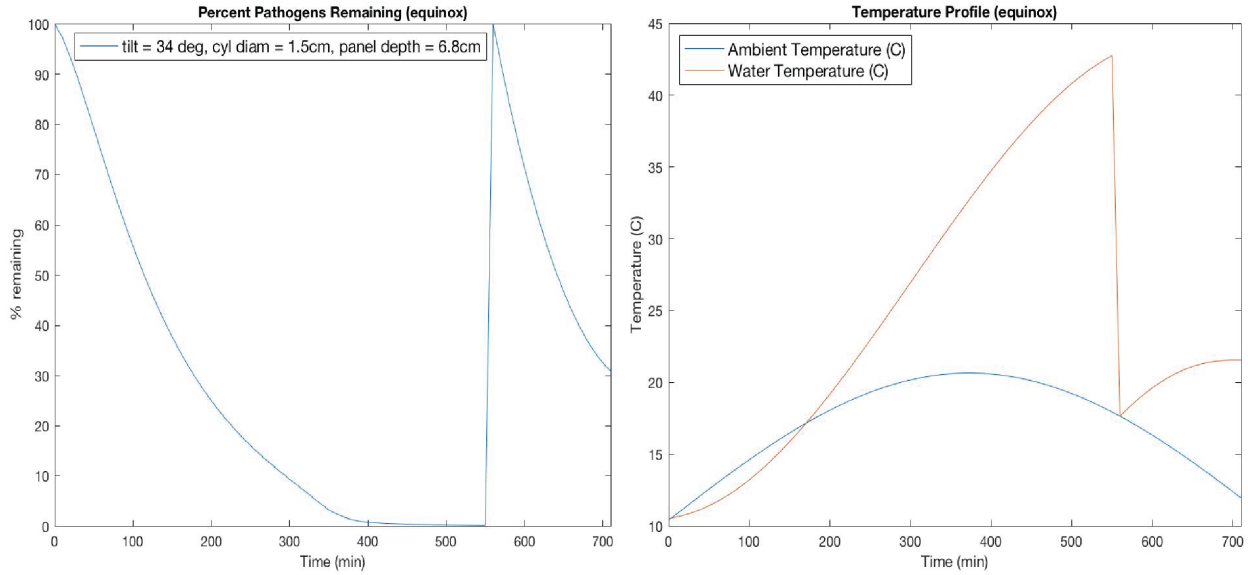

Figure 4.5: a) CORE panel pathogen level over one equinox day and b) heat gain over the equinox day

In this study it is considered important for the panel system to disinfect at least one full load of water in a day. There are many configurations that will do this on some of the days considered (and many more that will not), but only few that will disinfect a full panel load on all days tested. When considering efficiency, panels that didn't exchange at least one full load on any days were excluded from consideration in the results. The figures below show panel results for efficiency when a panel exchanged at least once (Figure 4.6) and when a panel disinfected a load on every day in consideration (Figure 4.7):

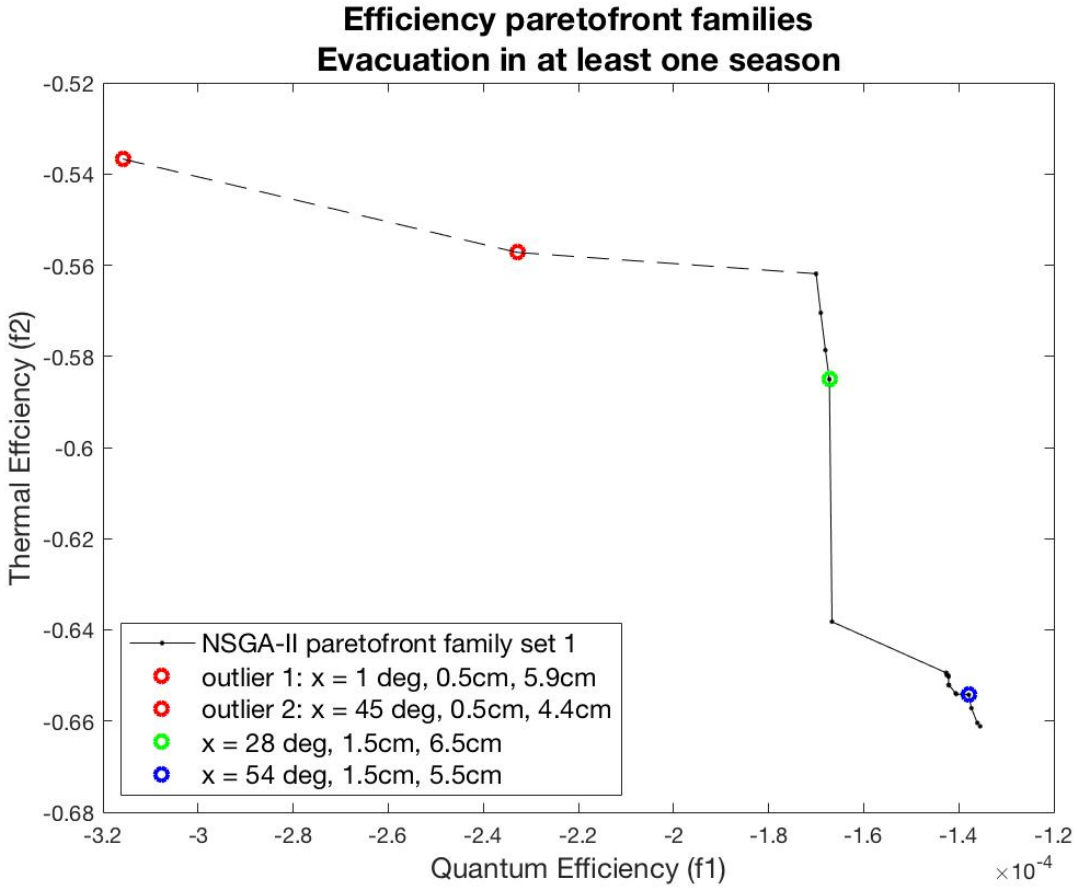

Figure 4.6: Average quantum and thermal efficiency for evacuation on at least one day

The results of MOP1 show pareto-curves that do not demonstrate clear tradeoffs with gradual variation in parameters. This roughness of the resulting front is due to the problem constraint of clearing at least one batch in at least one or in every season. For the following paretofront plots we see either outliers alone (Fig. 4.6) or families with distinct sets (Fig. 4.7). The sets are connected with dashed lines to show the border of the optimal fronts even though they are not continuous.

In Figure 4.6 we see several panel parameter configurations revealed for optimal efficiency with evacuation in all seasons. The family solution set appears as a

cluster of panel configurations (examples of the set parameters are shown in the figure with markers and in the legend). A panel type appears as an outlier at nearly vertical inclination, suggesting that some optimality for façade mounted systems is possible. However the more interesting variation is seen between the two extreme panel configurations, where the waveguide diameter is the primary difference. This is particularly evident in Figure 4.7, where evacuation in all seasons is shown.

While the efficiency plots do not speak to over all output, this relationship is relevant to further design considerations. Variation of quantum and thermal efficiency by cylinder diameter (described as panel solid fraction) are seen below in Figure 4.8 for single day (equinox) efficiency. Over all the efficiencies are comparable to expected efficiency values for both TiO_2 photocatalysis and for batch thermal collectors. [33]

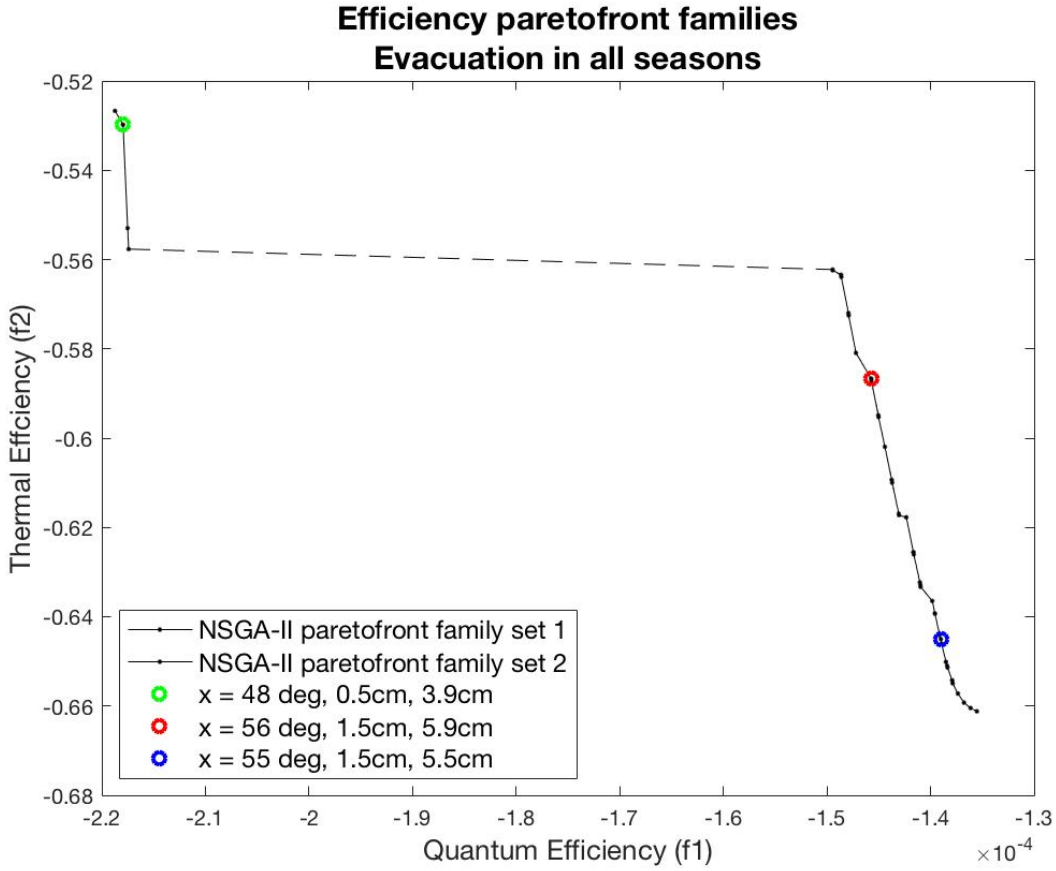

Figure 4.7: Average quantum and thermal efficiency for evacuation on all days

For the evacuation on all days the number of feasible designs that optimize efficiency are fewer, but show a similar trend: thinner cylinders produce greater quantum efficiency. In the above plot we see one outlier (the green marker) to a panel configuration with only slight variation between parameters. For efficiency throughout a year, it is clear that the panels are better inclined in this location, and thus are better suited for roof installation.

The tradeoff between quantum and thermal efficiency by cylinder variation can also be described as a packing density of cylinders, or the solid fraction of the waveguide/fluid matrix in the panel. The higher quantum efficiency is seen where the volume of fluid increases and the surface area of the cylinders decreases (which might be expected based on its formulation), however the volume and area relationships in the efficiency are inversely proportional in the reaction rate constant formulation and thus the effect should cancel out for the quantum efficiency. Thermal efficiency has an inverse tradeoff with variation in waveguide diameter, increasing with packing density. Figure 4.8 shows the relationship between these efficiencies and variation in solid fraction in the CORE panel.

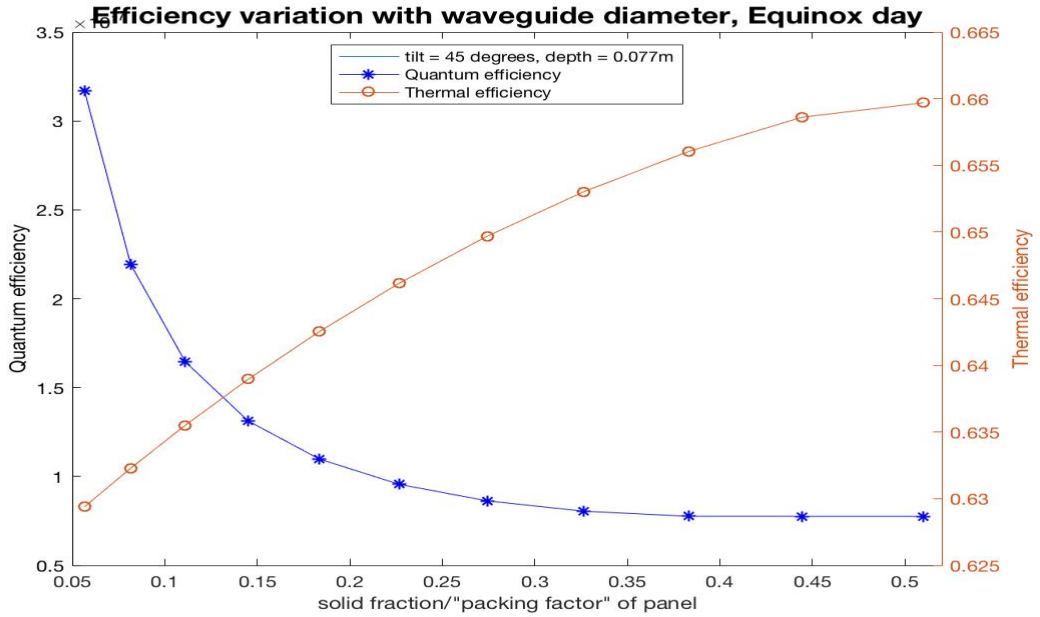

Figure 4.8: Variations of efficiency by cylinder diameter

5.2.1 Volume removal and overall optimal configurations

The CORE panel's primary technical objective is to produce cleaned water, as that is what is novel about this hybrid technology. For this reason the results of MOP2 are given more consideration when applying the NSGA-II procedure. The pareto-optimal solutions for MOP2, Figure 4.9, show dense final populations. There are few parameter sets that will perform well for water cleaning while maximizing heat gain when also controlled by volume. Figure 10 further amplifies this: when no minimum constraint on volume production was given, the resulting pareto-front (in black) shows a very similar front of optimal solutions in the restricted range of optimal solutions, but indicates solutions where there is no evacuation and higher heat gain. The volume of water that is cleaned for recycling ranges from 81L to 87L, and the amount of heat captured above the ambient temperature is on the order of 20MJ. While the range is small, both reusable water volume and heat gain represent

a significant contribution to the amount of resources used in a day by the average household.

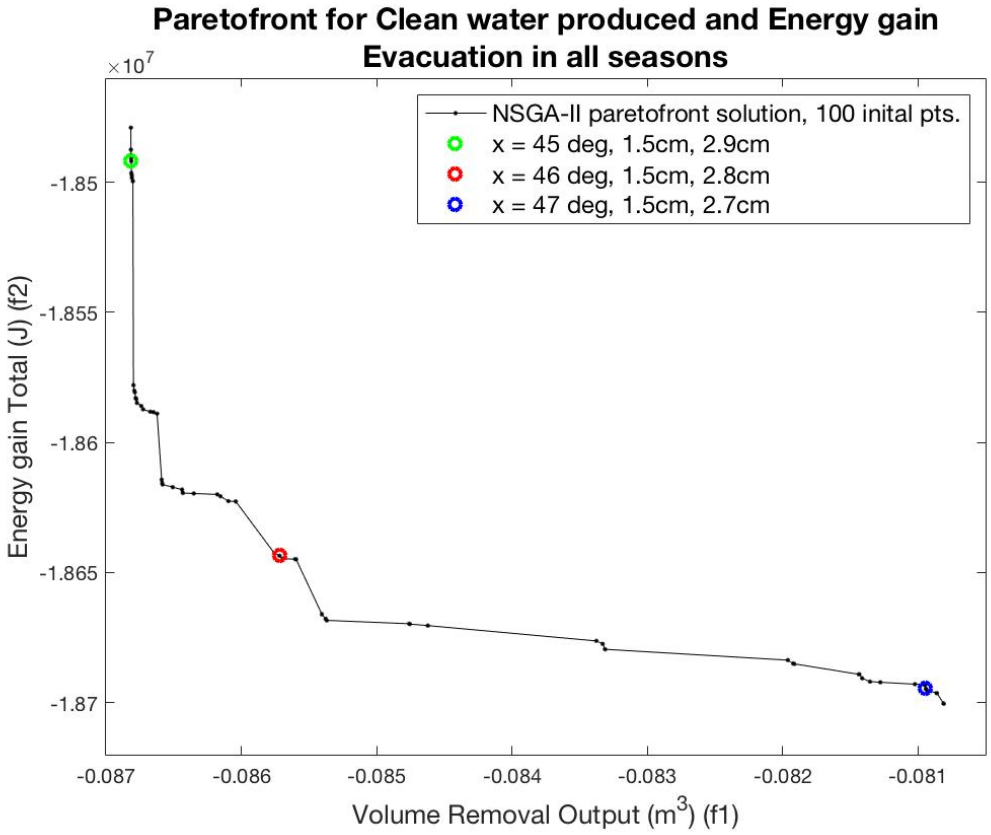

Figure 4.9: MOP2 output for evacuation in all seasons

Optimal volumetric output results show that the simulation favors conditions that do not have the highest photocatalytic efficiency. The solution vectors show that there is a clear dominance of designs where the cylinder diameter is at the upper bound of 1.5 cm. A higher packing density of waveguides is more effective for removal volume total, even if not operating at the highest efficiency. While the tradeoffs are still visible in the fronts, however there is a high degree of sensitivity in the parameter configurations. There are few panel configurations available for maximum removal potential, likely owing to the overall slow reaction rate.

As is seen in Figure 4.9, for full evacuation in each season the tilt needs to be at 45-47 degrees from vertical, the diameter of the waveguides held at 1.5cm diameter, and the overall depth of the panel around 5.5cm. The slenderness of the waveguides in this configuration is 0.53 (maximizing area active due to first and second reflection areas) and the solid fraction of the panel front is 0.51. The tilt angle in these results show that the panels are best suited for rooftop installation, were it is expected that the average best angle is 45 degrees. Studies have shown that optimal angle is not only given by latitude, but is longitudinally dependent due to climate and meteorological variation, that is each specific location has a specific

optimal angle of inclination for insolation [34], [35]. Our results suggest that without climate specific information, the hybrid CORE is best suited for all seasons at the average tilt of 45 degrees in Berkeley, CA. It is clear that for rooftop installations, the tilt angle and panel depth are important parameters and must be ensured to be within a specific and limited range. The least sensitive of these solutions calls for a systems that is oriented at 46 degrees and has a total water depth of 5.6 cm for the combined waveguide front and reservoir back of the CORE panel.

Overall, the objective space demonstrates a high degree of sensitivity to the parameters. The relative weakness of the reaction rate for TiO_2 coated waveguides constrains the range of design parameters. When the NSGA study does not include evacuation constraints in the objective evaluation, the higher heat gain is somewhat marginal (~10%), and thus we conclude that where there is any potential use for heat gain and water disinfection, the hybrid panel is a more useful model than thermal gain panels alone. Again, the dashed lines represent borders between solution vector sets on the resulting paretofront, and the blue dot shows maximum heat gain when no evacuations occur.

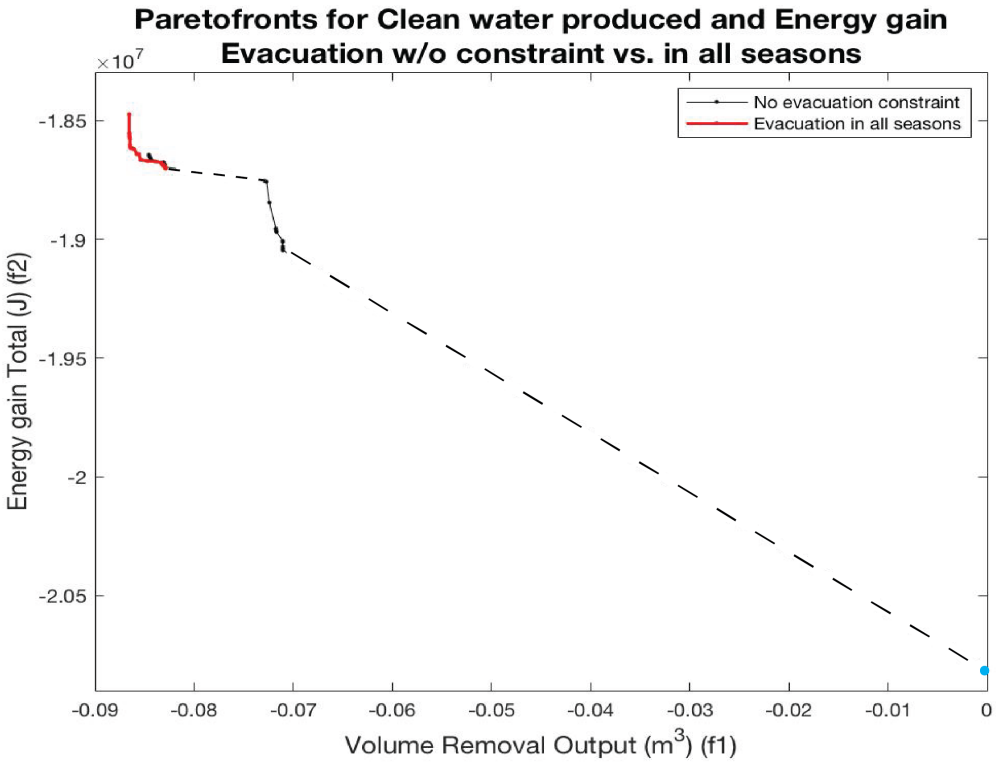

Figure 4.10: CORE output in all seasons and no volume removal constraint

5.2.2 BI system optimization

A further test performed for feasibility of traditional façade BI systems was performed by changing the bounds on tilt axis variable x(1) from 0 to 10 degrees.

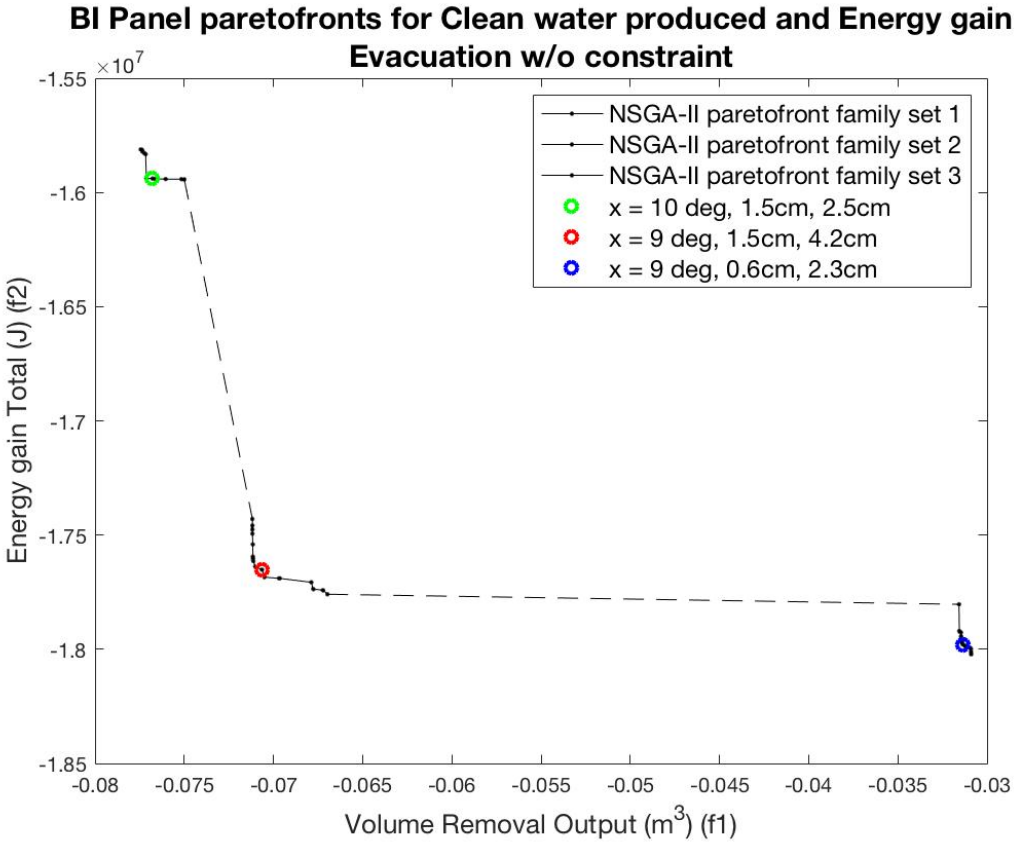

Figure 4.11: BI CORE panel removal averaged over all seasons, no evacuation constraint

The BI panel constrained to a horizontal tilt axis between 0 and 10 degrees form the vertical shows that it is feasible for CORE to function as a façade integrated system. While no configuration of parameters resulted in removal in all seasons, (summer was a limitation due to high average insolation angle difference), the solution front shows groupings where there are panel configurations that a panel that gathers heat for climate conditioning during summer while functioning as a hybrid grey water recycler/thermal gain panel during other seasons might be desirable for some applications. The use of doped TiO_2 is also a possibility to increase the reaction rate for BI panels, making them functional for all seasons. Doped titania has shown increase in the rate constant for removal of organic contaminants of up to 5 times. [36] A preliminary exploration of amplified *k* values for BI systems showed that an increase of the kinetic constant by 2.5 times showed significant increase in removal as well as removal in all seasons. The use of doped catalyst would increase cost, but also guarantee effectiveness of the CORE panel type for BI systems in terms of contaminant removal and disinfection.

5.3 Further discussion and directions

The simulation results show that the combination of pathogen removal and heat gain in a single panel system is feasible with this prototype in the area of Berkeley, CA., given that sufficient care is taken in installation. As with the models designed for optimal efficiency, these panels must be installed as part of a rooftop system to accommodate the necessary tilt angle for buildings with a purely vertical façade in order to be operational in every season. Façade panels could certainly be used for daily evacuation if there is sufficient tilt in surface of the building, some non-traditional buildings such as this do exist. Figure 4.11 does show that BI panel systems could also be used, but that they would not be useful for greywater recycling in all seasons, even though they would still function just fine for thermal gain during those times. In a real system set up, further investigations must be made to determine the pumping power required for the movement of water up to the roof and for redistribution back into the building infrastructure, as well as for heat exchange or radiant heating use. As well the actual temperature of the water entering the system must be accounted for in the thermal gain calculations.

The use of multi-objective optimization routines to access the effects of multiple parameters in a single simulation run provides in depth understanding of the performance of a complex system. Simultaneously testing the effect of many parameters in an optimization routine dramatically speeds understanding of interaction effects as well as the generation of a set of optimal types given variation in the parameters chosen. Though the set of design parameters was limited in this study (each variable added to the set of parameters increases the simulation time), further research will investigate the effect of additional parameters to expand on the range of the solution space.

VI. Conclusion:

"Green" technologies have received increasing attention over the past few years, especially multi-purpose and building integrated strategies. In this study a panel prototype so far only seen in laboratory conditions has been simulation tested for performance in solar conditions present at the site of UC Berkeley, and optimized using the fast elitist multi-objective algorithm NSGA-II. The results of the optimization procedure show few panel types that will perform effectively in the region considered. Other optimization objectives for the CORE panel can also be considered, such as optimizing for water retrieval in summer and heat recovery in winter. Overall the application of the GA to these multi-purpose panel types gives heartening results, for both understanding essential parameters for performance as well as what must be considered in site by site application. Further studies must account for the contribution of other as of yet unexplored parameters, such as pump power in relationship to loss of energy use and removal gain (higher pump activity generates higher convection to reactive surfaces for greater removal, yet draws more power away from output).

Efficiency pareto-fronts show that there is a competition for maximal efficiency between models based on the packing factor of waveguides, with more waveguide density producing higher heat efficiency and vice versa for photocatalytic efficiency. Clear tradeoffs for output for heat and volume of clean water are not as visible due to the constraint of a slow reaction for titania photocatalysis. If doped TiO_2 were substituted the surface kinetic constant would dramatically increase (due to visible light exciting electrons beyond the band gap) and the removal rate of pathogens would similarly increase. Such an increase would enable a much greater number of panel configurations to exist, and thus increase the flexibility of functioning systems as well as invite deeper exploration of possible configurations using multi-objective optimization.

References:

[1] San Francisco Health Code, *ARTICLE 12C: ALTERNATE WATER SOURCES FOR NON-POTABLE APPLICATIONS*. 2016.

[2] K. Hashimoto, H. Irie, and A. Fujishima, "TiO 2 Photocatalysis : A Historical Overview and Future Prospects," vol. 44, no. 12, pp. 8269–8285, 2005.

[3] D. F. Ollis, "Photocatalytic purification and remediation of contaminated air and water," *Comptes Rendus l'Academie des Sci. - Ser. IIc Chem.*, vol. 3, no. 6, pp. 405–411, 2000.

[4] T. T. Chow, "A review on photovoltaic/thermal hybrid solar technology," *Appl. Energy*, vol. 87, no. 2, pp. 365–379, 2010.

[5] S. Mohammad, H. Hashemi, J. Choi, and D. Psaltis, "Solar thermal harvesting for enhanced photocatalytic reactions," *Phys. Chem. Chem. Phys.*, vol. 16, no. 11, pp. 5137–5141, 2014.

[6] S. Malato, J. Blanco, D. C. Alarcón, M. I. Maldonado, P. Fernández-Ibáñez, and W. Gernjak, "Photocatalytic decontamination and disinfection of water with solar collectors," *Catal. Today*, vol. 122, no. 1–2, pp. 137–149, 2007.

[7] T. Van Gerven, G. Mul, J. Moulijn, and A. Stankiewicz, "A review of intensification of photocatalytic processes," *Chem. Eng. Process.*, vol. 46, pp. 781–789, 2007.

[8] O. Tsydenova, V. Batoev, and A. Batoeva, "Solar-Enhanced Advanced Oxidation Processes for Water Treatment : Simultaneous Removal of Pathogens and Chemical Pollutants," *Int. J. Environ. Res. Public Heal.*, vol. 12, pp. 9542–9561, 2015.

[9] R. J. Braham and A. T. Harris, "Review of Major Design and Scale-up Considerations for Solar Photocatalytic Reactors," *Ind. eng. Chem. Res.*, vol. 48, no. 8, pp. 8890–8905, 2009.

[10] K. Hofstadler and S. Novalic, "New Reactor Design for Photocatalytic Wastewater Treatment with Ti02 Immobilized on Fused-Silica Glass Fibers: Photomineralization of 4-Chlorophenol," *Environ. Sci. Technol.*, vol. 28, no. 4, pp. 670–674, 1994.

[11] N. J. Peill and M. R. Hoffmann, "Fiber-Optic Cable Reactor for Waste Stream Remediation," *J. Sol. Eneergy Eng.*, vol. 119, no. August, pp. 229–236, 1997.

[12] W. Choi, J. Y. Ko, H. Park, and J. S. Chung, "Investigation on TiO 2 -coated optical fibers for gas-phase photocatalytic oxidation of acetone," vol. 31, pp. 209–220, 2001.

[13] R. W. Bliss, "The derivations of several plate efficiency factors useful in the design of flat - plate solar heat collectors," *Sol. Energy*, vol. 3, pp. 55–61, 1959.

[14] S. A. Klein, W. A. Beckman, and J. A. Duffie, "A Design procedure for solar heating systems," *Sol. Energy*, vol. 18, no. July 1975, pp. 113–127, 1976.

[15] J. A. Duffie and M. A. Beckman, *Solar Engineering of Thermal Processes*. New York: Wiley, 1991.

[16] L. . Florschuetz, "Extension of the Hottel-Whillier Model To the Analysis of Combined Photovoltaic / Thermal Flat Plate Collectors," *Sol. Energy*, vol. 22, pp. 361–366, 1979.

[17] H. A. Zondag, "Flat-plate PV-Thermal collectors and systems: A review,"

Renew. Sustain. Energy Rev., vol. 12, no. 4, pp. 891–959, 2008.
[18] T. T. Chow, "Performance analysis of photovoltaic-thermal collector by explicit dynamic model," *Sol. Energy*, vol. 75, no. 2, pp. 143–152, 2003.
[19] P. Dupeyrat, C. Ménézo, M. Rommel, and H. M. Henning, "Efficient single glazed flat plate photovoltaic-thermal hybrid collector for domestic hot water system," *Sol. Energy*, vol. 85, no. 7, pp. 1457–1468, 2011.
[20] J. Tamayo Vera, T. Laukkanen, and K. Sirén, "Performance evaluation and multi-objective optimization of hybrid photovoltaic-thermal collectors," *Sol. Energy*, vol. 102, pp. 223–233, 2014.
[21] J. Tamayo Vera, T. Laukkanen, and K. Sirén, "Multi-objective optimization of hybrid photovoltaic-thermal collectors integrated in a DHW heating system," *Energy Build.*, vol. 74, pp. 78–90, 2014.
[22] A. Žukauskas, "Heat Transfer from Tubes in Crossflow," *Adv. Heat Transf.*, vol. 18, pp. 87–159, 1987.
[23] V. Rao, "Heating and Treating Water with Sunlight: Solar Photocatalytic-Thermal Systems for a Sustainable Built Environment," UC Berkeley, 2018.
[24] C. Maurer, C. Cappel, and T. E. Kuhn, "MODELLING BUILDING-INTEGRATED SOLAR THERMAL SYSTEMS," in *Proceedings of Building Simulation 2015*, 2015, no. 1, pp. 2524–2529.
[25] K. Deb, *Multi-Objective Optimization Using Evolutionary Algorithms : An Introduction*. 2011.
[26] A. Ghosh, "Evolutionary Algorithms for Multi-Criterion Optimization : A Survey," *Int. J. Comput. Inf. Sci.*, vol. 2, no. 1, pp. 38–57, 2004.
[27] K. Deb, A. Member, A. Pratap, S. Agarwal, and T. Meyarivan, "A Fast and Elitist Multiobjective Genetic Algorithm :," *IEEE Trans. Evol. Comput.*, vol. 6, no. 2, pp. 182–197, 2002.
[28] K. Deb and A. Srinivasan, "Innovization: Discovery of Innovative Design Principles Through Multiobjective Evolutionary Optimization," in *Multiobjective Problem Solving from Nature*, J. Knowles, D. Corne, and K. Deb, Eds. Springer, 2008.
[29] "Solar Position Algorithm," *NREL*. .
[30] Ashrae, "Methods of testing to determine the thermal performance of solar collectors," vol. 2010, no. Ra, p. 41, 1993.
[31] N. Aste, C. Pero, and F. Leonforte, "Water flat plate PV – thermal collectors : A review," *Sol. Energy*, vol. 102, pp. 98–115, 2014.
[32] State of California, *Chapter 15 State Plumbing Code*. 2016.
[33] ISO/FDIS, "INTERNATIONAL STANDARD ISO / FDIS Solar energy — Solar thermal collectors — Test methods," 2013.
[34] T. P. Chang, "The Sun's apparent position and the optimal tilt angle of a solar collector in the northern hemisphere," *Sol. Energy*, vol. 83, no. 8, pp. 1274–1284, 2009.
[35] M. Z. Jacobson and V. Jadhav, "World estimates of PV optimal tilt angles and ratios of sunlight incident upon tilted and tracked PV panels relative to horizontal panels," *Sol. Energy*, vol. 169, no. December 2017, pp. 55–66, 2018.
[36] A. W. Xu, Y. Gao, and H. Q. Liu, "The preparation, characterization, and their photocatalytic activities of rare-earth-doped TiO2 nanoparticles," *J. Catal.*, vol.

207, no. 2, pp. 151–157, 2002.

Chapter V:
Summary and Future Research Directions

I. Motivation and Intention:

Water scarcity is already a problem countenanced by significant portions of the world's population, and it is one that promises to escalate in the near future. The connection of natural resource use via the Water-Energy nexus and the trend towards urbanization only amplifies the current and future predicted stresses on limited supplies. Strategies to confront these issues have been framed in this work as "Net-Zero" interventions; these are policies and technologies that can be grouped together by their design goals of reducing resource use, load on infrastructure, and the drive towards economic and ecological sustainability in the built environment. The challenges presented by the burgeoning built environment are ultimately an opportunity for engineering design to develop efficient, multivalent solutions that meet in the areas where these perils overlap.

This research proposes a multi-physics Net-Zero technological solution to the joint problem of water scarcity and high-energy use in the urban environment: building-integrated panel systems for on-site grey water recycling and thermal gain for climate control. The system is solar powered, local to the building, and uses the medium of the grey water itself as the working fluid for heat transport in a hybrid green design. The research directions described in this thesis are diverse as the project was undefined at the start and many possibilities had to be considered and explored before a prototype could be designed for experimentation. The previous chapters demonstrate the use of Finite Element Analysis modeling for estimating the significance of removal mechanics, laboratory based chemical reaction kinetics experimentation, and the use of mathematical optimization to narrow potential models to site-specific solutions for the chosen prototype design. This chapter summarizes the key findings of this research and proposes future directions for inquiry for each area in the preceding chapters.

II. Summary:

The conception of a solar active, building integrated panel system for grey water disinfection and thermal gain, required several directions of investigation. First, an exploration of the mechanisms that would need to be modeled in a full panel scale performance analysis revealed a void in the knowledge of particle interception modeling. Second, a novel multi-physics solution necessitated laboratory experimentation to characterize the removal potential and kinetics for the proposed CORE panel design. Third, a site specific performance evaluation of the full building integrated system in operation employed a mathematical optimization routine (NSGA-II) to determine feasibility and working parameters of the novel panel type. This dissertation offers experimental and modeling research to respond to the

questions that arose in these areas. Each of the chapters is prepared for publication with it's own reference section.

In Chapter 1, a literature review of areas pertinent to this research is compiled. This includes definition of the problem area, resource scarcity complications due to urban development, and the realm of innovations created to confront it centered on Net-Zero buildings. Opportunities for solutions are presented, grey water recycling and on-site, solar driven systems, before a description of the mechanisms at play in solar photocatalytic and photolytic systems. A review of the existing technologies related to water disinfection and thermal gain is then given. Finally, hybrid systems and building integrated technologies are described, and the inspiration leading to the CORE panel design is revealed.

In Chapter 2, the potential removal in a cylinder bank due to particle interception in moderate laminar flow is defined with a correlation based on Freidlander's interception efficiency. [1] The inspiration for this chapter is the gap in the literature discovered when researching the potential for particle interception as a removal mechanism in the CORE panel. Moderate laminar flows (*Re* regime above creeping flow and up to turbulent) had no representation in the literature on particle interception. Cellular models on creeping flow and turbulent flow across cylinders are well defined, but the CORE has constrained flow due the cylinder geometry, and operates in the moderate flow region. Using COMSOL and modeling the system, FE experimentation is used to develop a correlation that extends Freidlander's model to moderate laminar flows in cylinder banks, as well as a rule of thumb for cylinder bank particle interception based on variation in solid fraction. While the study elaborated on a previously unexplored area, it was determined that particle interception would not be a meaningful contribution to removal in the CORE panel.

In chapter 3, the CORE (Cylindrical Optical Reactive Elements) panel is defined and an experimental study to assess the disinfection potential and determine kinetics for the panel prototype is detailed. The experiment used the decolorization of a probe compound methylene blue to model the photocatalytic disinfection of *E. coli* bacteria under laboratory-simulated sunlight. Additionally, the photocatalytic behavior of the cylinders in isolation from photolysis of the bulk was examined by using a grate that blocked all other light except from the heads of the cylinders. The results showed that in the absence of photolysis, the photocatalytic removal was due almost entirely to light transmitted through the cylinders, rather than through the medium and incident on the outside of the cylinder surfaces. A correlation for cylinder mass transfer is derived from Chilton-Colburn analogy and compared to experimental results favorably. Beyond this, it was seen that photolysis was a significant factor in removal for the CORE panel system. The slow reaction is modeled as pseudo-zero order, and the results provided a basis for developing a mathematical model for extrapolating to a full panel system in the next chapter.

In chapter 4, the seasonal performance of the CORE panel in the solar conditions of Berkeley, CA. is modeled and analyzed with a mathematical optimization routine, the NSGA-II genetic algorithm. This study is seen as a pilot routine that could be performed to assess panel feasibility in variable environments and that could also be used to tune parameters for site-preferred outputs. This study made assumptions that the panel profile would need to remain relatively thin for building integration, and that the question of its use as a Building-Added or Integrated system could be addressed. Parameters considered are the tilt on the horizontal axis, the diameter of the cylindrical waveguides, and the depth of the panel. The two objectives examined are removal/heat efficiency, and daily clean water volume/energy outputs. The results show that there are feasible, though limited, panel types that function for removal in all seasons for the location examined. Building Added panels are the only type that achieves this in for all seasons, however the performance of Building Integrated panels (with rotation constraints for façade integration) is presented as well.

III. Future Research Directions:

This dissertation seeks to provide a series of studies that elaborate on the design and assessment of a novel solar Net Zero building integrated technology for photocatalytic disinfection and thermal gain. The result of these studies is ultimately more questions than answers, as is expected in large-scale research projects, some more important than others. While some of these more closely pertaining to the individual studies have been addressed in their respective conclusions, some larger questions remain unaddressed. I will look at a few of these below.

1. Titanium dioxide as photocatalyst

This research focused exclusively on fixed titania substrate as a photocatalyst, owing to its abundant use in industrial processes and low cost. Also shown in this research are the reaction limitations of an immobilized substrate, the very reason the wave guides are used in the CORE design is to increase active surface area and enhance the distribution of UV light. The slow reaction rate of solar TiO_2 photocatalysis is strongly affected by these limitations. However the mechanism of hydroxyl radical formation is achievable through a number of different means, not only through the use of other photocatalysts, but also through other oxidizing compounds. For example, the use of a slight amount of hydrogen peroxide, another oxidizing agent that decomposes quickly into water and oxygen, has been shown to dramatically enhance radical production when used along with TiO_2 in removal experiments, as well as to significantly reduce time to disinfection in photolytic processes. [2], [3] In the practical installation of any CORE system the effects of radical generation accelerants and photosensitizers such as doped catalysts (see chapter 4), need to be considered and analyzed, as any increase in reaction rate for disinfection and mineralization would dramatically affect the parameter choices made in the GA study, and potentially suggest fundamental changes to the geometry

of the wave guides. Ultimately, changes to the band gap activation energy of the catalyst and the addition of photosensitization components to the working fluid will amplify the efficiency of the system on the most basic chemo-mechanical level. There are multiple research directions available for photocatalytic reaction engineering, the most evident to me being the inclusion of visible-light reactive doped catalyst to increase removal volume and determine loss in terms of thermal capture (energy diverted from thermal gain to photocatlytic reaction) for over all residential outputs.

2. Panel specific changes – light capture and flow rate

The optical waveguides, which are employed fundamentally to hold and distribute the reactive material of the catalyst, are conceived of as simple cylinders in this work. It is easy to imagine light-concentrating waveguides, with convex lenses perhaps, or truncated conical sections that increase light concentration on the active photocatalyst coated surfaces. While such concepts were imagined during this project, simple cylindrical waveguides were employed primarily for their ease in prototype fabrication. The ray tracing programs employed, both the 3D models in TracePro 7.1 and the 2D Matlab models created by myself, can be been adjusted to investigate the effects of light capture by geometry of the surfaces and volume of the waveguides. Further investigations in topology optimization would be required for their generation and to determine the effect of such shapes on the flow field and in pollutant removal. Such studies have a fundamental physical intrigue, and while they were conceived of, the over all project goal of moving towards a functioning mathematical model took priority over optimizing light capture. There is substantial room here for topological optimization of the waveguides based on the objectives of light maximization instantaneously and over time based on a moving source.

In the GA study of Chapter 4, the flow rate was held constant under the assumption that it would only increase removal while not affecting thermal gain. What was not discussed was that for flow increase there would be increased pump energy cost which would decrease overall energetic gains. Thus another objective could be formulated using flow rate as a design parameter wherein the objective function relates losses due to pressure drop to removal volume and thermal efficiency, along these lines:

$$f_{i,j}(x) = \frac{\dot{m}_{H_2O}\Delta P}{\eta_p} \tag{1}$$

where ΔP is a function of *Re*, geometry, and surface roughness of the coated waveguides. Conceiving the energy cost of pumping as a negative component in the thermal gain objective could potentially increase tradeoffs between energetic and volume removal maximization, creating a broader spread between panel design parameters of functioning models. These are areas where specific changes to the

panel in terms of components and process variables generate new directions for research concerning the operation of the CORE panel technology.

3. Site specific integration

There is significant opportunity in a hybrid, multi-physics technology to tune the design parameters to site and environment specific requirements. For example, as a technology the CORE panel system for recirculating flow is simple and relatively low cost, the photocatalyst on the interior is inexpensive, durable, and counteracts fouling during operation. The figure below shows a table generated by the SOAP interdisciplinary research group at Berkeley, an EFRI sponsored project and the source of this research, where the context surrounding opportunities for community integration are given. [4] All of the areas considered below show high irradiance and thus potential for solar technology installation. However, in certain contexts, such as Phoenix, AZ, the over all cost of energy utilities are low compared to income, but there is significant water usage as well as scarcity. Here the CORE panel shows promise for both energy and water resource use reduction and would need to be tuned to account for both, but would have little current economic impact.

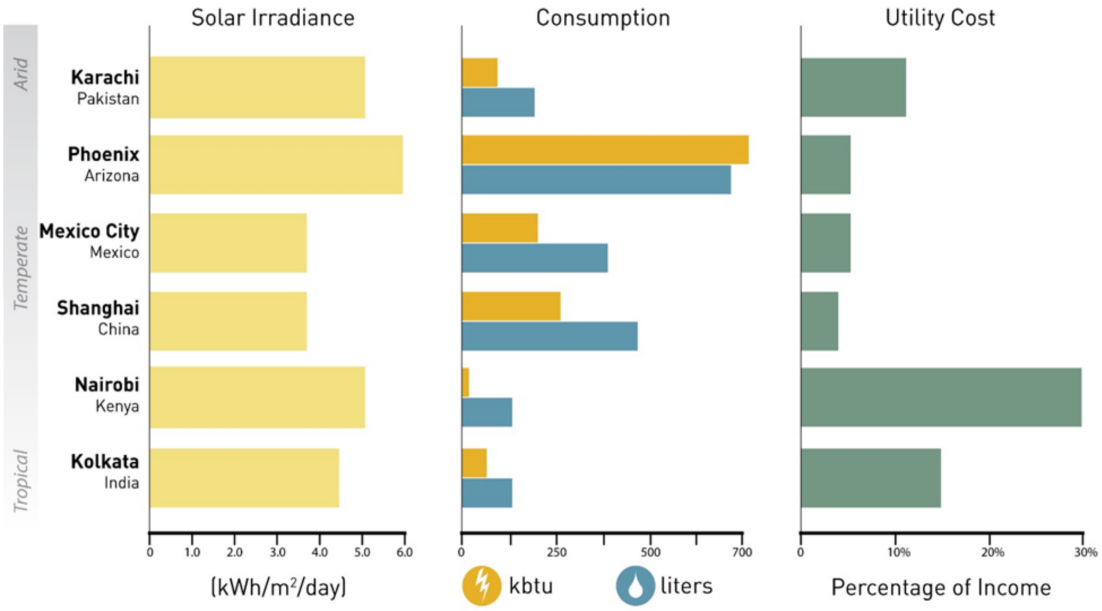

Figure 5.1: Context-dependent site considerations

Nairobi however, shows almost no consumption of energy resources alongside a need for water, where the cost for such services is a significant part of the household budget. Here the impact of the CORE panel system would be specifically economic, and tuned to water use reduction. This is an example of how site dependent context can elicit different considerations in design intentions, and provides insight into creating further inquiry into site-specific study design. This is a rich area for further exploration in particular in tandem with the use of mathematical optimization,

where the generation and weighting of objective function formations specific to context dependent design goals allows unique solutions for building integration of Net Zero technology.

4. Cost optimization and building system integration

Moving forward from studies of parameter arrangement and site adaptations, actual implementation involves venue identification and corresponding cost analysis. This area is currently unexplored in this research, but extends from designing the pretreatment, such as screening and sedimentation of actual greywater and the double piping required for on-site reuse, to conceptualizing the manner in which the heat will be recovered and used in the building, along with the equipment and its arrangement for doing so. The cost of the panel system is little discussed but could be the subject of an entire multi-objective study in itself, in particular when combined with the context dependent considerations described briefly above.

That significant opportunities for interdisciplinary research across the fields of architecture and engineering exist has been highlighted in my research. When considering the fabric of buildings and their connection within and to the urban environment, there is pressing need for collaboration and the development of mutual goals *and* the means for achieving them. Some of the challenges associated with Net Zero building technologies and architectural integration were mentioned in the literature review, however once again these challenges present opportunities for disciplines to generate coordinated bodies and spaces where novel inquiries could be formulated and pursued together. On the broadest level of directions pointed to in this research, interdisciplinary research in Net Zero technologies is the groundwork required for more focused investigations on its implementation and effects.

References:

[1] S. K. Friedlander, *Smoke, Dust, and Haze: Fundamentals of Aerosol Dynamics*, 2nd ed. New York: John Wiley & Sons, 2000.

[2] N. M. Mahmoodi, M. Arami, N. Y. Limaee, and N. S. Tabrizi, "Decolorization and aromatic ring degradation kinetics of Direct Red 80 by UV oxidation in the presence of hydrogen peroxide utilizing TiO 2 as a photocatalyst," *Chem. Eng. J.*, vol. 112, no. 1–3, pp. 191–196, 2005.

[3] B. J. P. A. Cornish, L. A. Lawton, and P. K. J. Robertson, "Hydrogen peroxide enhanced photocatalytic oxidation of microcystin-LR using titanium dioxide," vol. 25, pp. 59–67, 2000.

[4] V. Rao, H. Kagey, D. Campbell, S. Hermanowicz, and M. Gutierrez, "A Framework for Navigating Discontinuities in Interdisciplinary R&D: A Case Study in Building Systems Innovation," *unpublished manuscript*, UC Berkeley, 2016.

APPENDICES:

A.1 – Ray Tracing code from Chapter III

```
%% Ray tracer for Cylinder

% cylinder modeled in first approximation as two flat plates d apart

% note: dimensions in cm

clear all

% inputs
% angincrement = [15 30 45 60 75];
angincrement = [45];
% snell's number

snair = 1;
snmed = 1.5; %glass
snti02 = 2.3;

% angle of incoming light
% (note, might eventually loop through this and
% save the results in a vector for optimization)

for i = 1:length(angincrement);
    clear l;
    clear ht;

    incang = degtorad(angincrement(i));
    radtodeg(incang);

    % Intensity based

    att = -0.015; %per cm for clear glass

    % transforms

    I_o = 36;
    Io = I_o*cos(incang); %direct irradiance for UVA/B
    Iovec(i) = Io;

    ang = asin((snair/snmed)*sin(incang));
    radtodeg(ang);

    % Fresenel Equations:
    % percent transmitted to ti02 for s and p polarizations

    anginc = pi/2 - ang;   %transform 90 degrees
    radtodeg(anginc);

    angti02 = asin((snmed/snti02)*sin(anginc));   %get angle
```

```
transmitted to ti02
    radtodeg(angti02);

    Rs = (abs((snmed*cos(anginc) -
snti02*cos(angti02))/(snmed*cos(anginc) + snti02*cos(angti02))))^2;

    Rp = (abs((snmed*cos(angti02) -
snti02*cos(anginc))/(snmed*cos(angti02) + snti02*cos(anginc))))^2;

    R = (Rs+Rp)/2;
    Rvec(i) = R;
    % T = 1-R;

    % So, based on my understanding of the Fresnel equations, there
isn't going
    % to be much light regardless after one or two bounces.  Still, why
not
    % proceed?

    count = 1;
    w = 1;       %diameter of cylinder;

    % initialization
    l(count) = 0;
    ht(count) = 0;
    I(count) = Io;

    tol = 0.01; % 1% of initial radiance

    advl = cos(ang); % advance vectors
    advh = -sin(ang);

    while I(count) >= tol*Io;

        % outer loop for single pass through bounces of light for a
given width
        % are in Intensity, where once the intensity is below a certain
amount, the
        % loop terminates

        % next is the series of steps that flip the beam as it bounces
down the
        % cylinder.  I am wanting to do this with 'flip' counters, that
is, using
        % 'flip' as a measure of state for the light beam.  Technically
I could
        % code this into a single loop, using something to change the
flip command
        % and a multiple to the adv variable of something like adv =
        % [cos(ang),(-1^flip)*sin(ang)] as a kind of unit vector which
describes
        % the direction of the beam.  actually, i think I am going to
do this.  And
        % also incorporate this inside the height check loop
```

```
        t = 0.1;          % advance unit
        % htol = 1;         % ht tolerance for iterations

        while ht(count) >= -1*w/2 && t >=1e-4; %flip exponent on w goes
here for single loop

            l(count+1) = l(count)+t*advl;
            ht(count+1) = ht(count)+t*advh;
            tcheck(count) = t;

            %if abs(w/2 - ht(count+1)) >=0;     %flip
            if abs(w/2-ht(count+1)) <= 1e-4; %flip
                break
            end
            t = t;    % this is a catch sequence for if the inital
length is somehow very close to w/2
            %end

            if abs(ht(count+1)) > w/2
                t = 0.1*t;
                l(count+1) = l(count)+t*advl;
                ht(count+1) = ht(count)+t*advh;
            end
            cntchk(count) = count;
            I(count+1) = I(count)*exp(att*t);

            if I(count+1) <= tol*Io
                fake = 1;
                if length(l) > length(I)
                    I(count+1) = 0;
                end
                break
            end

            %htol = abs(abs(ht(count+1))-w/2);

            count = count+1;

        end

        if (w/2) - abs(ht(count)) < w/10;
            I(count) = R*I(count);
        end

        if I(count) <= tol*Io

            I(length(l))=0;
%             if length(l) > length(I)
%                 I(length(l)) = 0;
%             end

            break
        end
```

```
        t = 0.1;

        while ht(count) <= w/2 && t >=1e-4; %flip exponent on w goes
here for single loop


            l(count+1) = l(count)+t*advl;
            ht(count+1) = ht(count)-t*advh;
            tcheck(count) = t;

            %if abs(w/2 - ht(count+1)) >=0;     %flip
            if abs(w/2-abs(ht(count+1))) <= 1e-4; %flip
                break
            end
            t = t;    % this is a catch sequence for if the inital
length is somehow very close to w/2
            %end

            if abs(ht(count+1)) > w/2
                t = 0.1*t;
                l(count+1) = l(count)+t*advl;
                ht(count+1) = ht(count)-t*advh;
            end

            cntchk(count) = count;

            %update I
            I(count+1) = I(count)*exp(att*t);

            %I check
            if I(count+1) <= tol*Io
                fake = 3;
                if length(l) > length(I)
                    I(count+1) = 0;
                end
                break
            end

            %update count
            count = count+1;

        end

        % I check
        if I(count) <= tol*Io
            fake = 4;
            if length(l) > length(I)
                I(count+1) = 0;
            end
            break
        end

        % update I if at edge
        if (w/2) - abs(ht(count)) < w/10;
            I(count) = R*I(count);
        end
```

```
        if l(count)>100;
            break
        end

    end


    slenderness(i) = w/l(count);

    % draw the cylinder and incoming ray

    xup = [0,l(count)];
    yup = [w/2,w/2];
    xdown = [0,l(count)];
    ydown = [-w/2,-w/2];
    xray = [-cos(incang),0];
    yray = [sin(incang),0];
    xend = [0,0];
    yend = [w/2,-w/2];

    % plot raytrace

    figure
    plot(l,ht,'LineWidth',2.5)
    hold
    plot(xup,yup,'k')
    plot(xdown,ydown,'k')

    plot(xray,yray,'r','LineWidth',2.5)
    plot(xend,yend,'k')
    axis equal
    xlabel('Length in diameters')
    ylabel('Unit diameter')
    title('Slenderness study for 45 degree incident angle')
    ylim([-0.75 0.75]) % this is for the image used in the paper, can
remove later for loop
    xlim([-0.7 4.7])


    for i = 1:length(l);
        l15(i) = l(i)*(3);
    end

    tpcylI = [100 47 12 5 1.2 0.02];
    tpl = [0 3 6 9 12 15];

    ex=-0.3;
    for e = 1:16;
        tple(e) = e-1;
        tpcylIe(e) = 100*exp(ex*tple(e));
    end

    figure
    plot(l15,100*I/Io,'LineWidth',2.5)
```

```
    hold
    plot(tple,tpcylIe,'g','LineWidth',2.5)
    xlabel('length in millimeters')
    ylabel('% Initial irradiance in glass cylinder')
    legend('Parallel plate ray trace','Cylinder ray
trace','Location','NorthEast')
    title('Ray trace studies for light remaining in glass cylinder')

    clear I
  %  plot intensity as a function of length


end


% figure
% plot(angincrement,1-Rvec)
% title('Transmittance by angle of incidence')
% xlabel('Angle of incidence')
% ylabel('Transmittance')
%
% figure
% plot(angincrement,slenderness)
% title('Optimal Slenderness by angle of incidence')
% xlabel('Angle of incidence')
% ylabel('slenderness')
```

A.2 – Transform of cylinder coordinates to cartesian from Chapter II

```
%% recovery of streamline from COMSOL cyinder plot for transform into
cartesian coordinates from cylindrical

% This is a program to take the plot lines from comsol and transform
them
% into a meaningful form for a boundary layer analysis.

% I will bring in a data set from a streamline plot in COMSOL and
% manipulate it in order to fit a dimensionless curve to it and proceed
% from thence.

%length of data set

n = length(ytest);

%radius of cylinder (1cm diam.)
r = 0.005;

%loop to adjust coordinates and scale
% for i = 1:n;
%     count(i) = i;
%     ytest1(i) = -ytest(i);
%     %xtest1(i) = xtest(i);
% end

% minx = min(xtest)

for i = 1:n;
    yprime(i) = sqrt(ytest(i)^2 + xtest(i)^2) - r;
    xprime(i) = r * atan(xtest(i)/-ytest(i));

end

for i = 3:n;
    if yprime(i) == min(yprime)

        mindepth = yprime(i)

        theta = radtodeg(xprime(i)/r)

        break
    end
end

% NOTE: This study is very specific to the studies done in COMSOL.

% The script is set up to work with an element that gives data
beginning
% with a negative number, and ending in zero (for x coordinate
geometric
% dimensions).  Also, there is a division by 100 on the min depth test,
and
% there is absolutely no reason for this (an artifact of previous
```

```
code!).

% the efficiency is given by the volume flow inside the critical
streamline
% over the volume of the flow over one cylinder width (which is equal
to
% Uavg*d = 1cm/s*1cm = 10^-4 m^2/s) in this case we are simply removing
the
% multiplication by l from both, and thus find the efficiency
numerically.
% It is worth noting that the streamline velocity near to the center of
the
% entrance for

% eta = (mindepth*0.01) / (r*uavg)

% calculated efficiency from Friedlander for stand alone cylinder in
% potential flow is 0.7892*(Re^(1/2))*R^2, where R is 1e-4 in this
case.

% parameter for geometry change
% m = 1.15;
% uavg = 0.005*(m/(m-0.5))
% % solid fraction
% sf = (pi*(r^2)/2)/(m^2*0.01*sqrt(3)*0.01);
% % uatstrm = 0.0254;
% umax = uavg*(m/(m - 0.5))
% Re = 2*r*umax*1e6
% R = 1e-4;
% etaf = 0.7892*(Re^(1/2))*R^2

%%Plotting

% figure
%
% plot(xprime,yprime)
% figure
%
% plot(xtest,-ytest)
% axis equal
% axis ([-1e-4 6e-3 0 15e-3])
```

A.3 – GA code from Chapter IV

```
%% GA Transfer Simulation for CORE

%% gamultiobj for removal/ heat output paretofront
% The two objectives in this program are designed to compete with each
% other

%% Initial notes:

%% Section 0

% Initial definitions

% start timer
tic

%% Section 0.1: Tamb(t) for each day of interest

% the ambient temperature is defined from eight year averages in order
to
% assess heat loss at each ten minute interval

%% Section 0.2 definition of Ttot

% Ttot describes the transmission-absorption value (ta) for this panel
% for all incident angles.  I have not included the physical details.
In
% short, this uses the fresnel equations and snell's law to determine
the
% amount of light that is transmitted to the interior of the panel from
% incident light across all the material layers.

% NOTE: see transabs_pmma_nogap.m for all details here.

th = 0.3;
ag = 0.36;
n1 = 1.0;
n2 = 1.49;
n3 = 1.52;

for zz = 1:90;
    zz=round(zz);
    thetai(zz) = degtorad(zz-1);
    thetag(zz) = asin(sin(thetai(zz))*n1/n2);
    rperpg(zz) = (abs( ( (n1 * cos(thetai(zz))) - (n2 *
cos(thetag(zz))) ) / ( (n1 * cos(thetai(zz))) + (n2 * cos(thetag(zz)))
) ) )^2;
    rparg(zz) =  (abs( ((n1 * cos(thetag(zz))) - (n2 *
cos(thetai(zz)))) / ( (n1 * cos(thetag(zz))) + (n2 * cos(thetai(zz))) )
))^2;
    Rg(zz) = (rparg(zz)+rperpg(zz))/2;
    Tg(zz) = 1-Rg(zz);
    lg(zz) = th/cos(thetag(zz));
```

```
    loss(zz) = exp(-lg(zz)*ag);
end

for y = 1:length(thetag);
    thetaw(y) = asin(sin(thetag(y))*n2/n3);
    rperpw(y) = (abs( ( (n2 * cos(thetag(y))) - (n3 * cos(thetaw(y))) )
/ ( (n2*cos(thetag(y))) + (n3*cos(thetaw(y))) ) ) )^2;
    rparw(y) =  (abs( ((n2*cos(thetaw(y))) - (n3*cos(thetag(y)))) / (
(n2*cos(thetaw(y))) + (n3*cos(thetag(y))) ) ))^2;
    %reflected
    Rw(y) = (rparw(y)+rperpw(y))/2;
    %transmitted
    Tw(y) = 1-Rw(y);
end

for m = 1:length(thetai);
    Ttot(m) = Tw(m)*loss(m)*Tg(m);
end


Sd = 100; %W/m^2, diffuse irradiance


%% Section 1: definition of parameters for gamultiobj

% x(1) = tilt of panel
% x(2) = cylinder diameter (m)
% x(3) = panel depth

lb = [1, 0.005, 0.02];
ub = [89, 0.015, 0.1];
% lower and upper bounds on design variables,

fun = @(x)objval(x, Ttot);  %calling the objective function evaluation
function

%% Section 1.1: paretosearch

npts = 100;
opts_ps.ParetoSetSize = 2*npts;
opts.ps.MaxFunctionEvaluations = 10000;
%options for paretosearch
opts_ps =
optimoptions('paretosearch','Display','off','PlotFcn','psplotparetof');

% definition of contstraints and number of variables
A = []; b = [];
Aeq = []; beq = [];
numberOfVariables = 3;

% function paretosearch call.

% Note: calls 'fun' as one of the variables it passes
[x_ps,fval_ps,exitflag,psoutput1] =
paretosearch(fun,numberOfVariables,A,b,Aeq,beq,lb,ub,[],opts_ps);
```

```
disp("NSGA-II Total Paretosearch Function Count: " +
psoutput1.funccount);

% %
% % find optimal points to start pareto solution
% x0 = zeros(2,3);
% x0f = (lb + ub)/2;
% opts_fmc =
optimoptions('fmincon','Display','off','MaxFunctionEvaluations',1e4);
% x0(1,:) =
fmincon(@(x)pickindex(x,1,Ttot),x0f,[],[],[],[],lb,ub,[],opts_fmc);
% x0(2,:) =
fmincon(@(x)pickindex(x,2,Ttot),x0f,[],[],[],[],lb,ub,[],opts_fmc);
%
% opts_ps.InitialPoints = x0;
% opts_ps.PlotFcn = [];
% [x_psx0,fval_ps1x0,exitflag,psoutput1x0] =
paretosearch(fun,numberOfVariables,A,b,Aeq,beq,lb,ub,[],opts_ps);
% disp("Total Initial Opt pt. Paretosearch Function Count: " +
psoutput1x0.funccount);
%
%
%
% Fmax = max(fval_ps1x0);
% nobj = numel(Fmax);
% Fmin = min(fval_ps1x0);
% w = sum((Fmax - fval_ps1x0)./(1 + Fmax - Fmin),2);
% p = w.*((Fmax - fval_ps1x0)./(1 + Fmax - Fmin));
% xnew = zeros(size(x_psx0));
% nsol = size(xnew,1);
% fvalnew = zeros(nsol,nobj);
% opts_fg = optimoptions('fgoalattain','Display','off');
% nfv = 0;
% for ii = 1:nsol
%     [xnew(ii,:),fvalnew(ii,:),~,~,output] =
fgoalattain(fun,x_psx0(ii,:),fval_ps1x0(ii,:),p(ii,:),...
%         A,b,[],[],lb,ub,[],opts_fg);
%     nfv = nfv + output.funcCount;
% end
% disp("fgoalattain Function Count: " + nfv)


% Plotting solution
figure

[fps, indexp] = sortrows(fval_ps,1,'ascend');
plot(fps(:,1),fps(:,2),'k-')

%hold on

% fps2 = sortrows(fval_ps1x0,1,'ascend');
% plot(fps2(:,1),fps2(:,2),'r-')
%
% % %xlim([0 40])
% % %ylim([0 1e-2])
% %
```

```
% [fps3,indexp] = sortrows(fvalnew,1,'ascend');
% plot(fps3(:,1),fps3(:,2),'k.-')

% hold on
% plot(fps(1,1),fps(1,2),'go','Linewidth',2)
% plot(fps(2,1),fps(2,2),'ro','Linewidth',2)
% plot(fps(24,1),fps(24,2),'bo','Linewidth',2)
%plot(fps(12,1),fps(12,2),'co','Linewidth',2)


%legend('paretofront, 100 inital pts.','x = 51 deg, 0.5cm, 0.03m','x =
62 deg, 1.5cm, 0.052m','x = 61 deg, 1.5cm, 0.054m');%,'x = 45 deg,
1.5cm, 0.077m','Location','southwest')
%'fpval_ps','fval_ps1x0','fvalnew')%,'x = 72 deg, 0.5cm, 0.1m','x = 26
deg, 0.5cm, 0.1m','x = 36 deg, 1.1cm, 0.1m')
%'paretoserach w/inital pts', 'paretosearch w/hybrid')

%xlim([-12 -7])
%ylim(1e7*[-2.2 -1.65])

xlabel('Averaged Quantum efficiency (f1)')
ylabel('Averaged Thermal Efficiency (f2)')
title('Efficiency paretofront for CORE panel, evacuation in all
seasons','Fontsize',15)
%title ('Basic NSGA-II algorithm for CORE output')

toc;
time = toc

%% function pick index for inital optimal points
function z = pickindex(x,k,Ttot)
z = objval(x, Ttot); % evaluate both objectives
z = z(k); % return objective k
end


%% Section 2: objective function defintion

function F = objval(x, Ttot)
% here I pass Ttot along with x into the evaluation of the objective
% functions

%% Section 2.1: Panel physical parameters

rhow = 10^3; % density of H20, kg/m^3
rhog = 2.5*10^3; %density of glass, kg/m^3
Vflow = 0.015; % velocity of flow in panel, m/sec
Qflow = Vflow*x(3); % flow rate in panel, m^3/sec this is equivalent to
40L/min
% x(3) is panel depth

% diameter of cylinder range is 0.5 to 1.5

ff = ( ( sqrt(3) - 0.5*pi*((100*x(2))/2)^2 )  /sqrt(3) );   % fluid
fraction in panel
```

```
% x(2) is diameter of cylinders in panel
sf = 1-ff; %solid fraction in panel
Vpanel = ff*x(3);  % fluid volume in panel, m^3
Vres = x(3); % Vol. reservoir, m^3
Vtot = Vpanel+Vres; %Vol. panel m^3

MH20 = rhow*Vtot; % total mass of water

cpH20 = 4186; %specific heat of water, J/kg*C
cpg = 1000; %specific heat of glass, J/kg*C
cptot =  (cpH20*x(3) + x(3)*(ff*cpH20 + sf*cpg) ) / (x(3)+x(3));
%change cpH20*X depending on reservoir depth
% x(3) is the panel depth in the above line

Mtot = ff*x(3)*rhow + sf*x(3)*rhog + Vres*rhow; %total mass, kg

HRTpan = Vpanel/Qflow; % hydraulic residence time in panel, seconds

% transfer parameters

%cylinder relations
lcyl = x(3); %m
dcyl = x(2); %m
rcyl = dcyl/2; %m
Areacyl = pi*lcyl*dcyl; %m^2
cell_length = dcyl*sqrt(3);%m
numcyl = 1/cell_length;
Umaxavg = Vflow * (0.02/(0.02-dcyl)); % m/s, dcyl is x(2)

Dmb = 3*10^-10; %diffusion of MB in H20

numft = 10*HRTpan; %number of flow throughs of panel in study time
increment of ten minutes

%% Section 2.2 Solar data to incident angle on panel surface

% In this section I use solar data (elevation, azimuth at 10 minute
intervals)
% for a location on a specific day to genrate a vector of incident
angles
% on a panel surface.

% these functions are called inside the objective function evaluation
% becuase tilt of the panel is one of the variables I am investigating
in
% the optimization (x(1)).

elez = zeros;
aziz = zeros;
[ele,azi] = solardata1(elez,aziz);
% ele = elevation azi = azimuth

% length of data vector
n = length(ele);
```

```
% n= length(ele) count of solar data vector (section
% angle in degrees offset from due south of panel along azimuth
direction
% positive past south in the west direciton, neg otherwise
delta = 0; %  ==> panel is facing due South

[alpha,gamma] = solardatatovector1(ele,azi,n,delta);
%alpha and gamma are used to define theta in the next function

sigma = degtorad(x(1));
% sigma is the angle of tilt to the horizontal plane

[theta] = panelincidentangle1(alpha,gamma,n,sigma);
% theta is the incident angle of beam irradiance to the panel surface
for each time

n = length(theta);
%resize to theta

nor = 180/n; % this is what divides the number of segments and
equalizes them
% in order to make a vector that matches thetai and still goes over the
sin
% function of a days temp fluctuation

low = 10; % avg of spring and fall for both low and high here
high = 20.5;
for h = 1:n
    t(h) = (h-1) * 10;
    Tambeq(h) = 273.15+low +  ( (high-low) * sin(0.95 * degtorad(nor *
h-1)) );
    % this is in K
end


%% Section 2.3: Source values at specific times

% Source is calculated every 10 minutes, coincident with theta from
'solar in
% theta'
%l = 72; %length(elez); % define this from a vector of solar values

Sd = 100; %W/m^2, diffuse irradiance

% this loop finds the beam irradiance on the panel face at each time t
% from the solar data
for i = 1:n;
    ang = (round(radtodeg(theta(i))));%getting a count number
    if ang <= 0;
        ang = 1;
    elseif abs(ang)>=90;
        ta = 0;
    else
        ta = Ttot(ang); % (defined in 0.2)
    end
    G(i) = 1000*cos(theta(i)) + Sd;
```

```
    Sb(i) = 1000*cos(theta(i))*ta; %Sbeam(i) = full insolation *
cos(theta(i)
    % * transabs for given angle Ttot(ang)
    Stot(i) = Sd+Sb(i);
end

%% Section 2.4: fraction of irradiance due to incidence in cylinders

% Angle relations for removal

% this section relates the angle of the incident radiation on the panel
% to the angle in the cylinder to determine the fraction of cylinder
% surface area illuminated

%fraction of cylinder active in CORE experiment
thetaexpc = degtorad(90) - asin( (1/1.5)*sin(degtorad(45)));

Aexp = (0.015*pi*0.003);
Acylexp = ( 2*0.0015^2/cot(thetaexpc) ) ;  %fraction of active area in
experiment
Afracexp = Acylexp / Aexp ;  %fraction of active area in experiment

AcylC = pi*dcyl*lcyl; %Area of cylinder in GA
for i = 1:n
    %angle in glass cylinder
    thetagl(i) = asin( 1/1.5 * sin(theta(i)) );
    Acyl(i) = (2 * (rcyl)^2) / cot(1.5708 - thetagl(i));
    if Acyl(i) > AcylC/2;

        Acyl(i) = AcylC/2 ;

    end
    Afrac(i) = Acyl(i)/(AcylC);
    Acyltot(i) = Afrac(i)/Afracexp * AcylC/Aexp;
    Atot(i) = numcyl*Acyl(i);
end
Icylexp = sin(degtorad(45))*750*Ttot(45)*(pi/2)*cot(thetaexpc);
Iexp = sin(degtorad(45))*750*Ttot(45);
I_o = 1000; % W/m^2
Ifrad = 0.1172; %I fraction for diffuse radiation
for i = 1:n-1;
    ang = (round(radtodeg(theta(i))));%getting a count number
    if ang <= 0;
        ang = 1;
    elseif abs(ang)>=90;
        ta = 0;
    else
        ta = Ttot(ang); % (defined in 0.2)
    end
    Ifracb(i) = I_o * ta * ( cos(theta(i) ) * cot(1.5708-thetagl(i)) )
* (pi/2) / Icylexp;

    % this is the beam factor I calcualted from basics in the notebook,
see pg. 21
    Ifracph(i) = ( (I_o*cos(theta(i))*ta)+100 )/Iexp;
    % this is the irradiance acting in photolysis based on experiments,
```

```
its
    % the diffuse component is added in directly here (+100)
end



%% Section 2.5: Losses in panel

hconv = 5.5; % W/m*K, external convection, wind speed across panel is 2
m/s

eps = 0.9;
sig = 5.67*10^-8;
k = 0.045; %conduction coeff across insulation on back
L = 0.05; %depth of insulation, m

if x(1) <= 10;

    Ub = 0.0045/L;
    Ue = 0;

else

    Ub = k/L + 1/5.5;  % losses due to conduction and convection out
the back
    Ue = Ub*0.6/1; % edge loss

end

U = Ub+Ue; % combined edge and back loss coeff

%% Section 2.6: Heat Study

Utot_o = U+hconv; % inital loss coeffieicnt
Quo = (Stot(1)+Stot(2))/2;
delTo = Quo*600/(cptot*Mtot); %seconds to 10 minute time intervals
T(1) = Tambeq(1)+delTo;

% removal via reservoir mass balance consts and inits
Ctot(1) = 1;
% photolysis
kphconst = 0.00067;

count = 0;

%initialize output objective functions
Vremtot = 0;
Egaintot = 0;
ice = 0;

Vrem = 0;

effrem = zeros(1,n);
effheat = zeros(1,n);
effremtot = 0;
```

```
effheattot = 0;

for i = 1:n-1;
    %inital pass for temp gain
    hrad_o = eps * sig * (T(i)^2 + Tambeq(i)^2) * (T(i) + Tambeq(i));
    Ut_o = hconv + hrad_o; %loss on front of panel
    Utot_o = Ut_o + U;

    Qu_o = ((Stot(i) + Stot(i+1))/2) - Utot_o * (T(i)-Tambeq(i)) ;
    delT_o = Qu_o*600/(cptot*Mtot);
    T_o = T(i)+delT_o;
    Tavg(i) = (T_o+T(i))/2;

    %iteration for more accurate radiation coeff
    hrad(i) = eps * sig * (Tavg(i)^2 + Tambeq(i)^2) * (Tavg(i) +
Tambeq(i));
    Ut(i) = hconv + hrad(i);
    Utot(i) = Ut(i) + U;
    Qu(i) = ((Stot(i)+Stot(i+1))/2) - (Utot(i) * (T(i)-Tambeq(i)) );
    delT(i) = Qu(i)*600/(cptot*Mtot);
    T(i+1) = T(i)+delT(i);

    % begin removal study
    mu = 2.414 * (10^-5) * 10 ^ (247.8 / (T(i)-140) );
    Re = rhow*Umaxavg*dcyl/mu;
    Sc = mu/(rhow*Dmb);
    muv(i) = mu;
    Rev(i) = Re;
    Sci(i) = Sc;

    % removal via reservoir mass balance

    E_act = 11000;
    R_gas = 8.3145;
    T_1 = 293;

    k_init = 10^-4 * (0.012*Rev(i) + 3.96);
    k_o = k_init/(exp(-(E_act/(R_gas*T_1))));

    k_new = k_o*exp(-(E_act/(R_gas*T(i))));
    %kfrac(i) = (k_new/k_init);

    % scaling relations from experimental removal to CORE reactor
numerical

    kvb(i) = k_new * numcyl^2/48 * ( Acyltot(i) )* Ifracb(i) *
(0.25/(Vtot*1000));
    kvd(i) = k_new * numcyl^2/48 * ( AcylC/Aexp )* (100/Icylexp) *
(0.25/(Vtot*1000));

    kph(i) = Ifracph(i)*kphconst;
    %kphd & kphb combined above

    ktot = kph(i)+kvb(i)+kvd(i); % k total at time step i
    ktot = ktot * (1 + ((0.83/50) * (T(i)-273)) );
```

```
    Ctot(i+1) = Ctot(i)*exp(-ktot*10);

    %          %Efficiency vectors: for efficiency objective functions
    effrem(i+1) = (Vtot/Atot(i+1)) * ktot / ((G(i+1)+G(i))/2);
    effheat(i+1) = (  delT(i)  )*(cptot*Mtot) / (( (G(i+1)+G(i))/2) *
600 );
    if effheat(i+1) > 1;
        effheat(i+1) = 1;
    end

    %This section for Volume vs. Heat gain total objective functions
    if Ctot(i+1)<=10^-3 | (T(i+1)-273) >= 55;
        Ctot(i+1) = 1;
        Vremtot = Vremtot + Vtot;
        Egaintot = (T(i+1)-Tambeq(i))*(cptot*Mtot) + Egaintot;
        T(i+1) = Tambeq(i+1);
        count = count+1;
    else
        continue
    end
    %

end

% Output objective functions
%Vremtot = Vremtot;% + (1-Ctot(n))*Vtot;
Egaintot = Egaintot + (T(n)-Tambeq(n))*(cptot*Mtot);

%

% % test for clearing one batch

if Vremtot <= 0.999*Vtot;
    Vremtot = 0;
    Egaintot = Egaintot;
    ice = 1;

    %     effremtot=0;
    %     effheattot=0;

end

Vrem = 2*Vremtot;
Etot = 2*Egaintot;

effremtot = 2 * (sum(effrem)/(n));
effheattot = 2 * (sum(effheat)/(n));


clear theta;
clear ele;
clear azi;
clear Ifracb;
clear Ifracph;
clear thetagl;
clear Acyl;
```

```
clear Afrac;
clear Acyltot;
clear Atot;
clear Sb;
clear Stot;
clear t;
clear Tambeq;
clear T;
clear Tavg;
clear hrad;
clear Ut;
clear Utot;
clear Qu;
clear delT;
clear muv;
clear Rev;
clear Sci;
clear kvb;
clear kvd;
clear kph;
clear Ctot;
clear Vremtot;
clear effrem;
clear Egaintot;
clear effheat;
clear G;
%% repeat for winter

elez = zeros;
aziz = zeros;
[ele,azi] = solardataw(elez,aziz);
% ele = elevation azi = azimuth

% length of data vector
n = length(ele);

delta = 0; %  ==> panel is facing due South

[alpha,gamma] = solardatatovector1(ele,azi,n,delta);
%alpha and gamma are used to define theta in the next function

sigma = degtorad(x(1));
% sigma is the angle of tilt to the horizontal plane

[theta] = panelincidentangle1(alpha,gamma,n,sigma);
% theta is the incident angle of beam irradiance to the panel surface
for each time

n = length(theta);

nor = 180/n;

low = 8.5; % avg of spring and fall for both low and high here
high = 15.5;
for h = 1:n
    t(h) = (h-1) * 10;
```

```
    Tambeq(h) = 273.15+low +  ( (high-low) * sin(0.95 * degtorad(nor *
h-1)) );
    % this is in K
end

%% source
for i = 1:n;
    ang = (round(radtodeg(theta(i))));%getting a count number
    if ang <= 0;
        ang = 1;
    elseif abs(ang)>=90;
        ta = 0;
    else
        ta = Ttot(ang); % (defined in 0.2)
    end
    G(i) = 1000*cos(theta(i)) + Sd;
    Sb(i) = 1000*cos(theta(i))*ta; %Sbeam(i) = full insolation *
cos(theta(i)
    % * transabs for given angle Ttot(ang)
    Stot(i) = Sd+Sb(i);
end

%% angle and Ifraction
for i = 1:n
    %angle in glass cylinder
    thetagl(i) = asin( 1/1.5 * sin(theta(i)) );
    Acyl(i) = (2 * (rcyl)^2) / cot(1.5708 - thetagl(i));
    if Acyl(i) > AcylC/2;

        Acyl(i) = AcylC/2 ;

    end
    Afrac(i) = Acyl(i)/(AcylC);
    Acyltot(i) = Afrac(i)/Afracexp * AcylC/Aexp;
    Atot(i) = numcyl*Acyl(i);
end

for i = 1:n;
    ang = (round(radtodeg(theta(i))));%getting a count number
    if ang <= 0;
        ang = 1;
    elseif abs(ang)>=90;
        ta = 0;
    else
        ta = Ttot(ang); % (defined in 0.2)
    end
    Ifracb(i) = I_o * ta * ( cos(theta(i) ) * cot(1.5708-thetagl(i)) )
* (pi/2) / Icylexp;

    % this is the beam factor I calcualted from basics in the notebook,
see pg. 21
    Ifracph(i) = ( (I_o*cos(theta(i))*ta)+100 )/Iexp;
    % this is the irradiance acting in photolysis based on experiments,
its
    % the diffuse component is added in directly here (+100)
end
```

```
Utot_o = U+hconv; % inital loss coeffieicnt
Quo = (Stot(1)+Stot(2))/2;
delTo = Quo*600/(cptot*Mtot); %seconds to 10 minute time intervals
T(1) = Tambeq(1)+delTo;

% removal via reservoir mass balance consts and inits
Ctot(1) = 1;

%initialize output objective functions
Vremtot = 0;
Egaintot = 0;

effrem = zeros(1,n);
effheat = zeros(1,n);

count = 0;

for i = 1:n-1;
    %inital pass for temp gain
    hrad_o = eps * sig * (T(i)^2 + Tambeq(i)^2) * (T(i) + Tambeq(i));
    Ut_o = hconv + hrad_o; %loss on front of panel
    Utot_o = Ut_o + U;

    Qu_o = ((Stot(i)+Stot(i+1))/2) - Utot_o * (T(i)-Tambeq(i)) ;
    delT_o = Qu_o*600/(cptot*Mtot);
    T_o = T(i)+delT_o;
    Tavg(i) = (T_o+T(i))/2;

    %iteration for more accurate radiation coeff
    hrad(i) = eps * sig * (Tavg(i)^2 + Tambeq(i)^2) * (Tavg(i) +
Tambeq(i));
    Ut(i) = hconv + hrad(i);
    Utot(i) = Ut(i) + U;
    Qu(i) = ((Stot(i)+Stot(i+1))/2) - (Utot(i) * (T(i)-Tambeq(i)) );
    delT(i) = Qu(i)*600/(cptot*Mtot);
    T(i+1) = T(i)+delT(i);

    % begin removal study
    mu = 2.414 * (10^-5) * 10 ^ (247.8 / (T(i)-140) );
    Re = rhow*Umaxavg*dcyl/mu;
    Sc = mu/(rhow*Dmb);
    muv(i) = mu;
    Rev(i) = Re;
    Sci(i) = Sc;
    % removal via reservoir mass balance

    E_act = 11000;
    R_gas = 8.3145;
    T_1 = 293;

    k_init = 10^-4 * (0.012*Rev(i) + 3.96);
    k_o = k_init/(exp(-(E_act/(R_gas*T_1))));

    k_new = k_o*exp(-(E_act/(R_gas*T(i))));
    %kfrac(i) = (k_new/k_init);
```

```
    % scaling relations from experimental removal to CORE reactor
numerical

    kvb(i) = k_new * numcyl^2/48 * ( Acyltot(i) )* Ifracb(i) *
(0.25/(Vtot*1000));
    kvd(i) = k_new * numcyl^2/48 * ( AcylC/Aexp )* (100/Icylexp) *
(0.25/(Vtot*1000));

    kph(i) = Ifracph(i)*kphconst;
    %kphd & kphb combined above

    ktot = kph(i)+kvb(i)+kvd(i); % k total at time step i
    ktot = ktot * (1 + ((0.83/50) * (T(i)-273)) ); %synergy

    Ctot(i+1) = Ctot(i)*exp(-ktot*10);

     %          %Efficiency vectors: for efficiency objective functions
    effrem(i+1) = (Vtot/Atot(i+1)) * ktot / ((G(i+1)+G(i))/2);
    effheat(i+1) = ( delT(i) )*(cptot*Mtot)/( ((G(i+1)+G(i))/2) *600 );
    if effheat(i+1) > 1;
        effheat(i+1) = 1;
    end


    %This section for Volume vs. Heat gain total objective functions
    if Ctot(i+1)<=10^-3 | (T(i+1)-273) >= 55;
        Ctot(i+1) = 1;
        Vremtot = Vremtot + Vtot;
        Egaintot = (T(i+1)-Tambeq(i))*(cptot*Mtot) + Egaintot;
        T(i+1) = Tambeq(i+1);
        count = count+1;
    else
        continue
    end
    %

    %
end

Vremtot = Vremtot;% + (1-Ctot(n))*Vtot;
Egaintot = Egaintot + (T(n)-Tambeq(n))*(cptot*Mtot);

% % test for clearing one batch

if Vremtot <= 0.999*Vtot;
    Vremtot = 0;
    Egaintot = Egaintot;
    ice = ice +1;

    %     effremtot=0;
    %     effheattot=0;
end

Vrem = Vrem + Vremtot;
Etot = Etot + Egaintot;
```

```
effremtot = effremtot + sum(effrem)/(n);
effheattot = effheattot + sum(effheat)/(n);

%% repeat for summer
clear theta;
clear ele;
clear azi;
clear Ifracb;
clear Ifracph;
clear thetagl;
clear Acyl;
clear Afrac;
clear Acyltot;
clear Atot;
clear Sb;
clear Stot;
clear t;
clear Tambeq;
clear T;
clear Tavg;
clear hrad;
clear Ut;
clear Utot;
clear Qu;
clear delT;
clear muv;
clear Rev;
clear Sci;
clear kvb;
clear kvd;
clear kph;
clear Ctot;
clear Vremtot;
clear effrem;
clear Egaintot;
clear effheat;
clear G;

elez = zeros;
aziz = zeros;
[ele,azi] = solardatas(elez,aziz);
% ele = elevation azi = azimuth

% length of data vector
n = length(ele);

% n= length(ele) count of solar data vector (section

% angle in degrees offset from due south of panel along azimuth
direction
% positive past south in the west direciton, neg otherwise
delta = 0; %  ==> panel is facing due South

[alpha,gamma] = solardatatovector1(ele,azi,n,delta);
%alpha and gamma are used to define theta in the next function
```

```
sigma = degtorad(x(1));
% sigma is the angle of tilt to the horizontal plane

[theta] = panelincidentangle1(alpha,gamma,n,sigma);
% theta is the incident angle of beam irradiance to the panel surface
for each time
n = length(theta);

nor = 180/n; % this is what divides the number of segments and
equalizes them
% in order to make a vector that matches thetai and still goes over the
sin
% function of a days temp fluctuation


% Ambient temp
low = 14.5; % avg of spring and fall for both low and high here
high = 23.5;
for h = 1:n
    t(h) = (h-1) * 10;
    Tambeq(h) = 273.15+low +  ( (high-low) * sin(0.95 * degtorad(nor *
h-1)) );
    % this is in K
end



% make incident angles greater than 90 = 90
for i = 1:n;
    if radtodeg(theta(i)) > 90;
        theta(i) = degtorad(90);
    end
end

%% source
for i = 1:n;
    ang = (round(radtodeg(theta(i))));%getting a count number

    if ang <= 0;
        ang = 1;
    elseif abs(ang)>=90;
        ta = 0;
    else
        ta = Ttot(ang); % (defined in 0.2)
    end

    G(i) = 1000*cos(theta(i)) + Sd;
    Sb(i) = 1000*cos(theta(i))*ta; %Sbeam(i) = full insolation *
cos(theta(i)
    % * transabs for given angle Ttot(ang)
    Stot(i) = Sd+Sb(i);
end

%% angle and Ifraction
for i = 1:n
    %angle in glass cylinder
```

```
    thetagl(i) = asin( 1/1.5 * sin(theta(i)) );
    Acyl(i) = (2 * (rcyl)^2) / cot(1.5708 - thetagl(i));
    if Acyl(i) > AcylC/2;

        Acyl(i) = AcylC/2 ;

    end
    Afrac(i) = Acyl(i)/(AcylC);
    Acyltot(i) = Afrac(i)/Afracexp * AcylC/Aexp;
    Atot(i) = numcyl*Acyl(i);
end

for i = 1:n;
    ang = (round(radtodeg(theta(i))));%getting a count number
    if ang <= 0;
        ang = 1;
    elseif abs(ang)>=90;
        ta = 0;
    else
        ta = Ttot(ang); % (defined in 0.2)
    end
    Ifracb(i) = I_o * ta * ( cos(theta(i) ) * cot(1.5708-thetagl(i)) )
* (pi/2) / Icylexp;

    % this is the beam factor I calcualted from basics in the notebook,
see pg. 21
    Ifracph(i) = ( (I_o*cos(theta(i))*ta)+100 )/Iexp;
    % this is the irradiance acting in photolysis based on experiments,
its
    % the diffuse component is added in directly here (+100)
end

Utot_o = U+hconv; % inital loss coeffieicnt
Quo = (Stot(1)+Stot(2))/2;
delTo = Quo*600/(cptot*Mtot); %seconds to 10 minute time intervals
T(1) = Tambeq(1)+delTo;

% removal via reservoir mass balance consts and inits
Ctot(1) = 1;

Vremtot = 0;
Egaintot = 0;
count = 0;

effrem = zeros(1,n);
effheat = zeros(1,n);

for i = 1:n-1;
    %inital pass for temp gain
    hrad_o = eps * sig * (T(i)^2 + Tambeq(i)^2) * (T(i) + Tambeq(i));
    Ut_o = hconv + hrad_o; %loss on front of panel
    Utot_o = Ut_o + U;

    Qu_o(1) = ((Stot(i)+Stot(i+1))/2) - Utot_o * (T(i)-Tambeq(i)) ;
    delT_o = Qu_o*600/(cptot*Mtot);
    T_o = T(i)+delT_o;
```

```
    Tavg(i) = (T_o+T(i))/2;

    %iteration for more accurate radiation coeff
    hrad(i) = eps * sig * (Tavg(i)^2 + Tambeq(i)^2) * (Tavg(i) +
Tambeq(i));
    Ut(i) = hconv + hrad(i);
    Utot(i) = Ut(i) + U;
    Qu(i) = Stot(i+1) - (Utot(i) * (T(i)-Tambeq(i)) );
    delT(i) = Qu(i)*600/(cptot*Mtot);
    T(i+1) = T(i)+delT(i);

    % begin removal study
    mu = 2.414 * (10^-5) * 10 ^ (247.8 / (T(i)-140) );
    Re = rhow*Umaxavg*dcyl/mu;
    Sc = mu/(rhow*Dmb);
    muv(i) = mu;
    Rev(i) = Re;
    Sci(i) = Sc;
    % removal via reservoir mass balance

    %arrhenius rate considerations (do not know E_act iw/ certainty,
but it is
    %comparable to this value of 11000
    %from http://article.sapub.org/pdf/10.5923.j.ajee.20120201.01.pdf
    E_act = 11000;
    R_gas = 8.3145;
    T_1 = 293;

    k_init = 10^-4 * (0.012*Rev(i) + 3.96);
    k_o = k_init/(exp(-(E_act/(R_gas*T_1))));

    k_new = k_o*exp(-(E_act/(R_gas*T(i))));
    %kfrac(i) = (k_new/k_init);

    % scaling relations from experimental removal to CORE reactor
numerical

    kvb(i) = k_new * numcyl^2/48 * ( Acyltot(i) )* Ifracb(i) *
(0.25/(Vtot*1000));
    kvd(i) = k_new * numcyl^2/48 * ( AcylC/Aexp )* (100/Icylexp) *
(0.25/(Vtot*1000));

    kph(i) = Ifracph(i)*kphconst;
    %kphd & kphb combined above

    ktot = kph(i)+kvb(i)+kvd(i); % k total at time step i
    ktot = ktot * (1 + ((0.83/50) * (T(i)-273)) );

    Ctot(i+1) = Ctot(i)*exp(-ktot*10);

     %          %Efficiency vectors: for efficiency objective functions
    effrem(i+1) = (Vtot/Atot(i+1)) * ktot / ( (G(i+1)+G(i))/2 );
    effheat(i+1) = ( delT(i) )*(cptot*Mtot)/( ((G(i+1)+G(i))/2) *600 );
    if effheat(i+1) > 1;
        effheat(i+1) = 1;
    end
```

```
    %This section for Volume vs. Heat gain total objective functions
    if Ctot(i+1)<=10^-3 | (T(i+1)-273) >= 55;
        Ctot(i+1) = 1;
        Vremtot = Vremtot + Vtot;
        Egaintot = (T(i+1)-Tambeq(i))*(cptot*Mtot) + Egaintot;
        T(i+1) = Tambeq(i+1);
        count = count+1;
    else
        continue
    end
    %
    %
end

Vremtot = Vremtot;% + (1-Ctot(n))*Vtot;
Egaintot = Egaintot + (T(n)-Tambeq(n))*(cptot*Mtot);

% % test for clearing one batch

if Vremtot <= 0.999*Vtot;
    Vremtot = 0;
    Egaintot = Egaintot;
    ice = ice +1;

    %     effremtot=0;
    %     effheattot=0;
end

Vrem = Vrem + Vremtot;
Etot = Etot + Egaintot;

Vrem = Vrem/4;
Etot = Etot/4;

effremtot = effremtot + sum(effrem)/(n);
effheattot = effheattot + sum(effheat)/(n);

effremfin = effremtot/4;
effheatfin = effheattot/4;

%% objective function evaluation


% F = [-effremfin, -effheatfin];
if ice > 2;
    F = [1 1];

%  if Vrem == 0;
%      F = [1 1];
else
    %F = [-Vrem, -Etot];
    F = [-effremfin, -effheatfin];
end
```

```
% if ice > 0;
%     F = [1 1];
% end


%
```

```
%% Functions within objval function

% functions for solar data, included inside objective function
evaluation
% because the tilt of the panel is one of the variables of interest
(x(1)).

%% solardata1
function [ele,azi] = solardata1(elez,aziz)

ele = [88.481535 86.627330 84.714515 82.778997 80.835253 78.890414
76.948801 75.013535 73.087201 71.172157 69.270691 67.385119 65.517845
63.671412 61.848540 60.052164 58.285466 56.551913 54.855290 53.199732
51.589761 50.030307 48.526742 47.084886 45.711014 44.411841 43.194480
42.066378 41.035206 40.108720 39.294568 38.600072 38.031964 37.596114
37.297267 37.138799 37.122543 37.248684 37.515749 37.920688 38.459041
39.125163 39.912486 40.813795 41.821488 42.927812 44.125058 45.405716
46.762586 48.188857 49.678148 51.224534 52.822541 54.467135 56.153704
57.878024 59.636231 61.424785 63.240439 65.080202 66.941305 68.821163
70.717341 72.627503 74.549360 76.480578 78.418645 80.360611 82.302546
84.238271 86.155905 88.027325 89.781947];

azi = [-89.903762 -88.369581 -86.830538 -85.282937 -83.723023 -
82.146950 -80.550760 -78.930358 -77.281482 -75.599682 -73.880288 -
72.118391 -70.308817 -68.446103 -66.524485 -64.537883 -62.479900 -
60.343830 -58.122688 -55.809250 -53.396140 -50.875934 -48.241322 -
45.485320 -42.601543 -39.584547 -36.430240 -33.136354 -29.702962 -
26.133004 -22.432769 -18.612285 -14.685513 -10.670312 -6.588082 -
2.463105 1.678416 5.809515 9.903710 13.936196 17.884855 21.730992
25.459756 29.060245 32.525358 35.851443 39.037830 42.086309 45.000604
47.785897 50.448395 52.994977 55.432901 57.769585 60.012430 62.168705
64.245457 66.249462 68.187190 70.064798 71.888125 73.662704 75.393777
77.086316 78.745048 80.374475 81.978905 83.562475 85.129176 86.682884
88.227377 89.766370 91.303529];

end

%% solardataw
function [ele,azi] = solardataw(elez,aziz)

ele = [89.0104   87.4663   85.8858   84.3067   82.7457   81.2115
79.7095   78.2439   76.8181   75.4353   74.0987   72.8112   71.5758
70.3957   69.2738   68.2132   67.2171   66.2885   65.4303   64.6455
```

```
63.9370   63.3073   62.7589   62.2940   61.9145   61.6221   61.4181
61.3032   61.2781   61.3428   61.4972   61.7404   62.0714   62.4887
62.9907   63.5753   64.2401   64.9826   65.8001   66.6897   67.6485
68.6735   69.7615   70.9095   72.1144   73.3731   74.6827   76.0400
77.4421   78.8859   80.3680   81.8848   83.4317   85.0021   86.5846
88.1557  89.6629];
azi = [ -59.2086  -57.6483  -56.0555  -54.4278  -52.7633  -51.0598  -
49.3152  -47.5276  -45.6953  -43.8166  -41.8899  -39.9141  -37.8880  -
35.8110  -33.6826  -31.5030  -29.2725  -26.9920  -24.6630  -22.2875  -
19.8681  -17.4079  -14.9106  -12.3806   -9.8226   -7.2419   -4.6442   -
2.0355    0.5782    3.1904    5.7950    8.3859   10.9573   13.5036
16.0198   18.5012   20.9438   23.3442   25.6995   28.0073   30.2659
32.4741   34.6311   36.7368   38.7913   40.7952   42.7492   44.6546
46.5127   48.3251   50.0935   51.8198   53.5059   55.1540   56.7660
58.3443   59.8910];

end

%% solardatas
function [ele,azi] = solardatas(elez,aziz)

ele = [  89.8573  88.3499   86.7177   85.0147   83.2671   81.4871
79.6809   77.8525   76.0045   74.1392   72.2582   70.3631   68.4551
66.5355   64.6056   62.6664   60.7192   58.7649   56.8048   54.8399
52.8715   50.9007   48.9290   46.9576   44.9882   43.0225   41.0624
39.1101   37.1682   35.2398   33.3284   31.4383   29.5749   27.7447
25.9559   24.2186   22.5460   20.9544   19.4647   18.1030   16.9010
15.8957   15.1268   14.6322   14.4402   14.5630   14.9928   15.7041
16.6607   17.8226   19.1520   20.6158   22.1869   23.8432   25.5674
27.3458   29.1677   31.0244   32.9091   34.8162   36.7413   38.6805
40.6308   42.5894   44.5541   46.5229   48.4940   50.4659   52.4370
54.4061   56.3719   58.3333   60.2890   62.2380   64.1791   66.1113
68.0333   69.9440   71.8423   73.7266   75.5956   77.4477   79.2807
81.0922   82.8785   84.6341   86.3486   88.0001   89.5403];

azi = [ -120.5952 -119.0686 -117.5699 -116.0966 -114.6466 -113.2174 -
111.8068 -110.4122 -109.0313 -107.6615 -106.3003 -104.9448 -103.5925 -
102.2402 -100.8848  -99.5231  -98.1515  -96.7661  -95.3626  -93.9364  -
92.4823  -90.9945  -89.4665  -87.8907  -86.2587  -84.5606  -82.7848  -
80.9179  -78.9439  -76.8441  -74.5956  -72.1714  -69.5387  -66.6576  -
63.4802  -59.9486  -55.9939  -51.5361  -46.4857  -40.7509  -34.2514  -
26.9440  -18.8578  -10.1297   -1.0171    8.1358   16.9749   25.2190
32.7042   39.3803   45.2780   50.4717   55.0525   59.1111   62.7298
65.9801   68.9221   71.6060   74.0732   76.3580   78.4886   80.4886
82.3776   84.1723   85.8865   87.5322   89.1196   90.6574   92.1535
93.6145   95.0463   96.4544   97.8434   99.2177  100.5812  101.9376
103.2903  104.6423  105.9968  107.3565  108.7241  110.1023  111.4936
112.9005  114.3253  115.7705  117.2383  118.7313  120.2515];
end



%% function solardatatovector1

function [alpha,gamma] = solardatatovector1(ele,azi,n,delta);
```

```
for i = 1:n;

    elea(i) = 90 - ele(i);

    if elea(i) <= 0;
        continue;
    end

    if abs(delta - azi(i)) >= 90;
        azi(i) = azi(i);
    end

    if elea(i) >= 90;
        elea(i) = 90;
    end


    alpha(i) = degtorad(elea(i));
    gamma(i) = degtorad(azi(i) - delta);
end

end

%% function panelincidentangle1

function [theta] = panelincidentangle1(alpha,gamma,n,sigma)

% thetai gives the angle of incidence of beam irradiance for each time
% in the solar data
for i = 1:n;

    costheta(i) = sin(alpha(i))*cos(sigma) +
cos(gamma(i))*cos(alpha(i))*sin(sigma);

    theta(i) = acos(costheta(i));

end
end


end
% end of functions within objval function
```